Multi-Decadal Convection Permitting Dynamical Downscaling of Current and Future Climates over South America

Changhai Liu

chliu@ucar.edu

National Center for Atmospheric Research https://orcid.org/0000-0003-4730-3116

Kyoko Ikeda

National Center for Atmospheric Research

Francina Dominguez

University of Illinois Urbana-Champaign

Andreas F. Prein

Institute for Atmospheric and Climate Science, ETH Zürich

Roy M. Rasmussen

National Center for Atmospheric Research

Zhe Zhang

National Center for Atmospheric Research

Lulin Xue

National Center for Atmospheric Research

Richard B. Neale

National Center for Atmospheric Research

Kwok Pan Chun

University of the West of England

Cenlin He

National Center for Atmospheric Research

Rosimar Rios-Berrios

National Center for Atmospheric Research

Michelle Simões Reboita

Universidade Federal de Itajubá - UNIFEI

Yongjie Huang

University of Oklahoma Norman Campus: The University of Oklahoma

Helber Barros Gomes

Federal University of Alagoas

Marta Llopart

Instituto Uruguayo de Meteorologia
Jimy Dudhia
National Center for Atmospheric Research
Yang Tian
National Center for Atmospheric Research
Lucia Scaff
University of Concepción
Adam C. Varble
Pacific Northwest National Laboratory
Luis Morales-Marin
Universidad Nacional de Colombia
Christoforus Bayu Risanto
Vatican Observatory, Vatican City State
Erin Dougherty
National Center for Atmospheric Research
Jorge Llamocca Huamani
National Service of Meteorology and Hydrology of Peru
Daniel Veloso-Aguila
Colorado State University
Kristen L. Rasmussen
Colorado State University
Aiguo Dai
University at Albany
Kelly M. Núñez Ocasio
Texas A&M University
Zachary L. Moon
Texas A&M University
Maria Laura Bettolli
Universidad de Buenos Aires-CONICET-IFAECI
Ye Mu
University of California Santa Barbara
José Augusto Paixão Veiga
Universidade do Estado do Amazonas
Everaldo Barreiros de Souza
Universidade Federal do Para
Erick Claros
University of Illinois Urbana-Champaign
Leila Constanza Hernandez Rodriguez
Lawrence Berkeley National Laboratory

Fei Chen
The Hong Kong University of Science and Technology
Zhe Feng
Pacific Northwest National Laboratory
Maria Leidinice da Silva
Abdus Salam International Centre for Theoretical Physics
Lluís Fita
Universidad de Buenos Aires
Rocio Balmaceda-Huarte
Universidad de Buenos Aires
Miguel Lagos-Zúñiga
Universidad Tecnica Federico Santa Maria
Decker Guzman Zabalaga
Universidad Mayor de San Andres
K. Santiago Hernández
Institute for Atmospheric and Climate Sciences, ETH Zrich
Elizabeth Silvestre Espinoza
Universidad Nacional Agraria La Molina
Franciano Scremin Puhales
Universidade Federal de Santa Maria
José A. Mantovani Jr.
National Institute for Space Research: Instituto Nacional de Pesquisas Espaciais
Marcelo Somos-Valenzuela
Baylor University
Juan Diego Giraldo-Osorio
Pontificia Universidad Javeriana
Octavia Crompton
USDA-ARS
Omar V. Müller
Universidad Nacional del Litoral
Timothy Schneider
National Center for Atmospheric Research
Andrew J. Newman
National Center for Atmospheric Research
Pablo A. Mendoza
Universidad de Chile
Julio T. Bacmeister
National Center for Atmospheric Research
Patrick Callaghan

National Center for Atmospheric Research
Wei Wang
National Center for Atmospheric Research
Danqiong Dai
University of Western Ontario
Cristian Martinez-Villalobos
Universidad Adolfo Ibanez
Diego Urdiales-Flores
University of Lausanne
Luis Gustavo Gonçalves de Gonçalves
Centro Euro-Mediterraneo sui Cambiamenti Climatici
Ingrid Petry
Hydraulic Research Institute / Federal University of Rio Grande do Sul (IPH/UFRGS)
Zhixiao Zhang
University of Oxford
Tomásio E. Januário
University of Sao Paulo
Angela Iza Wong
National Institute of Meteorology and Hydrology (INAMHI)
Santiago Nuñez Mejia
Universidad del Azuay
Víctor C. Mayta
University of Wisconsin-Madison
Flavio Justino
Universidade Federal de Vicosa
Germán Poveda
Universidad Nacional de Colombia
Peter J van Oevelen
George Mason University
Rosmeri Porfírio da Rocha
Universidade de Sao Paulo
Álvaro Ossandón
Universidad Tecnica Federico Santa Maria
Justin R Minder
University at Albany
Amanda Rehbein
Universidade de Sao Paulo
Rong Fu
University of California Los Angeles

Marcelo Zamuriano
Universidad Mayor de San Simon
Liping Di
George Mason University
Ethan D. Gutmann
National Center for Atmospheric Research

Research Article

Keywords: South America, dynamical downscaling, convection permitting, pseudo global warming, regional climate model simulation, WRF model

Posted Date: January 14th, 2026

DOI: https://doi.org/10.21203/rs.3.rs-8439819/v1

Multi-Decadal Convection Permitting Dynamical Downscaling of Current and Future Climates over South America

Changhai Liu[1 *], Kyoko Ikeda[1], Francina Dominguez[2], Andreas F. Prein[3], Roy M. Rasmussen[1], Zhe Zhang[1], Lulin Xue[1], Richard B. Neale[1], Kwok Pan Chun[4], Cenlin He[1], Rosimar Rios-Berrios[1], Michelle Simões Reboita[5], Yongjie Huang[6], Helber Barros Gomes[7], Marta Llopart[8,9], Jimy Dudhia[1], Yang Tian[1], Lucia Scaff[10], Adam C. Varble[11], Luis Morales-Marin[12], Christoforus Bayu Risanto[13], Erin Dougherty[1], Jorge Llamocca Huamani[14], Daniel Veloso-Aguila[15], Kristen L. Rasmussen[15], Aiguo Dai[16], Kelly M. Núñez Ocasio[17], Zachary L. Moon[17], Maria Laura Bettolli[18], Ye Mu[19], José Augusto Veiga[20], Everaldo Barreiros de Souza[21], Erick Claros[22], Leila Constanza Hernandez Rodriguez[23], Fei Chen[24], Zhe Feng[11], Maria Leidinice da Silva[25], Lluís Fita[26], Rocio Balmaceda-Huarte[27], Miguel Lagos-Zúñiga[28], Decker Guzman Zabalaga[29], K. Santiago Hernández[3], Elizabeth Silvestre Espinoza[30], Franciano Scremin Puhales[31], José A. Mantovani Jr.[32,33], Marcelo Somos-Valenzuela[34,35], Juan Diego Giraldo-Osorio (J. D. Giraldo-Osorio)[36], Octavia Crompton[37], Omar V. Müller[38], Timothy Schneider[1], Andrew J. Newman[1], Pablo A. Mendoza[39,40], Julio T. Bacmeister[1], Patrick Callaghan[1], Wei Wang[1], Danqiong Dai[41], Cristian Martinez-Villalobos[42,43], Diego Urdiales-Flores[44], Luis Gustavo Gonçalves de Gonçalves[45,46], Ingrid Petry[47], Zhixiao Zhang[48], Tomásio E. Januário[49], Angela Iza Wong[50], Santiago Nuñez Mejia[51], Víctor C. Mayta[52], Flavio Justino[53], Germán Poveda[54], Peter J van Oevelen[55], Rosmeri Porfírio da Rocha[56], Álvaro Ossandón[57], Justin R Minder[16], Amanda Rehbein[58], Rong Fu[59], Marcelo Zamuriano[60], Liping Di[61], Ethan D. Gutmann[1]

[1]NSF National Center for Atmospheric Research, Boulder, CO, United States

[2]University of Illinois at Urban Champaign, Urbana, United States

[3]Institute for Atmospheric and Climate Science, ETH Zürich, 8092 Zurich, Switzerland

[4]Univerisity of the West of England, Bristol, United Kingdom

[5]Universidade Federal de Itajubá - UNIFEI, Brazil

[6]Center for Analysis and Prediction of Storms (CAPS), University of Oklahoma, Norman, United States

[7]Institute of Atmospheric Sciences, Federal University of Alagoas, Maceió, Brazil

[8]Uruguay Instituto Uruguayo de Meteorología, Montevideo, Uruguay

[9]Departamento de Ciências Atmosféricas, Universidade de São Paulo, Brazil

[10]Department of Geophysics, University of Concepcion, Concepcion, Chile

[11]Pacific Northwest National Laboratory, Richland, United States

[12]Universidad Nacional de Colombia, Bogota, Colombia

[13]Vatican Observatory, Vatican City State

[14]National Service of Meteorology and Hydrology of Peru, Lima, Peru

[15]Department of Atmospheric Science, Colorado State University, Fort Collins, United States

[16]University at Albany, SUNY, Albany, United States

[17]Department of Atmospheric Sciences, Texas A&M University, College Station, United States

[18]Universidad de Buenos Aires-CONICET-IFAECI, Argentina

[19]Department of Geography, University of California, Santa Barbara, United States

[20]Universidade do Estado do Amazonas - UEA, Brazil

[21]Universidade Federal do Para - UFPA, Brazil

[22]Department of Civil and Environmental Engineering, University of Illinois Urbana-Champaign, Urbana, United States

[23]Lawrence Berkeley National Laboratory, Berkeley, USA

[24]The Hong Kong University of Science and Technology, Hong Kong

[25]The abdus Salam International Center for theoretical Physics, Italy

[26]Universidad de Buenos Aires, Centro de Investigaciones del Mar y la Atmósfera (CIMA), IFAECI UBA-CONICET-CNRS-IRD, Argentina

[27]Universidad de Buenos Aires-CONICET, Argentina

[28]Departamento de Obras Civiles, Universidad Técnica Federico Santa María, Valparaiso, Chile

[29]Laboratorio de Fisica de la Atmósfera, Instituto de Investigaciones Fisicas - Universidad Mayor de San Andrés, Bolivia

[30]Universidad Nacional Agraria la Molina, Peru

[31]Universidade Federal de Santa Maria - UFSM, Brazil

[32]National Institute for Space Research (INPE), Sao Jose dos Campos, Sao Paulo, Brazil

[33]Developmental Testbed Center (DTC), NSF National Center for Atmospheric Research, Boulder, Unites States

[34]Geosciences Department, Baylor University, United States

[35]Department of Forestry Science, Faculty of Agricultural and Environmental Sciences, University of La Frontera, Chile

[36]Pontificia Universidad Javeriana, Bogotá, Colombia

[37]USDA-ARS, Fort Collins, United States

[38]Universidad Nacional del Litoral-CONICET, Argentina

[39]Department of Civil Engineering, Universidad de Chile, Chile

[40]Advanced Mining Technology Center (AMTC), Universidad de Chile, Chile

[41]University of Western Ontario, London, Ontario, N6A3K7, Canada

[42]Faculty of Engineering and Science, Universidad Adolfo Ibañez, Santiago, Chile

[43]Data Observatory Foundation, ANID Technology Center, Santiago, Chile

[44]Institute of Earth Surface Dynamics, University of Lausanne, Lausanne, Switzerland

[45]Centro Euro-Mediterraneo sui Cambiamenti Climatici (CMCC), Bologna, Italy

[46]National Institute for Space Research (INPE), Sao Jose dos Campos, Sao Paulo, Brazil

[47]Hydraulic Research Institute / Federal University of Rio Grande do Sul (IPH/UFRGS), Porto Alegre, Brazil

[48]Department of Physics, University of Oxford, Oxford, Oxfordshire, UK

[49]Department of Atmospheric Science, University of Sao Paulo - IAG/USP, SP, Brazil

[50]National Institute of Meteorology and Hydrology (INAMHI). Quito, Ecuador

[51]Universidad del Azuay - TRACES, Universidad de Cuenca - iDRHICA. Cuenca, Ecuador

[52]Department of Atmospheric and Oceanic Sciences, University of Wisconsin, Madison, United States

[53]Universidade Federal de Vicosa, MG, Brazil

[54]Deparment of Geosciences and Environment, Universidad Nacional de Colombia, Medellín, Colombia

[55]Department of Atmospheric, Ocean & Earth Sciences, George Mason University / Internationan GEWEX Project Office, United States

[56]Departamento de Ciências Atmosféricas, Universidade de São Paulo, São Paulo, Brazil

[57]Departamento de Obras Civiles, Universidad Técnica Federico Santa María, Valparaiso, Chile

[58]Departamento de Ciências Atmosféricas, Universidade de São Paulo, São Paulo, Brazil

[59]Department of Atmospheric and Oceanic Sciences, University of California, Los Angeles, United States

[60]Departamento de Física, Universidad Mayor de San Simón, Cochabamba, Bolivia

[61]Center for Spatial Information Science and Systems, George Mason University, Fairfax, United States

Submitted to *Climate Dynamics*

December 22, 2025

*Corresponding author: Dr. Changhai Liu, NSF National Center for Atmospheric Research, P. O. Box 3000, Boulder, CO 80307-3000, USA.
E-mail: chliu@ucar.edu ORCID: 0000-0003-4730-3116

Abstract

This paper reports on two sets of 22-year convection-permitting regional climate simulations conducted with the Weather Research and Forecasting model over the entirety of South America at 4-km grid spacing. The first simulation downscales the fifth-generation European Centre for Medium-Range Weather Forecasts atmospheric reanalysis (ERA5) to reproduce the present-day climate conditions over the period 2000-2021. The second simulation projects late-century climate change using the Pseudo-Global Warming (PGW) approach, in which the meteorological reanalysis fields are perturbed using monthly climate change signals from the Community Earth System Model Large Ensemble (LENS2), corresponding to ~3°C of global warming under the CMIP6 SSP3-7.0 scenario during 2060-2080. Results show that the historical simulation successfully captures multiscale climatological characteristics of precipitation and near-surface air temperature, including their interannual cycle down to diurnal variabilities, as validated against multiple satellite and reanalysis datasets, and demonstrates clear added value compared to the original ERA5 data, particularly at daily to sub-daily temporal and mesoscale to local spatial scales. The PGW simulation projects significant continental-scale warming, especially over the Andes, broadly consistent with LENS2 projections. Precipitation changes are spatially and seasonally complex, with most regions undergoing either increases or slight decreases, while the Amazon Basin exhibits predominant warm season drying. Additionally, extreme precipitation intensifies across the continent, and snowfall and snowpack decline over the Andes. These simulations provide a first-of-its-kind long-term high-resolution dataset for the climate science and policymaking communities, enabling detailed studies of atmospheric, land-surface, and hydrological processes in South America and their changes under a warming climate.

Keywords: South America, dynamical downscaling, convection permitting, pseudo global warming, regional climate model simulation, WRF model

1 Introduction

High-resolution climate data is essential for accurately characterizing regional climate variability and extreme events such as heatwaves, floods, and droughts (Giorgi and Gutowski 2015; Ban et al. 2014; Kendon et al. 2017). Its spatial granularity enables reliable local impact assessments and better-informed adaptation and mitigation planning (IPCC 2021). Sectors like agriculture, water management, hydropower generation, human health, urban planning, and disaster risk reduction increasingly depend on fine-scale projections for localized decision-making (Hewitson et al. 2014; Lenderink et al. 2014). While global climate models (GCMs) are indispensable for understanding long-term large-scale climate dynamics, their coarse spatial resolution limits their ability to represent mesoscale to small-scale atmospheric and land-surface processes that influence local climates and extremes (Prein et al. 2020; Feng et al. 2023). To bridge this scale gap, downscaling has become pivotal for translating coarse-resolution GCM outputs into fine-scale climate information that facilitates regional climate and impact studies (Benestad et al. 2008; Giorgi et al. 2009; Maraun et al. 2010).

Among commonly used downscaling techniques, dynamical downscaling, or regional climate simulation, generates high-resolution climate data by driving a regional climate model (RCM) with coarse-resolution GCM output or reanalysis boundary conditions (Giorgi and Mearns 1991; Laprise 2008). Since its introduction in the late 1980s, the approach has progressed from initial coarse-resolution to today's km-scale resolution simulations, supported by advances in model physics (Xue et al. 2014; Giorgi 2019; Prein et al. 2015; Schär et al. 2020; Lucas-Picher et al. 2021). Early RCMs in the 1990s operated at ~50–100 km resolution to capture regional climate variability unresolved by GCMs (Giorgi and Mearns 1991; Giorgi 2006). With growing computational power, resolutions improved to 10–25 km, enabling better simulation of mesoscale processes, terrain-driven precipitation, and land–atmosphere interactions (Rummukainen 2010; Gutowski et al. 2010). Over the past decade or so, convection-permitting RCMs (CPRCMs) at ~1–5 km resolution have marked a major advance (Liu et al. 2017; Senior et al. 2021; Halladay et al. 2023; Rasmussen et al. 2023). By explicitly resolving deep convection, they eliminate the need for cumulus parameterization (Prein et al. 2015; Kendon et al. 2017; Liu et al. 2017; Schär et al. 2020) and provide more realistic simulations of convective storms, precipitation extremes, and short-timescale variability through enhanced representation of complex terrain, land-surface heterogeneity, coastlines, and many other mesoscale to small-scale processes (Rasmussen et al. 2011, 2014, 2023; Kendon et al. 2012, 2014; Ban et al. 2014, 2021; Fosser et al. 2015; Prein et al. 2017, 2024; Stratton et al. 2018; Coppola et al. 2020; Yun et al. 2020; Giorgi et al. 2023; da Rocha et al. 2024).

Beyond improvements in spatial resolution, dynamical downscaling has advanced through more sophisticated methods for prescribing boundary forcing. Traditionally, RCMs were directly driven by GCM or reanalysis data via lateral boundary conditions using time-slice or transient approaches (Jones et al. 1995; Christensen et al. 2007). Subsequent developments introduced bias-correction techniques that adjust GCM boundary conditions toward observed climatology, thereby reducing systematic errors transferred to regional simulations (Maraun et al. 2010; Ehret et al. 2012; Done et al. 2015; Dai et al. 2020). More recently, the pseudo-global warming (PGW) framework has gained prominence, modifying historical conditions with projected mean GCM changes to preserve synoptic variability while isolating future thermodynamic forcing (Schär et al. 1996; Kawase et al. 2009; Rasmussen et al. 2011; Liu et al. 2017; Wang et al. 2025). A further refinement incorporates transient GCM weather perturbations in addition to mean changes, addressing a key limitation of the original PGW approach (Dai et al. 2020).

Together, advances in model resolution and forcing strategies have established dynamical downscaling as a central tool for regional climate research, enabling more realistic projections to support impact assessments and adaptation planning (e.g., Mendoza et al. 2015a, 2016). However, applications of convection-permitting downscaling remain limited in South America, where complex topography, strong land–atmosphere coupling, and diverse climate regimes pose persistent modeling challenges.

The South American climate is characterized by substantial spatial heterogeneity arising from its wide latitudinal extent, complex topography and land-surface atmospheric feedbacks, and interactions with major atmospheric and oceanic circulation systems (Garreaud et al. 2009; Reboita et al. 2021). The Amazon rainforest, the world's largest tropical forest, exerts a dominant control on regional and remote hydrological processes through intense evapotranspiration and efficient precipitation recycling (Salati and Vose 1984; Zemp et al. 2014; Dominguez et al. 2022; Qin et al. 2025). Recycled moisture sustains rainfall within the basin and is transported downstream, influencing precipitation over southeastern South America and even into the subtropics (Moraes-Arraut et al. 2012; Poveda et al. 2014; Zemp et al. 2014; Zemp et al. 2017; Boers et al. 2017; Drumond et al. 2014; Yang and Dominguez 2019; Ruiz-Vásquez et al. 2024; Claros et al. 2025). The Andes impose strong dynamical controls by acting as a major meridional barrier, producing sharp east–west precipitation gradients and shaping regional and hemispheric circulation and extreme rainfall intensities over northwestern South America and Patagonia (Garreaud et al. 2003, 2009; Herdies et al. 2002; Viale et al. 2019; Espinoza et al. 2020; Poveda et al. 2020; Rojas and Minder 2024; Claros & Kuroiwa 2025). The range also modulates the South American Low-Level Jet (SALLJ; Salio et al. 2002; Marengo et al. 2004; Wang and Fu 2004), which supplies moisture to subtropical South America (Berbery and Barros 2002) and supports some of the deepest (Zipser et al. 2006), largest (Velasco and Fritsch 1987), and longest-lived (Durkee and Mote 2009) mesoscale convective systems (MCSs) globally with extreme lightning (Cecil et al. 2015) and hail (Cecil and Blankenship 2012; Kumjian et al. 2020).

The South American climate is also shaped by large-scale ocean–atmosphere interactions, such as the Intertropical Convergence Zone (ITCZ; Poveda et al. 2006) at seasonal timescales, and the El Niño–Southern Oscillation (ENSO), which drives substantial interannual rainfall variability across northern and southeastern regions of the continent (Ropelewski and Halpert 1987; Grimm et al. 2000; Cai et al. 2020; Reboita et al. 2021). The continent forms a core component of the South American Monsoon System (SAMS), the dominant seasonal circulation over tropical and subtropical South America. SAMS interacts with global circulation features, including the Hadley and Walker cells and ENSO (Vera et al. 2006; Marengo et al. 2012; Campos and Rondanelli 2023), and produces a pronounced austral-summer wet season. It also gives rise to the South America Convergence Zone (SACZ; Kodama 1992; Carvalho et al. 2002), a northwest–southeast-oriented band of enhanced precipitation.

In addition, land–atmosphere interactions play an important role in influencing the South American climate. For instance, enhanced evapotranspiration prior to the wet season supplies moisture that increases precipitation (Fu et al. 1995; Wright et al. 2017). The resulting latent heating drives moisture transport into the Amazon and strengthens the upper-tropospheric anticyclonic circulation over the SAMS region (Li and Fu 2004), affecting wet-season onset over the southern Amazon (Fu and Li 2004). Betts and Viterbo (2005) further demonstrated that these interactions involve coupling among soil moisture, sub-cloud relative humidity, boundary-layer clouds, and deep convection.

The intricate interactions among the aforementioned atmospheric, land and oceanic systems give rise to substantial spatial and temporal climate variability over South America, complicating climate prediction and impact assessment. While GCMs, including those participating in the Coupled Model Intercomparison Projects (CMIP3, CMIP5, and CMIP6), have shown progress in representation of large-scale processes (e.g., Leung et al. 2022), significant biases persist (de Medeiros et al. 2022). Many of these limitations stem from coarse spatial resolution and simplified physical parameterizations (Solman et al. 2008; Marengo et al. 2012). For instance, GCMs commonly underestimate precipitation in the Amazon and subtropical South America and suffer a persistent double-ITCZ bias, misrepresenting key circulation systems such as the SACZ and SALLJ that affect hydrological cycles and monsoon timing (Li et al. 2006; Yin et al. 2013; Zhang et al. 2015; Sakaguchi et al. 2018; Adam et al. 2020). Additionally, the Andes, a dominant control on regional circulation and precipitation gradients, are poorly resolved, leading to substantial errors across western South America (Reichler and Kim 2008; Duffy et al. 2003). While CMIP6 models exhibit improvements in regional climate variability and extremes relative to earlier generations, large inter-model spread and persistent biases remain, particularly in depicting convection, precipitation, and land–atmosphere coupling (Haarsma et al. 2016; IPCC 2021; Gateño et al. 2024; Vásquez et al. 2024 2025). These limitations highlight the need for high-resolution regional downscaling to enhance the reliability of climate projections and impact assessments in South America (Arias et al. 2025).

Although regional climate downscaling has progressed relatively slowly in South America largely due to limited computational resources, it has nonetheless become essential for advancing understanding of the continent's complex climate system and for generating climate projections at decision-relevant scales (Dominguez et al. 2024; Martinez et al. 2024). Foundational efforts, including the CLARIS (Solman et al. 2013) and CREAS (Marengo et al. 2012) projects and later CORDEX South America initiatives (Giorgi et al., 2022; Bettolli et al. 2021), have supported assessments of future changes in the SAMS, Amazon rainfall, extratropical cyclones, and hydrological extremes, informing sectors such as water management, agriculture, and disaster risk reduction (Chou et al. 2014; Crespo et al. 2023; Lagos-Zúñiga et al. 2024). More recently, CPRCMs with ~4-km grid spacing have been increasingly applied across the region, yielding substantial improvements in representing climate processes over a range of spatial and temporal scales (Portele et al. 2021; Feijoó and Solman 2022; Halladay et al. 2023; Huang et al. 2023, 2024a, 2024b; Lagos-Zúñiga 2024; Liu et al. 2025; Hernández et al. 2025). To further advance hydroclimate research based on CPRCMs, the South America Affinity Group (SAAG) now coordinates a network of more than 100 researchers worldwide (Dominguez et al. 2024).

This study presents and analyzes the SAAG dynamical downscaling efforts over South America across a 22-year historical period, which include a PGW experiment designed to project late-century changes under the CMIP6 SSP3-7.0 scenario. It builds upon and extends the findings from year-long experiments reported in Liu et al. (2025). The primary objectives are: (1) to develop a long-term high-resolution community dataset to support research on hydroclimate processes, climate change impacts, and policymaking, and (2) to investigate the performance of the employed CPRCM in reproducing the multiscale spatiotemporal characteristics of the present-day climate and its potential responses to future global warming. Section 2 describes the model configuration, methodology, and evaluation datasets. The evaluation of the downscaled present-day climate and a preliminary analysis of projected future changes are presented in Sections 3 and 4, respectively. Finally, a discussion and conclusions are provided in Section 5.

2 Numerical model, simulation design, and evaluation data

Two sets of multi-decadal regional climate downscaling simulations were conducted using the widely-used state-of-the-art Weather Research and Forecasting (WRF) model with convection-permitting spatial resolution: a historical climate simulation for the period 2000-2021 and a perturbed climate simulation covering the same period under the CMIP6 SSP3-7.0 scenario as detailed below. The historical simulation serves as a baseline, aimed at reproducing recent climatological characteristics, thereby reinforcing confidence in the model configuration for climate projections. The climate sensitivity simulation offers a physically consistent representation of one scenario of late-century climate conditions under enhanced greenhouse gases (GHGs) forcing.

2.1 Model configuration

The model configuration closely followed the framework established by Liu et al. (2025) through year-long experiments, and is summarized below for completeness. The WRF model version 4.1.5 (Skamarock et al. 2019) was utilized, with a single computational domain consisting of 1472 x 2028 grid points at a 4-km horizontal grid spacing, which fully covers the entire South American continent and part of adjacent oceans (Fig. 1a). The configuration includes 61 stretched vertical levels extending from surface up to 10 hPa, with a 10-km deep sponge layer to mitigate the impact of vertically propagating gravity waves over the towering Andes Mountains. The primary physics parameterizations include: the Thompson microphysics scheme (Thompson et al. 2008), the Yonsei University planetary boundary layer scheme (Hong et al. 2006) coupled with the Revised Monin-Obukhov surface layer scheme (Jimenez et al. 2012), the Rapid Radiative Transfer Model for GCMs (RRTMG) longwave and shortwave radiation (Iacono et al. 2008), and the Noah land surface model with multiple parameterization options (Noah-MP; Niu et al. 2011; He et al. 2023), coupled with the MMF groundwater scheme (Miguez-Macho et al. 2007). This model setup has been tested across different ENSO phases in Liu et al. (2025), showcasing high skill in reproducing the observed multi-scale spatiotemporal characteristics of precipitation and temperature over South America. The main difference between the WRF model configurations used in North America (Liu et al. 2017; Rasmussen et al. 2023) and the present study is the omission of spectral nudging, which was found to offer minimal benefits for simulating the South American climate (Liu et al. 2025). Additionally, the current configuration also excludes an available scale-aware deep precipitating convection parameterization, as these schemes have been shown to provide limited added value at convection-permitting resolutions (Liu et al. 2021, 2025).

2.2 Historical climate simulation

The historical climate simulation spans approximately 22 years, from 31 December 1999 to 31 December 2021, excluding the first day spinup from the analysis. The initial and lateral boundary conditions are provided by the hourly ERA5 reanalysis product at a horizontal grid spacing of 0.25° (Hersbach et al. 2020). For the lower boundary condition, the sea surface temperature (SST) is taken from ERA5 over open waters and large inland water bodies. For small water bodies, the skin temperatures are obtained from the diurnal averages of 2-m surface air temperature, as ERA5 cannot resolve these smaller features.

2.3 Future climate simulation

The future climate simulation is designed to downscale the late-century South American climate projected by the Coupled Model Intercomparison Project Phase 6 (CMIP6) under the Shared Socioeconomic Pathway (SSP) 3-7.0 emission scenario using the PGW method. This approach, first pioneered by Schär et al. (1996) and further developed and widely adopted in the climate downscaling community (e.g., Sato et al. 2007; Hara et al. 2008; Kawase et al. 2009; Rasmussen et al. 2011; Kay et al. 2015; Liu et al. 2017; Rodgers et al. 2021; Heim et al. 2023; Wang et al. 2025), applies climate perturbations derived from GCM projections to adjust the reanalysis-based initial and boundary forcing used in baseline historical regional climate simulations, allowing for the simulation of global climate change effects on a regional scale without requiring full future boundary conditions. As such, it is expected that the lateral boundary forcing in the PGW simulation reflects the mean late–21st-century climatological conditions projected by GCMs, while preserving daily weather system variability similar to historical conditions.

As shown in Eqs. (1)-(2), the climate perturbations for this study were derived from the Community Earth System Model version 2 (CESM2) Large Ensemble (LENS2) simulations, which consist of 100 members at a 1-degree horizontal resolution covering the period 1850-2100 under CMIP6 historical and SSP370 future radiative forcing scenarios (Rodgers et al. 2021):

$$WRF_{input} = ERA5 + \Delta LENS2_{SSP370} \quad (1)$$

$$\Delta LENS2_{SSP370} = LENS2_{2060\text{-}2080} - LENS2_{2000\text{-}2020} \quad (2)$$

where $\Delta LENS2_{SSP370}$ is the ensemble-mean monthly change signal under the CMIP6-SSP370 scenario, representing the difference between the historical monthly climate for the 21-year period 2000-2020 ($LENS2_{200\text{-}2020}$) and the late-century monthly climate for the 21-year period 2060-2080 ($LENS2_{2060\text{-}2080}$). The period 2060-2080 was selected based on the projected changes in global mean temperature to be about ~3^{o}C above pre-industrial values (Rodgers et al. 2021). While it does not represent the full range of uncertainty, this provides one plausible high-impact pathway (Kawase et al. 2021; Giorgi 2019).

The monthly perturbed physical fields include geopotential height, horizontal wind, air temperature, relative humidity, sea level pressure, SST, soil temperature, and sea ice fraction. These fields are assumed to be valid at the middle of each month and are linearly interpolated to the hourly ERA5 data. It is important to note that introducing a climate perturbation can roughly preserve the hydrostatic, geostrophic, and thermal wind balances in large-scale dynamics because the difference between two balanced mean climatological fields approximately maintains the linear relationships among the temperature, geopotential height, and horizontal wind perturbation fields (Rasmussen et al. 2011). To maintain consistency with the imposed climate warming signal, the concentrations of all GHG species used in the radiative transfer model are adjusted to levels representative of 2070s, following the CMIP6 SSP3-7.0 scenario. These concentrations approximate the multi-year average over the 2060–2080 period.

The large-member ensemble mean difference effectively reduces the substantial internal variability present in individual GCM realizations, making it a more realistic representation of anthropogenically induced climate signals. The monthly perturbation fields in Fig. 2, $\Delta LENS2_{SSP370}$, at 850 and 250 hPa, as well as the SST perturbations, offer a visual representation of the imposed climate change signals in the PGW simulation. Overall, the lower-tropospheric circulation perturbations (Figs. 2a-d) are quite weak across all months, especially over land, with wind speed changes generally staying below 2 m s^{-1} almost everywhere. A consistent pattern of easterly perturbations is observed year-round in Southern South America (SSA) and its surrounding waters. Another notable feature is the wintertime systematic anticyclonic circulation in the tropics and subtropics, accompanied by northerly wind perturbations east of the Andes (Fig. 2c), which could suggest an intensification or change of altitude of the SALLJ in the future climate. In general, the upper-level wind perturbations (Figs. 2e-h) are more pronounced, with relatively strong midlatitude westerly perturbations observed during austral summer, fall, and spring seasons, attaining peak wind speeds over 4 m s^{-1}. In summer (Fig. 2e), the wind perturbations become more prominent in the tropics and subtropics, converging toward the Amazon Basin.

The low-level relative humidity (RH) over land (Figs. 2a-d) exhibits dominant negative changes in lower latitudes, including the Amazon, and prevailing positive changes in higher latitudes, such as the La Plata Basin and SSA. In contrast, the low-level RH over most oceans undergoes larger reductions compared to that over the continent. Comparatively large absolute changes occur in the upper troposphere (Figs. 2e-h). During summer and fall, there are RH decreases in the tropical and subtropical regions, with increments observed roughly south of 25°S. On the other hand, winter and spring are characterized by widespread RH decreases across almost the entire domain. Notably, a reduction in RH does not necessarily indicate a decrease in specific humidity, due to the warming temperature that shows a robust signal throughout the troposphere. In the lower troposphere (Figs. 2a-d), a relatively uniform spatial warming pattern is witnessed during summer and spring, mostly ranging from 2-3°C. During winter and fall, a strong warming signal of 3-3.5°C is seen in the subtropics, tapering to 1.5-2°C south of 30°S. In the upper troposphere (Figs. 2e-h), strong warming exceeding 4°C occurs in the tropics, decreasing to about 1.5°C in high latitudes. The seasonal pattern reveals the largest warming in summer (Fig. 2e) and the weakest warming in spring (Fig. 2h). It is worth pointing out that the altitude-dependent warming magnitude is suggestive of an enhancement of static stability, which would decrease deep convective mass flux.

The imposed SST perturbation is the primary component of the lower boundary forcing, given the minimal extent of sea ice within the model domain. As shown in Figs. 2i-l, ocean warming varies spatially between 1 - 3.5°C with slightly greater signals in summer and fall. The highest warming occurs in the upwelling coastal waters of Peru and northern Chile, while the lowest warming is observed over the Southern Ocean and Atlantic waters north of South America.

2.4 Model evaluation data

Eight datasets were used for evaluating the historical simulation or for comparisons against the PGW simulation. These datasets include six satellite- or gauge-based precipitation products, one reanalysis-based precipitation and surface air temperature product, and LENS2-projected precipitation and surface air temperature data for the late century. The multiple observation-based gridded precipitation products are employed to assess uncertainties in precipitation observations. Each of these datasets is described as follows.

1) IMERG precipitation. The Integrated Multi-Satellite Retrievals for Global precipitation measurement (IMERG; Huffman et al. 2019) dataset is created by fusing passive microwave precipitation retrievals from multiple satellites with infrared observations to fill the temporal

gaps, thereby providing continuous global precipitation data for more than two decades, starting in June 2000. In this study, we used IMERG Version 06, the most recent version available at the time of data processing. This version is gauge-adjusted and provided on a 0.1° spatial grid with a half-hour temporal grid. This relatively high-resolution precipitation product is employed to evaluate various precipitation characteristics across hourly to annual time scales in the historical climate simulation.

2) CPC precipitation. The National Weather Service's Climate Prediction Center (CPC) produces a gauge-based analysis of daily precipitation on a 0.5° latitude/longitude grid over global land areas from 1979 to the present. This precipitation product combines all available sources, including rain gauge measurements, satellite observations, and numerical weather prediction models (Chen et al. 2008). In this study, the daily precipitation data is mapped to the IMERG spatial grid using bilinear interpolation.

3) GPCP precipitation. The Global Precipitation Climatology Project (GPCP) provides global monthly precipitation estimates by integrating various satellite datasets over land and ocean, along with a gauge analysis over land, on a 2.5-degree global grid from 1979 to the present (Adler et al. 2003). The coarse-resolution monthly precipitation data is bilinearly interpolated to the IMERG spatial grid.

4) CHIRPS precipitation V2.0. The Climate Hazards Group InfraRed Precipitation with Station data (CHIRPS) provides relatively high-resolution, long-term land-only precipitation estimates, covering a spatial range from 50°S to 50°N and a temporal range from 1981 to the near present, with various temporal and spatial resolutions (Funk et al. 2015). It incorporates an in-house climatology, 0.05° resolution satellite imagery, and in-situ station data to create gridded

precipitation time series for trend analysis and seasonal drought monitoring. This study uses the monthly, 0.05° resolution data, which is conservatively remapped to the IMERG spatial grid using the ESMF_regrid function of the NCL software package.

5) CMORPH precipitation. The Climate Prediction Center (CPC) Morphing Technique (CMORPH) dataset is estimated from multiple passive microwave sensors and is bias corrected against CPC daily gauge analysis over land and is adjusted against GPCP merged analysis of pentad precipitation over ocean (Xie et al. 2017). This dataset has a spatial grid of 8 km (~0.08°) and a temporal grid of 30 minutes, covering 60°S to 60°N and January 1998 to present. The data is interpolated to the IMERG spatial grid using the nearest neighbor method.

6) MSWEP precipitation. The Multi-Source Weighted-Ensemble Precipitation (MSWEP) provides near real-time precipitation estimates with a 3-hourly, 0.1° horizontal grid and full global coverage, spanning a long record that begins in 1979 (Beck et al. 2019). One unique feature of MSWEP is its integration of daily gauge, satellite, and reanalysis data, while also accounting for gauge reporting times, to obtain the highest quality precipitation estimates. The sub-daily precipitation data is remapped to the IMERG spatial grid using the nearest neighbor method.

7) ERA5 precipitation and temperature. ERA5 is the latest generation of global reanalysis, offering a 0.25° horizontal resolution at hourly time steps (Hersbach et al. 2020). In addition to serving as forcing for the simulations, ERA5 precipitation forecasts are compared with the historical simulation to assess the potential added value of the downscaling, while ERA5 2-meter temperature analysis is used to evaluate the historical simulation. ERA5 precipitation is linearly interpolated to the IMERG spatial grid, and the model temperature is remapped to the ERA5 spatial grid using the ESMF_regrid function of the NCL software package.

8) LENS2 precipitation and temperature. In addition to providing forcing for the PGW simulation, LENS2 projected mean precipitation and temperature changes are used to compare the projected changes in the higher resolution downscaled PGW simulation.

3 Validation of historical simulation

This section presents a comprehensive evaluation of the historical climate simulation (hereafter referred to as HIST), focusing on two critical climate variables: precipitation and surface air temperature. As IMERG data are available since June 2000, the analysis of temporal precipitation averages focuses on the 21 water years from June 2000 to May 2021, excluding the first 5 months and last 7 months of the historical simulation. Note that the water year definition varies across the continent. For this study, the water year starts in June of one year and ends in May of the following year. Furthermore, the austral winter, spring, summer, and fall seasons in the Southern Hemisphere are hereafter defined as June-July-August (JJA), September-October-November (SON), December-January-February (DJF), and March-April-May (MAM), respectively.

3.1 Precipitation

We assess the model's ability to reproduce observed precipitation patterns, variability, and intensity across a range of spatial and temporal scales, while using the historical simulation as the baseline for future projections. Figure 3 shows a comparison of annual precipitation, averaged over the 21 water years, between IMERG, HIST, and ERA5. According to IMERG (Fig. 3a), there is considerable variability in the annual precipitation averages across the continent, with the largest amounts in the tropical regions, which generally decreases towards higher latitudes but is strongly influenced by topography and proximity to oceans. The overall patterns align with those seen in other precipitation datasets (Fig. S1), particularly with the other relatively high-resolution CHIRPS, CMORPH, and MSWEP datasets. The WRF model reproduces the observed distributions of annual precipitation reasonably well (Fig. 3b), capturing the meridional gradient, the heavy tropical rainfall exceeding 5,000 mm along the Colombian coast and northwestern Amazon largely due to the influence of the Chocó low-level jet (Poveda and Mesa 1999, 2000; Yepes et al. 2019; Poveda 2023), intense orographic precipitation in central and southern Chile, and the low precipitation (< 100 mm) extending over the Atacama Desert in northern Chile and the adjacent Peruvian coast. However, some discrepancies are evident, such as overestimation of precipitation in the Andes and central Amazon, and underestimation over the tropical Atlantic coastal interior and the La Plata Basin (Fig. 3d). Quantitatively, HIST vs IMERG yield a spatial pattern correlation coefficient of 0.81 and a wet bias of ~6%; large mountain-region differences dominate the mean absolute error (MAE) and root mean square error (RMSE), with values of 341 and 685 mm, respectively.

It is important to note, however, that satellite estimates have substantial uncertainties, particularly in regions influenced by topographic effects and deep convection (Tan et al. 2019; Huffman et al. 2020; Vallejo-Bernal et al. 2020). IMERG retrievals over snow-covered areas are also problematic, and the scarcity of in-situ observations for calibration further contributes to the uncertainty. Additionally, the alternating negative-positive bias pattern over the northern tropical Andean Mountains likely arises from the limitations of IMERG’s resolution, which struggles to properly resolve the narrow ridges and valleys (e.g., Rojas et al. 2021), rather than being a flaw of the model. Likewise, the precipitation underestimation in IMERG documented by Rojas and Minder (2024) could contribute to the wet bias in the southern Andes. The IMERG data is compared with five additional precipitation products to assess observational uncertainties. As shown in Fig. 3d, the stippled areas indicate where the absolute difference between IMERG and HIST is smaller than the absolute difference between IMERG and at least one of the five other estimates. The significant wet biases over major mountain ranges (e.g., the Andes, Guiana Highlands, and the Serra do Mar mountain in southeastern Brazil) and dry biases near the tropical Atlantic coasts and in the southern La Plata Basin fall outside the range of observational uncertainties, though it is possible that all the gridded observational datasets struggle to quantify precipitation in mountainous terrain. A similar systematic dry bias over the La Plata Basin has been reported in coarse-resolution WRF modeling (Müller et al. 2014; Bracalenti et al. 2024; Liu et al. 2025), suggesting that enhanced resolution alone is not sufficient to reproduce the observed precipitation.

Like HIST, ERA5 effectively captures the large-scale climatological patterns as well (Fig. 3c), though it produces a more widespread strong wet bias over the Andes in comparison with HIST, along with a dry bias over most other regions of the continent (Fig. 3e). ERA5 has smaller dry biases than HIST over much of the La Plata Basin and the tropical Atlantic coastal areas. Overall, HIST exhibits a slight performance advantage over ERA5, as demonstrated by the evaluation metrics conducted here (i.e., pattern correlation, mean bias, absolute bias, and RMSE), emphasizing the benefits of convection-permitting downscaling.

The simulation closely matches the observations in the spatial distribution of seasonal precipitation (Fig. 4). Due to the influence of ITCZ activity, winter precipitation is primarily concentrated just north of the equatorial region (Figs. 4a and e), with the heaviest precipitation forming a southwest-northeast oriented band extending through Venezuela and Colombia. On the other hand, with the onset of the monsoon, seasonal precipitation in spring (Figs. 4b and f) expands southeastward, forming an extensive northwest-southeast oriented rainband. Heavy rainfall begins in the northwest, stretches into the Amazon Basin, and tapers off toward the southeast coast, coinciding with the SACZ. With the progression of the summer monsoon and the seasonal migration of the ITCZ, rainfall in northern South America weakens significantly. Meanwhile, the major rainband intensifies and shifts into the Southern Hemisphere, extending southeastward from the equator to the coastal region along the SACZ (Figs. 4c and g). In this season, the La Plata Basin receives moderate precipitation, which gradually decreases from the subtropical to the temperate regions. As the monsoon weakens and retreats equatorward in the fall, seasonal precipitation decreases in the subtropics considerably and becomes concentrated in the Amazonian region (Figs. 4d and h).

Even though the simulation accurately replicates the large-scale seasonal pattern and most of deviations from IMERG are within the observational uncertainties (Figs. 4i-l), several model errors remain apparent. Similar to the annual precipitation (Fig. 3d), significant wet biases are present over large topographic features, including the high Andes Mountains, their slopes and foothills, and the Guiana Highlands, contributing to the domain-wide positive precipitation difference from IMERG in spring, summer, and fall. Also, significant dry biases are found in tropical Atlantic coastal areas across all seasons, to a lesser extent, in southern Brazil during winter and spring and central Argentina-Uruguay strongly in summer. The simulation seems to perform best in the relatively dry winter season, exhibiting the highest pattern correlation (0.9) and the lowest bias (-1.9%) and RMSE (166 mm).

In addition to annual and seasonal patterns, monthly precipitation climatologies are reasonably well reproduced (see comparison between HIST and IMERG in Fig. S2). In particular, the simulation aligns well with the observations in terms of heavy precipitation locations and spatial extents, as well as the southward progression from late winter to early summer and the subsequent northward withdrawal from early fall to early winter. These features result in spatial pattern correlations greater than 0.8 and areal mean biases below 10% for most months. The simulation performs somewhat better during April–September than during October–March, as indicated by higher correlations and smaller percentage biases.

An analysis of the probability density function (PDF) of daily and hourly precipitation is presented in Fig. 5, evaluating how well the simulation reproduces observed frequency distributions from light through heavy events and illustrating the added value over the ERA5 forcing. The results demonstrate a high degree of alignment between HIST and IMERG for the domain-wide daily precipitation spectrum (Fig. 5a), with only a minimal underprediction of weak precipitation events less than ≈20 mm day^{-1} and an overproduction of stronger precipitation events at higher intensities. A fairly good comparison is also seen for the continent-wide hourly precipitation (Fig. 5g), exhibiting similar discrepancy patterns but with larger magnitudes, i.e., underpredicted precipitation events weaker than ≈7 mm h^{-1} and overpredicted those above this threshold. These multi-year statistics and model-observation differences are consistent with year-long experiments across different ENSO phases in Liu et al. (2025). Spectral discrepancies between model and IMERG point to a systematic underestimation of event frequency and an overestimation of mean intensity at daily and hourly timescales, averaged across the entire domain, though past studies have noted that IMERG tends to overestimate the frequency of light precipitation and underestimate heavy precipitation over continental regions (e.g., Cui et al. 2020; Ayat et al. 2021; Zhang et al. 2021; Feng et al. 2025), partly due to its effective resolution (Guilloteau and Foufoula-Georgiou, 2020). Thus, it is reasonable to assume that the HIST predictions may be more accurate than suggested by comparisons with gridded, satellite-based precipitation products.

ERA5 performs poorly in representing the observed precipitation spectra at both daily and hourly scales, with the hourly scale showing a greater discrepancy (Fig. 5). Although it reasonably reproduces the annual precipitation total (Fig. 3), ERA5 substantially simulates more daily events less than ≈24 mm day^{-1} and hourly events below ≈4 mm h^{-1}, while producing less intense daily and hourly events and seemingly missing extreme events altogether. The deficient precipitation intensity spectra in ERA5 are linked to the well-known "drizzle problem", referring to an overabundance of light precipitation events and a scarcity of heavy precipitation storms, a common issue observed in coarse-resolution models with parameterized convection (e.g., Dai 2006). The inferior performance of ERA5 in this regard provides further evidence of the added value of the downscaling simulation, compared to IMERG estimates.

Given the significant variability in precipitation climatology across the continent, a sub-regional analysis is essential to assess the model's performance across different climate zones and to account for potential geographical dependencies. Figs. 5b-f compare the probability distributions of daily precipitation across five of the seven IPCC climate reference regions (Fig. 1b): Northern South America (NSA), South American Monsoon (SAM), Southeast South America (SES), Southwest South America (SWS) and Southern South America (SSA). The two regions not shown, Northwest South America (NWS) and Northeast South America (NES), exhibit strong similarities to NSA and SAM, respectively. As exemplified by the two regions in Figs. 5b-c, all tropical and subtropical areas (i.e., NWS, NSA, SAM, and NES), dominated by convective precipitation, exhibit significant similarities in the observed PDF of daily precipitation. These regions also display similar discrepancies in both WRF and ERA5, which appear to largely govern the integrated behaviors across the continent (Fig. 5a). The best agreement between IMERG and HIST is observed in SES (Fig. 5d), despite a dry bias in precipitation amounts (Fig. 3d). Unlike the low-latitude regions, in the midlatitude Andes and the southernmost parts of the continent (i.e., SWS and SSA, Figs. 5e-f), where snow predominates, both HIST and ERA5 tend to overestimate precipitation occurrence across a broad spectrum of intensities. The regional hourly precipitation PDF patterns display geographical contrasts as well, as shown in Figs 5h-l. In low-latitude regions (Figs. 5h-i), the model predicts less weak precipitation events but predicts more occurrence of intense precipitation. The PDF distributions in NES and SAM closely resemble those in NWS and NSA, respectively, and are therefore not presented. In the mid-latitude SES region (Fig. 5j), there is good agreement between the simulation and observation, except for an overestimation of light drizzle precipitation less than ≈0.2 mm/h. The high-latitude SSA region (Fig. 5l) and the southern Andes SWS (Fig. 5k) both show overestimates across nearly the entire spectrum of precipitation intensities. ERA5 reanalysis consistently produces spurious weak precipitation and lacks sufficient representation of strong precipitation across all regions, as compared to either IMERG or HIST. These results indicate that the WRF simulation effectively replicates the PDF characteristics and regional variations of both daily and hourly precipitation, performing better than the ERA5 reanalysis, with potentially excessive heavy and insufficient light precipitation, though it is possible that observational product deficiencies contribute to such differences and that HIST provides some high-resolution value over such products as well. NSA and SSE encompass the regions where precipitation biases are larger than the discrepancies among observational datasets. In both regions, hourly PDFs show underestimation of precipitation in the central part of the spectrum. This would indicate that HIST is able to provide the correct frequency of events, but of less intensity (except for NSA with larger extremes).

The diurnal cycle of warm season precipitation over land is a key aspect of weather and climate systems, primarily driven by the daily cycle of solar heating, but also influenced by various physical processes that interact in complex ways. As shown in Figs. 6a and d, South America displays a complex spatial pattern of diurnal precipitation, with notable heterogeneities in the diurnal timing of maximum hourly precipitation. It is evident that most inland areas, as well as the surrounding coastal and mountainous regions, experience peak precipitation in the afternoon and evening in both the simulation and observations (Figs. 6a-b), presumably due to moist convection and thunderstorms triggered by accumulated solar heating and the attendant buildup of atmospheric instability. In mountainous regions, elevated surface heating induces anabatic (upslope) flow, further contributing to afternoon convection initiation. Near the coast, the daytime sea breeze plays a significant role in enhancing convective development. The simulation accurately reflects the observed nocturnal and early morning timing of peak precipitation in several regions, including the Andean valleys and foothills (Poveda et al. 2005; Bedoya-Soto et al. 2019), as well as the elongated coastal hinterland that runs roughly parallel to the coastline. These patterns are likely associated with nighttime katabatic (downslope) winds in the highlands and propagating convection near the coast, respectively.

Both the simulation and observations reveal a highly coherent pattern of diurnal variation in two regions: northern Argentina and the Atlantic coastal land. In these areas, a distinct delayed diurnal phase is apparent, occurring eastward from the mountains in northern Argentina and southwestward from the coastline in the coastal region, as evidenced in the diurnal Hovmöller diagrams in Fig. 7, in association with propagating convective systems fed by nocturnal low-level jets (e.g., Salio et al. 2007; Anselmo et al. 2020). The time-longitude diagram of hourly precipitation averaged between 29-34ºS (Fig. 7a) illustrates two distinct precipitation patterns: a propagating mode and a quasi-stationary mode. The propagating mode appears to initiate over the eastern Andes in the afternoon, intensifies rapidly as it moves downstream during the evening and night, and ultimately reaches around 55°W by early morning, traveling approximately 15° of longitude. The quasi-static precipitation, extending from 50°W to 60°W, develops in the afternoon due to intense solar heating and weakens by late evening. The localized heavy precipitation near the coast is likely driven by the sea breeze. Both the propagating and stationary precipitation modes, along with the resulting consistent diurnal patterns, are reasonably well replicated (Figs. 6b and 7c), although the propagating signal is somewhat weaker and slower than its observed counterpart. Similarly, the simulation demonstrates strong skill in capturing the observed phase shift of diurnal precipitation along the Atlantic coastline, which is related to sea-breeze initiated squall lines moving westward in the easterly trade winds and low-level jet (Alcântara et al. 2011). This process begins around noon with the sea breeze near the coastline, then moves inland and persists into the following morning (Figs. 7b and d). Of note is the substantial overestimate of the afternoon–evening orographic precipitation surrounding 69°W and 65°W by both ERA5 and HIST.

Despite the strong similarity in the spatial patterns of diurnal phases, precipitation shows a more prevailing afternoon-evening peak in frequency (Fig. 6d) compared to its amount (Fig. 6a). This is primarily due to the frequent occurrence of daytime isolated convection development driven by solar insolation, but the organization of less frequent mesoscale convective systems into overnight hours. The observed timing of maximum frequency is successfully simulated across the continent (Fig. 6e), yet there is an overprediction of the nocturnal peak along the Atlantic coastal inland. One common discrepancy exists in precipitation frequency and amount: the simulated peak happens about 1-2 hours earlier than observed over many areas. This model deficiency may be attributed to the rapid growth of thermal instability driven by excessively strong surface solar radiation resulting from underpredicted cloud cover (Liu et al. 2025). Other factors may also contribute, such as overly efficient warm-cloud precipitation processes in the employed microphysics scheme and IMERG’s limited ability to detect small, isolated precipitating convection.

Once again, HIST outperforms ERA5, which tends to exhibit more widespread late morning to afternoon peaks in precipitation amount and frequency, dominating much of the continent (Fig. 6c and f). In contrast, the nighttime maximum precipitation observed in mountainous and coastal inland regions in both IMERG and HIST is nearly absent in the reanalysis. ERA5's limited performance highlights that accurately representing the diurnal precipitation cycle remains a significant challenge for coarse-resolution numerical weather and climate models, where convective parameterizations often prematurely trigger convective development during the daytime and struggle to represent the mesoscale organization of deep convection. Consistent with the incorrect diurnal phase, the propagating precipitation signature east of the southern

Andes along the 48-50°W section is weak and moves too quickly, lacking the robustness seen in both observation and HIST (Fig. 7e). Additionally, the inland penetration of coastal convection, driven by the sea breeze circulation, is too fast and short-lived (Fig. 7f). These results suggest ERA5's limited ability to generate long-lived, propagating organized convection.

3.2 Near-surface air temperature

Surface air temperature is another fundamental climate variable that influences a wide range of atmospheric and surface processes, as well as daily life. In the following, ERA5 reanalysis data are used to evaluate the simulated temperature field. HIST output is first bilinearly mapped to the ERA5 grid and then calibrated to account for the elevation difference between the WRF model and ERA5 by applying a standard atmospheric lapse rate of 6.5°C km^{-1}. The results highlight consistent performance as evidenced by the time series of monthly 2-m temperatures averaged across the land (Fig. S3), which is characterized by comparable annual cycles and inter-annual variations between HIST and ERA5, without any noticeable trend.

Figure 8 presents the monthly mean daily 2-m temperature differences between the HIST simulation and ERA5 reanalysis, calculated by averaging the instantaneous hourly fields over the 22-year period from 2000 to 2021. Also displayed are the areal mean bias, the mean absolute error (MAE), and the Pearson correlation coefficient to provide a quantitative assessment of model performance. Overall, the differences are modest year-round, typically within a range of ±2°C across most of the continent. The strong agreement between HIST and ERA5 is further attested by the high spatial pattern correlation (above 0.98), low bias (ranging from -0.8 to -0.1°C), and low MAE (below 1.1°C). These results clearly indicate the model's skill in reproducing observed near-surface temperatures across different climate zones, including the sharp transitions near the steep Andes Mountains, thanks to a more realistic depiction of complex terrain using 4-km grid spacing. Notably, the error spatial pattern features a moderate seasonality. The winter months (Figs. 8a-c) exhibit a widespread mild cold bias, with regional warm biases observed in NSA, northern Chile, and parts of southeastern Brazil. The relatively large cold bias (<-2°C) in SSA is due to underpredicted daytime temperatures, while the significant warm bias (>2°C) in the southern Andes (~20-30^{o}S) results from overpredicted nighttime temperatures. Similar wintertime deficiencies have been documented in North America (Liu et al., 2017; Rasmussen et al., 2023) and in North of Chile in previous RCM simulations (Bozkurt et al, 2019). The cold bias has been partially attributed to the inaccurate treatment of snow cover fraction (He et al., 2019; Abolafia-Rosenzweig et al., 2025), while the warm bias has been speculated to partially result from the improper handling of soil thermal conductivity in sparsely vegetated areas, likely due to the omission of soil organic matter in the land surface model (Lin et al., 2025). As the season transitions into spring (Figs. 8d-f), the warm bias of more than 1^{o}C expands across most of the interior of South America, while a weak cold bias of up to -2^{o}C is observed around the surrounding coastal areas. SSA continues to experience a cold bias, though it is weaker than that in winter. As the season progresses into summer (Figs. 8g-i), the warm bias expands further southward. The pronounced warm bias in Argentina is driven by daytime temperature overpredictions and is coupled with an apparent dry bias (Fig. 4k), suggesting a potential link to insufficient cloud coverage, rainfall, and soil moisture. This issue is prominent in coarser regional and global climate models as well (e.g., Falco et al. 2018). The fall months witness a northward spread of the cold bias, concurrent with a reduction in warm bias coverage (Figs. 8j-l). This season has the smallest MAE.

The comparison of the probability distribution (relative frequency) of 2-m temperatures in Fig. 9 provides insight into the model's ability to represent temperature distributions, variability, and extreme events, which are crucial for climate predictions. The distributions of both daily mean and hourly instantaneous temperatures span a wide range, reflecting the diverse and complex climates across the continent. The simulation closely matches the reanalysis in terms of overall shape, rightward skewness, and comparable peak magnitudes and locations. Among the variables, the daily mean temperature (Fig. 9a) is the best captured, showing strong agreement across nearly all statistical attributes. In contrast, the hourly temperature (Fig. 9b) reveals an overestimation of high-temperature events, particularly along the right tail of the distribution. Model performance shows somewhat reduced skill for diurnal maximum and minimum temperatures (Figs. 9c–d), with an overprediction of extreme daily high temperatures and an underestimation of daily cold extremes.

As exemplified by the hourly temperatures in Fig. S4, clear geographical variations exist in both the probability distribution and model performance. Note that SAM is not shown, as it closely resembles NSA except for a longer, thinner left tail. Several distinct distribution patterns are discernible in ERA5, including right-skewed (Fig. S4a), left-skewed (Fig. S4b), approximately symmetric with respect to the peak frequency (Fig. S4c), and near bell-shaped with weak skewness (Figs. S4d–f). These regional contrasts are generally well captured by the simulation. Notwithstanding, notable discrepancies remain, primarily the more frequent occurrence of high temperatures across most climate zones (Figs. S4a–e), consistent with the prevailing warm bias in maximum temperatures, and colder low temperatures in SSA (Fig. S4f), aligning with the year-round cold bias in that region (Fig. 8).

4 PGW projection

The following subsections review some key features of regional changes in near-surface air temperature and precipitation, as well as snowpack over the Andes, as projected by the PGW downscaling simulation, along with comparisons to corresponding projections from LENS2, which serves as the input to the PGW simulation.

4.1 Surface air temperature changes

The time series of monthly averaged 2-m temperature differences between the PGW and HIST simulations (Fig. 10a), averaged over all land points, show similar magnitudes without an apparent 22-year trend for daily mean temperature (T_{avg}), minimum temperature (T_{min}), and maximum temperature (T_{max}). The observed subseasonal, seasonal, and interannual variations reflect the influence of the imposed monthly varying climate signals and enhanced GHGs forcing, as well as the internal variability. The 22-year average warming amounts are 2.5°C, 2.6°C, and 2.4°C for T_{avg}, T_{min}, and T_{max}, respectively. The multi-year composite indicates a weak seasonal cycle of temperature warming (Fig. 10b), particularly for T_{avg} and T_{min}. The greater warming in T_{min} compared to T_{max} suggests a reduced diurnal temperature range during fall and winter. The PGW-projected temperature changes are slightly weaker than those from LENS2 across most seasons, with a maximum difference of ≈0.2–0.3°C in winter, due in part to the LENS2-projected hot spots along the western edge of the Amazon Basin (see later).

The PGW simulation generates widespread warming across the continent in the annual mean temperature (Fig. 11a). The weakest warming, below 2°C, is observed over the southernmost La Plata Basin, whereas the strongest warming occurs over the Andes. In the tropical and subtropical Andes, temperature increases exceed 3°C, likely linked to reduced snow precipitation (see Section 4.3 and Fig. 16) and the associated snow–albedo feedback. Similar elevation-dependent warming has been documented in both observational analyses and numerical modeling studies over the Andes and other mountain regions (Tovar et al. 2022; Chimborazo et al. 2022; Byrn et al. 2024). Additionally, a regional strong warming above 2.5°C is witnessed between the southern Amazon and northern La Plata Basins. Despite many similarities in the spatial warming patterns between the PGW simulation (Fig. 11a) and LENS2 (Fig. 11b), notable differences are present. These include hot spots exceeding 4°C along the western edge of the Amazon Basin and more pronounced warming over the Amazon in LENS2. Both are associated with significant drying (Fig. 11d), though their underlying causes remain unclear.

As shown in Fig. 12, the warming patterns display noticeable seasonal variations, although the areal averages differ only slightly. In general, winter and spring (Figs. 12a–b) closely resemble the annual warming pattern discussed above (Fig. 11a), featuring weaker midlatitude warming (1-2.5^{o}C) over Argentina and more intense warming (>3^{o}C) over parts of the western mountains and the subtropical regions to their east. Summer and fall (Figs. 12c–d) reveal different spatial patterns with relatively uniform warming (1.5-2.5^{o}C) across most of the continent, except for comparatively stronger warming (>2.5^{o}C) north of the equator, along the Andes, and in some adjacent eastern areas. Most of these features and seasonal contrasts are consistent with LENS2 (Figs. 12e–h). Perhaps the most striking discrepancy from the PGW simulation is the presence of localized warming maxima exceeding 4°C over the Peruvian Andes and broader areas of enhanced warming above 2.5°C east of the tropical and subtropical Andes, both of which contribute to the slightly greater continental-scale average warming signals in LENS2. Another distinction is that the seasonality over central Brazil differs, with peak warming occurring in spring in PGW but in winter in LENS2.

4.2 Precipitation changes

The monthly precipitation in the PGW simulation (Fig. 10c), averaged over land points, demonstrates alternating episodes of positive (wetting) and negative (drying) changes relative to the HIST simulation, resulting in a marginal overall increase when averaged over the full simulation period. Given an approximate 2.5°C warming (Fig. 10a), the domain-mean precipitation change falls well below the rate predicted by Clausius-Clapeyron scaling, indicating the importance of processes beyond thermodynamics, such as atmospheric dynamics, regional moisture availability, moisture convergence, and precipitation efficiency, in determining mean precipitation responses to climate warming in South America. The 22-year composite annual cycle (Fig. 10d) highlights drying during late winter and spring (August–November), with wetting prevailing during the remaining seasons. The PGW simulation aligns reasonably well with the LENS2 projection in terms of the seasonal pattern, but it consistently shows a wetter or less drying response compared to LENS2 during most of the year (Fig. 10d), possibly due to the warm and humid conditions imposed by the PGW forcing.

The PGW simulation projects a complex pattern of annual precipitation changes (Fig. 11c), characterized by increases over Southeast South America (SES), Northeast South America (NES), parts of Colombia, and the equatorial Pacific coast, and decreases across most regions north of the equator, southern Chile, and the western Amazon. Most of these wetting and drying features are also reflected in the LENS2 projection (Fig. 11d). These results are qualitatively consistent with the runoff differences projected by various GCMs (Müller et al. 2024). The most prominent discrepancy arises over the Amazon Basin, where LENS2 projects a substantial precipitation decline exceeding 300 mm, while the PGW simulation yields only a minimal overall reduction and even some localized increases. The origin of this difference is not yet understood, but it may partly reflect the exclusion of land use and land cover (LULC) changes in the PGW framework (see, for example, Sierra et al. 2023, where it was shown that the onset of monsoon is changed due to deforestation), as well as the omission of tropical low-frequency variability under global warming. Another notable contrast is evident over the central Andes at low latitudes, where the PGW simulation produces a mountain ridgeline-scale alternating wetting–drying pattern, in contrast to the broad-scale wetting projected by LENS2, reflecting the inability of LENS2 to resolve subranges of the Andes. When averaged across the continent, LENS2 yields a 2.7% reduction in annual precipitation, compared to a small increase of 0.2% in PGW.

Precipitation responses to climatic warming present strong seasonality, as shown in Figs. 13a–d. During the climatologically driest season, winter (Fig. 13a), widespread precipitation increases are projected, with drying primarily limited to southern Chile and the far northern continent. During spring (Fig. 13b), a marked shift toward drying emerges across much of central Brazil and Bolivia, while far southern Brazil and Uruguay undergo pronounced wetting. On the other hand, summer precipitation changes (Fig. 13c) display a dipole-like pattern, characterized by enhanced rainfall in Northeast South America (NES) and reduced rainfall in Northern South America (NSA). In fall (Fig. 13d), the wetting–drying dipole weakens considerably, while areas experiencing increased precipitation expand, particularly across the lower La Plata Basin. LENS2 exhibits seasonal precipitation patterns and transitions that mostly resemble those in the PGW simulation. In particular, the winter wetting–drying distribution (Fig. 13e) mostly mirrors that of PGW (Fig. 13a). In spring, however, LENS2 projects widespread drying over NSA (Fig. 13f), in contrast to the prevailing wetting simulated by PGW (Fig. 13b), resulting in a greater areal mean precipitation decrease in LENS2. During summer, LENS2 shows more extensive and intensified precipitation reductions across the Amazon Basin (Fig. 13g) compared to PGW (Fig. 13c). These differences reflect the annual precipitation contrasts shown in Figs. 11c-d and largely explain the divergent spatially averaged precipitation responses between the two projections. A similar divergence is evident in the fall season (Fig. 13h). Of particular note, both LENS2 and PGW consistently project year-round drying over southern Chile, likely associated with a weakening of the westerly winds in a warmer climate (Fig. 2), which would reduce orographic lifting and thus suppress local precipitation. These regional differences illustrate how thermodynamic intensification, changes in large-scale circulation, and moisture-transport pathways collectively shape South America's hydroclimate response to climate warming.

Beyond total precipitation amounts, evaluating the response of event frequency and intensity to climate warming is fundamental to understanding associated hydrological and socio-economic effects. Fig. 14 presents a comparison of the frequency of wet hours – hours in which the accumulated precipitation exceeds 0.1 mm – and the wet-hour precipitation intensity between the HIST and PGW simulations. The wet-hour frequency is calculated as the percentage of wet hours relative to the total number of hours, while the corresponding mean intensity is the average precipitation amount per wet hour. The two simulations show nearly identical spatial distributions of precipitation frequency (Figs. 14a–b), which is not surprising given their similar large-scale boundary forcing due to the relatively weak perturbations applied in the PGW framework. High-frequency regions are concentrated in the tropical and subtropical Andes, southern Chile, the northwestern Amazon, and southernmost Brazil. These patterns closely resemble the spatial distribution of annual precipitation (Fig. 3b), suggesting that total precipitation amounts are primarily governed by event frequency. Mean precipitation intensity (Figs. 14d–e) peaks in the tropics and decreases toward higher latitudes and elevations, reaching minimum values in the coldest regions of SSA and along much of the Andes. Despite the overall similarity between the two climatologies, the PGW simulation projects a widespread decline in precipitation frequency (Fig. 14c), except for modest increases over much of Argentina and northern Chile, alongside a continent-wide enhancement in intensity (Fig. 14f). As found in previous studies, the intensity of the SALLJ is projected to increase, resulting in stronger advection of warm, moist air from the Amazon Basin toward the south. This enhanced transport is reflected in reduced precipitation over northern Paraguay. On average, the projected changes indicate a decrease of 9.2% in frequency and an increase of 11.3% in intensity across the continent. These results suggest that, under climate warming, precipitation events are likely to become less frequent but more intense, consistent with findings from many other regions globally (Trenberth et al. 2003; Allan and Soden 2008; O'Gorman and Schneider 2009; Martinez-Villalobos and Neelin 2023) and with projections for parts of South America based on RCMs (Reboita et al. 2022; Lagos-Zúñiga et al. 2024).

Extreme precipitation events are among the most hazardous and consequential impacts of climate variability and change, and quantifying their response to a warming climate is therefore crucial for robust risk assessment and effective adaptation planning. Here, the 99.9th percentile of daily and hourly precipitation, as shown in Figure 15, is employed as a diagnostic metric to evaluate projected changes in extreme short-duration precipitation under the PGW framework. Like the precipitation climatology (Fig. 3b), both daily and hourly extreme precipitation (Figs. 15a and d) exhibit substantial spatial variability. The largest extremes are typically located in regions of highest annual total precipitation, such as the coastal inland of Colombia, the foothills of the tropical and subtropical Andes, and various parts of the Amazon. Conversely, the smallest extremes correspond to the driest areas, including northern Chile and southern Argentina. There is little change in the spatial pattern of extreme precipitation in the PGW simulation (Figs. 15b and e) compared to the corresponding historical counterpart (Figs. 15a and d). Although the geographical distribution remains broadly similar between the two climates, climate warming primarily leads to more intense extreme precipitation events (Figs. 15c and f). The most pronounced intensification occurs along the tropical and subtropical Pacific coasts, across most of Argentina, and to a lesser extent in southeastern Brazil. On the other hand, slight reductions are found in some scattered regions, including parts of the northern coastal areas and southern Chile. On average across the continent, extreme daily and hourly precipitation amounts increase by 13.1% and 12.5%**,** respectively, both of which are slightly lower than the Clausius-Clapeyron (CC) scaling rate of ≈7% per degree Celsius, given the mean warming of 2.4°C. Of particular interest is that the largest increases in extreme precipitation, often surpassing the CC scaling, tend to coincide with regions experiencing the greatest increases in total precipitation (Fig. 11c), as well as with the areas of weakest warming in Argentina (Fig. 11a). Additionally, extreme precipitation increases dominate across the continent, exhibiting a much broader spatial extent than overall precipitation increases.

4.3 Snowpack changes

In South America, snowpack functions as a vital natural reservoir whose spring snowmelt runoff supports agriculture and hydropower in the countries bordering the Andes Mountains (e.g., Masiokas et al. 2006; Mendoza et al. 2014; Cornwell et al. 2016; Hernandez et al. 2022; Araya et al. 2023). As shown by the 22-year mean snow water equivalent (SWE) in Fig. 16d, snowpack in South America is primarily concentrated in the high mountainous regions of the Andes, which stretch along the western margin of the continent from Venezuela in the north to southern Chile and Argentina. SWE generally increases southward, reaching its maximum in the southern Andes and Patagonia, closely mirroring the spatial distribution of snowfall shown in Fig. 16c. Under warmer conditions, total precipitation (Fig. 16e) features a clear reduction across much of the central Andean ridge, where snowpack commonly resides. An exception is found in northern Chile, where the windward slopes experience modest increases in precipitation. Similar spatial patterns appear in the differential rainfall field (Fig. 16f), though the reduction covers a slightly smaller area. On the other hand, snowfall decreases almost everywhere, with the largest absolute declines occurring in the southernmost Andes and the Patagonian region, areas that coincide with the deepest historical snowpack and extensive glaciers (Fig. 16d), as well as in the high-altitude regions of Peru and Bolivia (Fig. 16g). This widespread reduction in snowfall, combined with increased melting driven by rising temperatures, contributes significantly to the observed snowpack shrinkage across South America (Fig. 16h). The areal average SWE is projected to decrease by ≈10% across the entire continent, with the largest relative reductions occurring in the tropical Andes, where climatological SWE values are already low. These results are consistent with observed snowpack and glacier declines in the region (Masiokas et al. 2006; Saavedra et al. 2018; Aranda et al. 2023) and with the snowpack contraction projected for the coming decades (e.g., Caro et al. 2025; Vásquez et al. 2025; Al-Yaari et al. 2024), which could have substantial societal and economic consequences.

5 Discussion and conclusions

5.1 Summary of the downscaling simulations

In this study, a pair of multi-year, high-resolution regional climate downscaling simulations was conducted using the WRF model at 4-km horizontal grid spacing over a domain encompassing the entire South American continent and adjacent oceans. The simulation suite includes a 22-year historical climate run, which downscales ERA5 reanalysis data for the 2000–2021 period, and a 22-year PGW-based climate run, representing late-century conditions centered on a projected global warming of ~3°C relative to the preindustrial baseline. In the PGW simulation, ERA5 data are perturbed using a climate change signal derived from a large ensemble of CESM2 projections (LENS2) for the period 2060-2080 under the CMIP6 SSP3-7.0 scenario, corresponding to a ~2.5°C regional warming above the 2000–2020 baseline in South America. This modeling effort represents a first-of-its-kind effort for the region, integrating a continental-scale domain, convection-permitting resolution, and a multi-decadal simulation period. The primary purpose is to generate a long-term high-resolution (hourly, kilometer-scale) dataset to support regional climate and hydrometeorological research across South America. To facilitate a broad range of scientific applications within the SAAG community as detailed in Dominguez et al. (2024), the simulations archive all conventional three-dimensional and 100+ two-dimensional atmospheric, near-surface, and land physical variables at hourly resolution, along with 15-minute outputs for a subset of selected variables. This comprehensive dataset serves as a valuable resource for diverse research communities and as a complementary tool for policymaking.

The accuracy and performance of the historical simulation in reproducing precipitation and near-surface air temperature were evaluated against multiple gridded precipitation datasets and ERA5 2-m temperature data. The analysis supports the following key conclusions:

1) *High skill in multiscale precipitation representation*: The 4-km WRF model demonstrates strong capability in capturing precipitation variability across temporal scales ranging from interannual to hourly. It accurately reproduces observed spatial patterns of annual and seasonal precipitation, the monthly progression of rainfall linked to monsoon dynamics, and a variety of diurnal precipitation regimes. Importantly, the model captures the propagation of precipitation through the overnight hours in the lee of the midlatitude Andes and inland from the Atlantic coast, as well as the full distribution spectrum of daily and hourly precipitation intensities. The majority of model deviations relative to satellite-derived precipitation estimates fall within the bounds of observational uncertainty. Nonetheless, significant differences remain, particularly across the Andes Mountains, necessitating further investigation into the respective roles of observational product uncertainties and WRF model deficiencies.
2) *Effective performance in temperature representation*: The model realistically simulates seasonal and sub-seasonal near-surface air temperatures and reproduces the probability distributions of both daily and hourly temperature values with reasonable accuracy.

3) *WRF added value over ERA5*: While ERA5 and WRF exhibit similar skill in capturing large-scale variability in precipitation (interannual to sub-seasonal), WRF substantially outperforms ERA5 in representing the diurnal cycle, simulating propagating precipitation, and capturing daily to hourly precipitation features, compared to IMERG estimates. Further, WRF provides a more accurate representation of precipitation extremes, offering enhanced value for studying high-impact weather events and climate applications.

Additional evaluation studies have provided evidence for the capability of this high-resolution historical simulation to reproduce the climatological characteristics of various weather systems over South America. For example, Potter (2023) demonstrated that the simulation captures the climatological pattern of orographic precipitation over the Chilean and Argentinian Andes but exhibits a wet bias in the northern domain and in some areas immediately leeward of the crest, while accurately reproducing the observed contribution of atmospheric rivers to Andean rainfall. Zilli et al. (2024) examined the simulation of tropical–extratropical cloud bands, the primary source of precipitation during the South American rainy season (November–March), and found that the simulated annual cycle of cloud band days deviates by only about 10% from observations. Similarly, Rehbein et al. (2025) evaluated the representation of MCSs and reported that key characteristics such as size, duration, and maximum precipitation are generally well captured by the model, despite a slight positive bias in maximum precipitation. Moreover, the WRF simulation was shown to successfully replicate many key characteristics of the interactions between SALLJs and MCSs, including the observed spatial patterns of MCS initiation and precipitation associated with different types of SALLJs, particularly the enhanced activity over SES (Mu et al., 2025). In summary, the dynamical downscaling using the convection-permitting WRF model substantially improves the representation of a wide range of physical processes, offering significant added value over the driving reanalysis. The model's strong overall performance builds confidence in its use for both process-level investigations and applied studies and supports the continued use of this configuration for future climate downscaling efforts.

An analysis of the PGW simulation was conducted to examine projected changes in surface air temperature, key precipitation characteristics, and snowpack, alongside a comparison with the driving CESM-LENS2 projection for the late 21st century (2060–2080). The main findings are summarized as follows:

1) *Substantial surface warming*: The PGW simulation projects an average surface temperature increase of approximately 2.4°C, with the strongest warming occurring in the Andes and subtropical regions. While the spatially averaged warming magnitude and many regional and seasonal features are broadly consistent with the CESM-LENS2 projection, regional differences are evident, likely stemming in part from differences in representations of land-surface processes and land-atmosphere interactions.
2) *Regional shifts in precipitation patterns*: Projected precipitation changes vary by region and season. Drying is anticipated in southern Chile and the western Amazon, while wetter conditions are expected in southeastern South America and along portions of the Pacific coast. Seasonal signals include wetter winters and drier springs. A significant divergence between the PGW simulation and CESM-LENS2 occurs over the Amazon, where the latter projects significantly greater drying.
3) *Changes in precipitation frequency and intensity*: The PGW simulation indicates a 9.2% reduction in the frequency of rainy days, coupled with an 11.3% increase in rainfall

intensity. Extreme precipitation events (99.9th percentile) are projected to intensify on both daily and hourly timescales. These results are consistent with the broader expectation that global warming will lead to fewer but more intense storms.

4) *Declining snowpack in the Andes*: The domain-average snowpack is projected to decline by roughly 10%, driven by both reduced snowfall and increased melting under warmer temperatures. This decline has potential implications for water availability, agriculture, and hydropower in high-altitude regions reliant on seasonal snowmelt.

Among many others, one application is particularly compelling for hydroclimate research. The Noah-MP land surface model with groundwater coupling (Miguez-Macho and Fan 2007; Niu et al. 2011) enables the SAAG simulations to resolve soil moisture and subsurface storage, providing an internally consistent representation of terrestrial water storage (TWS). As an integrative component, TWS links atmospheric inputs such as precipitation and snowmelt with losses through evapotranspiration, thereby shaping the persistence and propagation of hydrological anomalies across the landscape. This capability is particularly important because recent analyses using GRACE and GRACE-FO have established TWS anomalies as fundamental for understanding droughts and floods in South America, especially in the Amazon and La Plata basins (Chen et al. 2009, 2010; Humphrey et al. 2016; Getirana et al. 2020; Camacho et al. 2023). The inclusion of these subsurface processes therefore extends the scope of the SAAG dataset far beyond surface fluxes and offers a powerful tool for investigating how soil moisture and groundwater memory modulate the intensity, duration, and recovery of hydroclimatic extremes under both present and future climates.

5.2 Limitations and future work

The merits and limitations of the PGW technique have been thoroughly discussed in the literature (Liu et al. 2017, 2024; Brogli et al. 2023; Hall et al. 2024). In brief, PGW simulations are valuable for quantifying the more deterministic thermodynamic component of increasing greenhouse forcing, while avoiding the complications of unpredictable internal variations from individual GCM projections. This offers a distinct advantage over traditional dynamical downscaling, where a single GCM realization is typically used to provide boundary conditions for RCMs. Additionally, the climate forcing (i.e., Eqs. 1-2) represents the difference between two ensemble mean climates, which helps mitigate the systematic biases inherent in GCMs. Finally, the PGW technique enables direct comparisons between a historical year and the corresponding "future" (PGW) year in the context of current day interannual variability, due to the comparable daily weather perturbations between the PGW and baseline boundary forcings. The major criticism to the approach is its inability to address the future variability of synoptic-scale storms entering the study domain (Hall et al. 2024; Xu et al. 2019), as well as not being able to provide any information related to changes (e.g., frequency, intensity, extent) in climate systems (e.g., ITCZ, ENSO, SAMS, MJO) that have a strong influence on South America.

Despite its overall positive performance, the current WRF modeling system still suffers from weaknesses that must be addressed to improve historical hydroclimate simulations and potentially reduce uncertainties in future projections, although limitations in coarse-resolution gridded satellite observations (Müller et al. 2021; Liu et al. 2025) complicate their interpretation. Among these are several persistent model deficiencies, most notably, the excessive precipitation biases over major mountain ranges such as the Andes and the Guiana Highlands (Figs. 3–4). As identified by Liu et al. (2025), a root cause of this orographic wet bias lies in the underrepresentation of clouds in WRF simulations. This deficiency leads to excessive surface solar radiation, which can drive unrealistically strong thermal instability and anabatic (upslope) flows. The enhanced instability and upslope winds, combine to trigger orographic convection that is too early and too intense during the daytime, ultimately contributing to the overestimation of mountain precipitation. To effectively address this issue, future efforts should prioritize improving cloud representation, particularly non-precipitating clouds, which are critical to the radiation budget but frequently underrepresented in high-resolution WRF simulations (Kim et al. 2025). Specifically, incorporating a shallow cumulus cloud parameterization appears necessary for representing subgrid-scale cloud processes that remain unresolved at convection-permitting resolutions. Although such a scheme is currently unavailable in the present WRF model configuration, its inclusion might result in a meaningful improvement in the simulation of orographic precipitation. Additionally, even with accurate orographic cloud formation, cumulus congestus clouds were nonetheless found to precipitate too efficiently in WRF simulations employing the same microphysics scheme as in the present study, leading to excessive orographic convective precipitation (Zhang et al. 2024). Furthermore, a 4-km horizontal grid spacing is insufficient to resolve deep convective updrafts (e.g., Bryan et al. 2003), producing overly broad updrafts with biased velocities and vertical transport (e.g., Varble et al., 2020; Wang et al., 2020). These biases subsequently influence the convective-stratiform precipitation partitioning (e.g., Han et al. 2019). Consequently, smaller-scale regional comparisons that integrate large-eddy simulations and detailed limited-domain observations with large-domain, long-duration simulations will be essential for advancing km-scale model performance.

Another issue involves the use of present-day land use and land cover (LULC) in the PGW simulation, which does not account for potential future changes and thus introduces additional uncertainty into the projection. LULC changes, particularly deforestation and agricultural expansion, exert significant influence on South America's regional climate by modifying surface water and energy fluxes, evapotranspiration, and moisture recycling (Feddema et al. 2005; Bonan, 2008; Wongchuig et al. 2023). For instance, the Amazon rainforest, a critical component of the continent's hydrological system, plays a major role in maintaining atmospheric humidity and precipitation through strong evapotranspiration (Salati and Vose 1984; Spracklen et al. 2012; Wright et al. 2017). Large-scale deforestation reduces canopy cover and soil moisture retention, resulting in elevated surface temperatures and suppressed local rainfall (Lawrence and Vandecar 2015; Alkama and Cescatti 2016; Lima et al. 2023). Similar processes are found in the Dry Chaco (Bracalenti et al. 2024). These changes can disrupt the South American monsoon system (Sierra et al. 2023) and weaken precipitation recycling, with far-reaching consequences for water availability across the region (Nobre et al. 2009; Poveda et al. 2014; Marengo et al. 2018). Moreover, alterations in land surface properties affect boundary-layer dynamics, atmospheric circulation, and cloud formation, underscoring the importance of LULC changes in accurately simulating and projecting regional climate variability (Pielke et al. 2007; Pitman et al. 2009; Eiras-Barca et al. 2020). Consequently, the integration of dynamic land use processes into high-resolution climate models is essential for improving the assessment of future climate changes in South America (Devaraju et al. 2015; Boisier et al. 2015), a topic currently being explored in a separate SAAG community effort.

Another limitation of these simulations is the use of fixed (default) parameter values in the Noah-MP land surface model. Parameter uncertainties can strongly influence land–atmosphere water and energy exchanges simulated by land models (e.g., Rosero et al. 2010; Sepúlveda et al. 2022; Elkouk et al. 2024), thereby affecting other terrestrial water and energy storages. This is also true for Noah-MP, whose sensitivity to both “free” parameters (e.g., coefficients used in conceptual baseflow and surface runoff parameterizations) and “observable” parameters (e.g., saturated hydraulic conductivity, soil porosity, vegetation height) has been well documented (e.g., Cai et al. 2014; Mendoza et al. 2015b; Cuntz et al. 2016; Arsenault et al. 2018). In particular, Mendoza et al. (2015b) demonstrated the substantial influence of hidden (i.e., hard-coded) parameters, including those in the snowpack module, on model behavior, while Arsenault et al. (2018) identified the most influential parameters governing surface heat fluxes, soil moisture, and net carbon flux when using Noah-MP with dynamic vegetation. Importantly, parameter uncertainties can significantly alter both the sign and magnitude of projected changes in water-cycle variables, as shown by Mendoza et al. (2015a). Hence, future investigations should aim to develop improved and spatially coherent parameter estimates across the South American continent to enable more robust representations of snow, soil moisture, runoff, evapotranspiration, groundwater, and other hydrological variables under both historical and future climate conditions.

Lastly, aerosols exert a significant yet complex influence on South American weather and climate systems through both direct and indirect pathways. Directly, they affect the regional radiation budget by scattering and absorbing incoming solar radiation (Haywood and Boucher 2000). Indirectly, aerosols modify cloud microphysical properties, such as droplet numbers and sizes, thereby influencing cloud albedo, lifetime, coverage, and precipitation efficiency (Twomey 1977; Rosenfeld et al. 2008). In the Amazon Basin, aerosol emissions from biomass burning, originating from both natural processes and anthropogenic activities, can suppress or enhance convective precipitation by altering cloud formation and atmospheric stability (Andreae et al. 2004; Martins et al. 2009; Wu et al. 2021; Curtius et al. 2024). These interactions are particularly critical during the dry-to-wet season transition, when aerosol–cloud interactions have the potential to delay the onset of the South American Monsoon (Zhang et al. 2009; Spracklen et al. 2012). Furthermore, elevated aerosol concentrations can reduce surface-reaching solar radiation, weakening the surface energy budget and modifying local and regional circulation patterns (Koren et al. 2004; Butt et al. 2022). Despite their demonstrated importance, aerosols remain a major source of uncertainty in regional climate modeling due to their high spatial and temporal variability, as well as the complex, nonlinear interactions with clouds and land–atmosphere feedbacks (IPCC 2021; Bonini et al. 2023; He et al. 2024). In the current experimental configuration, aerosol–radiation interactions are represented using a prescribed $5° \times 4°$ 1990s aerosol climatology within the RRTMG radiation scheme, and aerosol–cloud interactions are entirely absent, as the employed microphysics scheme assumes a fixed cloud droplet number concentration. As a result, the suppression of warm rain by aerosols and the associated modifications to mixed-phase processes in convective clouds are not captured. Even microphysics schemes that include aerosol–cloud interactions often struggle to reproduce observed cloud and precipitation characteristics, highlighting the need for further research to advance cloud microphysical modeling and improve precipitation prediction (e.g., Morrison et al. 2020). The omission of dynamically evolved aerosol fields thus introduces an additional source of uncertainty in both historical and future climate simulations, particularly in regions such as the Amazon, where these feedbacks are known to be substantial.

In conclusion, this study provides a much-needed high-resolution long-term dataset that not only advances scientific understanding of South American climate dynamics under present and future forcing scenarios but also serves as a foundation for applied research. The dataset enables investigations of extreme weather events, assessments of climate impacts on water resources, and integrated evaluations of regional vulnerability and adaptation strategies. These capabilities are essential for supporting climate resilience, informing policy development, and guiding national and regional planning in the context of a changing climate. Additionally, the dataset presents new opportunities to force hydrological and land surface models (e.g., Segovia et al., 2025), thereby enhancing impact modeling and decision-support systems. A further strength of the dataset is that, through Noah-MP with groundwater coupling, it explicitly accounts for soil moisture, groundwater, and thus TWS. While this study focused on precipitation and snowpack, the availability of multi-decadal, convection-permitting TWS fields significantly enhances the dataset’s value for the community. It enables investigations of drought persistence, hydrological resilience, and long-term water-cycle variability across South America. Nonetheless, further efforts are required to reduce remaining uncertainties by improving model physics and Noah-MP parameter estimates, and incorporating currently missing processes, particularly those related to subgrid cloud dynamics and microphysics, LULC changes, and aerosol–cloud-radiation interactions. Future extensions of the SAAG effort will emphasize the integration of additional variables (e.g., soil moisture, evapotranspiration, and energy fluxes) and the development of user-friendly tools for applied sectors, including agriculture, water management, and disaster risk reduction.

Acknowledgements

This research was supported by the National Science Foundation under the NCAR Water System Program. We would like to acknowledge high-performance computing support from Cheyenne (doi:10.5065/D6RX99HX) provided by NCAR's Computational and Information Systems Laboratory's University Large Allocation, sponsored by the National Science Foundation (NSF) and award AGS 185270 from NSF. Lucia Scaff and Miguel Lagos-Zúñiga acknowledge the support of the supercomputing infrastructure of the NLHPC (CCSS210001), Powered@NLHPC. Santiago Nuñez Mejia acknowledges the SWACH project (VLIR TEAM EC2022TEA512A1) for supporting his participation in the SAAG discussions as part of his doctoral research. The Pacific Northwest National Laboratory is operated by the Battelle Memorial Institute under contract no. DE-AC06-76RLO1830.

References

Abolafia-Rosenzweig, R., He, C., Liu, C., Lin, T.-S., Mocko, D., Rittger, K., et al. (2025) Snow cover plays a non-dominant role in WRF/Noah-MP simulated surface air temperature cold biases over the western U.S. Journal of Geophysical Research: Atmospheres, 130, e2025JD044191. https://doi-org.cuucar.idm.oclc.org/10.1029/2025JD044191

Adam O, Schneider T, Brient F (2020) Regional and seasonal variations of the double-ITCZ bias in CMIP5 models. Clim Dyn 51:101–117

Adler, R.F., G.J. Huffman, A. Chang, R. Ferraro, P. Xie, J. Janowiak, B. Rudolf, U. Schneider, S. Curtis, D. Bolvin, A. Gruber, J. Susskind, and P. Arkin (2003) The Version 2 Global Precipitation Climatology Project (GPCP) Monthly Precipitation Analysis (1979-Present). J. Hydrometeor., 4,1147-1167.

Alcântara, C. R., M. A. S. Dias, E. P. Souza, and J. C. Cohen (2011) Verification of the role of the low level jets in Amazon squall lines. Atmos. Res., 100, 36–44, https://doi.org/10.1016/j.atmosres.2010.12.023.

Alkama, R., and Cescatti, A. (2016) Biophysical climate impacts of recent changes in global forest cover. *Science*, 351(6273), 600–604.

Allan, R. P., and Soden, B. J. (2008) Atmospheric warming and the amplification of precipitation extremes. *Science*, **321**(5895), 1481–1484. https://doi.org/10.1126/science.1160787

Al-Yaari, A., Condom, T., Anthelme, F., Cauvy-Fraunié, S., Dangles, O., Junquas, C., ... & Rabatel, A. (2024). Warming-induced cryosphere changes predict drier Andean eco-regions. Environmental Research Letters, 19(10), 104030.

Andreae, M. O., Rosenfeld, D., Artaxo, P., et al. (2004) Smoking rain clouds over the Amazon. *Science*, 303(5662), 1337–1342.

Anselmo, E. M., C. Schumacher, and L. A. T. Machado (2020) The Amazonian low-level jet and its connection to convective cloud propagation and evolution. Mon. Wea. Rev., 148, 4083–4099, https://doi.org/10.1175/MWR-D-19-0414.1.

Aranda, F., Medina, D., Castro, L., Ossandón, Á., Ovalle, R., Flores, R. P., & Bolaño-Ortiz, T. R. (2023) Snow persistence and snow line elevation trends in a Snowmelt-Driven Basin in the Central Andes and their correlations with hydroclimatic variables. Remote Sensing, 15(23), 5556.

Araya, D., Mendoza, P. A., Muñoz-Castro, E., & McPhee, J. (2023) Towards robust seasonal streamflow forecasts in mountainous catchments: impact of calibration metric selection in hydrological modeling. Hydrology and Earth System Sciences, 27(24), 4385-4408.

Arias, P.A., Correa, I.C., Fita, L. et al. (2025) How well CMIP6 models simulate key boundary conditions affecting South American climate? Insights for regional modeling efforts. Clim Dyn 63, 231. https://doi.org/10.1007/s00382-025-07704-w

Arsenault, K. R., Nearing, G. S., Wang, S., Yatheendradas, S., & Peters-Lidard, C. D. (2018) Parameter sensitivity of the Noah-MP land surface model with dynamic vegetation. Journal of Hydrometeorology, 19(5), 815-830.

Ayat H, Evans JP, Sherwood S, Behrangi A (2021) Are storm characteristics the same when viewed using merged surface radars or a merged satellite Pproduct? J Hydrometeorol 22(1):43–62. https://doi.org/10.1175/jhm-d-20-0187.1

Ban, N., et al. (2014) Evaluation of the COSMO-CLM regional climate model in climate simulations over Europe. *Climate Dynamics*, 42(9–10), 2747–2764.

Ban, N., Schmidli, J., & Schär, C. (2014) Evaluation of the convection-resolving regional climate modeling approach in decade-long simulations. *Journal of Geophysical Research: Atmospheres*, 119(13), 7889–7907.

Ban, N., Caillaud, C., Coppola, E., et al. (2021) The first multi-model ensemble of regional climate simulations at kilometer-scale resolution, part I: evaluation of precipitation. Clim. Dyn. 57, 275–302. https://doi.org/10.1007/s00382-021-05708-w

Beck, H. E., Wood, E. F., Pan, M., Fisher, C. K., Miralles, D. M., van Dijk, A. I. J. M., McVicar, T. R., and Adler, R. F. (2019) MSWEP V2 global 3-hourly 0.1° precipitation: methodology and quantitative assessment Bulletin of the American Meteorological Society 100(3), 473–500.

Bedoya-Soto, J.M., E. Aristizábal, A.M. Carmona, and G. Poveda (2019) Seasonal shift of the diurnal cycle of rainfall over Medellin's valley, Central Andes of Colombia (1998–2005). Frontiers in Earth Science, Atmospheric Science. 7:92. doi: 10.3389/feart.2019.00092.

Berbery, E. H., & Barros, V. R. (2002) The hydrologic cycle of the La Plata basin in South America. Journal of Hydrometeorology, 3(6), 630-645.

Bettolli ML, et.al. (2021) The CORDEX Flagship Pilot Study in southeastern South America: a comparative study of statistical and dynamical downscaling models in simulating daily extreme precipitation events. Climate Dynamics. 56: 1589-1608; DOI: https://doi.org/10.1007/s00382-020-05549-z

Betts, A. K., & Viterbo, P. (2005) Land-surface, boundary layer, and cloud-field coupling over the southwestern Amazon in ERA-40. Journal of Geophysical Research: Atmospheres, 110(D14).

Boers, N., Marwan, N., Barbosa, H. M. J., & Kurths, J. (2017) A deforestation-induced tipping point for the South American monsoon system. Scientific Reports, 7 (1), 41489. doi: 10.1038/srep41489

Boisier, J. P., et al. (2015) Evaluation of rainfall simulations in the Amazon basin using the WRF model. *Climate Dynamics*, 44(1-2), 249–273.

Bonan, G. B. (2008) Forests and climate change: Forcings, feedbacks, and the climate benefits of forests. *Science*, 320(5882), 1444–1449.

Bonini, R., et al. (2023) Aerosol–cloud–radiation interactions in South America: Current understanding and challenges. *Atmospheric Chemistry and Physics*, 23, 2517–2535.

Bozkurt, D., Rojas, M., Boisier, J. P., Rondanelli, R., Garreaud, R., & Gallardo, L. (2019) Dynamical downscaling over the complex terrain of southwest South America: present climate conditions and added value analysis. Climate Dynamics, 53(11), 6745-6767.

Bracalenti, M. A., Müller, O. V., Lovino, M. A., and Berbery, E. H. (2024) The agricultural expansion in South America's Dry Chaco: regional hydroclimate effects, Hydrol. Earth Syst. Sci., 28, 3281–3303, https://doi.org/10.5194/hess-28-3281-2024.

Brogli, R., Heim, C., Mensch, J., Sørland, S. L., and Schär, C. (2023) The pseudo-global-warming (PGW) approach: methodology, software package PGW4ERA5 v1.1, validation, and sensitivity analyses, Geosci. Model Dev., 16, 907–926, https://doi.org/10.5194/gmd-16-907-2023.

Bryan, G. H., Wyngaard, J. C., & Fritsch, J. M. (2003) Resolution requirements for the simulation of deep moist convection. Monthly Weather Review, 131(10), 2394–2416. https://doi.org/10.1175/1520-0493(2003)131<2394:RRFTSO>2.0.CO;2

Butt, N., de Oliveira, P. J. C., & Costa, M. H. (2022) Aerosol-induced surface cooling and Amazon rainfall suppression. *Environmental Research Letters*, 17(2), 024023.

Byrne, M.P., W.R. Boos, and S. Hu (2024) Elevation-dependent warming: observations, models, and energetic mechanisms. Weather Clim. Dynam., 5, 763–777, https://doi.org/10.5194/wcd-5-763-2024

Cai, W., McPhaden, M.J., Grimm, A.M., et al. (2020) Climate impacts of the El Niño–Southern Oscillation on South America. Nat. Rev. Earth Environ. 1, 215–231. https://doi.org/10.1038/s43017-020-0040-3.

Cai, X., Yang, Z. L., David, C. H., Niu, G. Y., & Rodell, M. (2014) Hydrological evaluation of the Noah-MP land surface model for the Mississippi River Basin. Journal of Geophysical Research: Atmospheres, 119(1), 23-38.

Camacho, C., Getirana, A., Rotunno F., Otto and Mourao, M. A. (2023) Large-Scale Groundwater Monitoring in Brazil Assisted With Satellite-Based Artificial Intelligence Techniques. Water Resources Research. 59. 10.1029/2022WR033588.

Campos, D., & Rondanelli, R. (2023) ENSO-related precipitation variability in Central Chile: The role of large scale moisture transport. Journal of Geophysical Research: Atmospheres, 128(17), e2023JD038671.

Caro, A., Condom, T., Rabatel, A., Aguayo, R., & Champollion, N. (2025) Future glacio-hydrological changes in the Andes: a focus on near-future projections up to 2050. Scientific Reports, 15(1), 10991.

Carvalho, L.M.V., Jones, C. and Liebmann, B. (2002) Extreme precipitation events in southeastern South America and large-scale convective patterns in the South Atlantic covergence zone. Journal of Climate, 15(17), 2377–2394. https://doi.org/10.1175/1520-0442(2002)015<2377:EPEISS>2.0.CO;2.

Carvalho, Leila M. V.; Charles Jones & Brant Leibman (2003) "The South Atlantic Convergence Zone: Intensity, Form, Persistence, and Relationships with Intraseasonal to Interannual Activity and Extreme Rainfall" (PDF). Journal of Climate, vol. 17, pp. 88. Retrieved 2009-06-05

Cecil, D.J., D.E. Buechler, R.J. Blakeslee (2015) TRMM LIS climatology of thunderstorm occurrence and conditional lightning flash rates J. Clim., 28, 6536-6547. DOI: 10.1175/JCLI-D-15-0124.1

Cecil, D. J., and C. B. Blankenship (2012) Toward a global climatology of severe hailstorms as estimated by satellite passive microwave imagers. J. Climate, 25, 687–703, doi:10.1175/JCLI-D-11-00130.1.

Chen, J., Wilson, C., Tapley, B., Yang, Z., and Niu, G. (2009) 2005 Drought event in the Amazon River basin as measured by GRACE and estimated by climate models. Journal of Geophysical Research. 114. B05404. 10.1029/2008JB006056.

Chen, J. L., C. R. Wilson, B. D. Tapley, L. Longuevergne, Z. L. Yang, and B. R. Scanlon (2010) Recent La Plata basin drought conditions observed by satellite gravimetry, *J. Geophys. Res.*, 115, D22108, doi:10.1029/2010JD014689.

Chen, M., P. Xie, and Co-authors (2008) CPC Unified Gauge-based Analysis of Global Daily Precipitation, Western Pacific Geophysics Meeting, Cairns, Australia, 29 July - 1 August 2008.

Chimborazo, O., Minder, J. R., and Vuille, M. (2022) Observations and simulated mechanisms of elevation-dependent warming over the Tropical Andes, J. Climate, 35, 1021–1044, https://doi.org/10.1175/JCLI-D-21-0379.1

Chou, S. C., et al. (2014) Evaluation of the Eta simulations nested in three global climate models. *American Journal of Climate Change*, 3(3), 438–454.

Christensen, J. H., et al. (2007) Regional climate projections. In: *Climate Change 2007: The Physical Science Basis*. IPCC AR4, Cambridge University Press.

Claros, E., & Kuroiwa, J. M. (2025) Can Non-Euclidean Distances Improve Spatial Interpolation of Precipitation in Mountainous Regions? International Journal of Climatology, e70071. https://doi.org/10.1002/joc.70071

Coppola, E., et al. (2020) Climate hazard indices projections based on CORDEX-CORE, CMIP5 and CMIP6 ensemble. *Climate Dynamics*, 55, 733–752.

Coppola, E., et al. (2021) A first-of-its-kind multi-model convection-permitting ensemble for investigating convective extremes in South America. *Earth System Dynamics*, 12(1), 97–128.

Cornwell E, Molotch NP, McPhee J. (2016) Spatio-temporal variability of snow water equivalent in the extra-tropical Andes Cordillera from distributed energy balance modeling and remotely sensed snow cover. Hydrology and Earth System Sciences 20 (1): 411–430 DOI: 10.5194/hess-20-411-2016

Crespo, N. M., Reboita, M. S., Gozzo, L. F., de Jesus, E. M., Torres-Alavez, J. A., Lagos-Zúñiga, M. Á., ... & da Rocha, R. P. (2023) Assessment of the RegCM4-CORDEX-CORE performance in simulating cyclones affecting the western coast of South America. Climate Dynamics, 60(7), 2041-2059.

Cui, W., Dong, X., Xi, B., Feng, Z., Fan, J. (2020) Can the GPM IMERG Final Product Accurately Represent MCSs' Precipitation Characteristics over the Central and Eastern United States? J. Hydrometeorol. 21, 39–57.

Cuntz, M., Mai, J., Samaniego, L., Clark, M., Wulfmeyer, V., Branch, O., ... & Thober, S. (2016) The impact of standard and hard-coded parameters on the hydrologic fluxes in the Noah-MP land surface model. Journal of Geophysical Research: Atmospheres, 121(18), 10-676.

Curtius, J., Heinritzi, M., Beck, L.J. et al. (2024) Isoprene nitrates drive new particle formation in Amazon's upper troposphere. Nature 636, 124–130. https://doi.org/10.1038/s41586-024-08192-4

Dai, A. (2006) Precipitation characteristics in eighteen coupled climate models. *Journal of Climate*, 19, 4605–4630. https://doi.org/10.1175/JCLI3884.1

Dai, A., R. M. Rasmussen, K. Ikeda, and C.-H. Liu (2020) A new approach to construct representative future forcing data for dynamic downscaling. Clim. Dyn., 55, 315-323. DOI 10.1007/s00382-017-3708-8.

de Medeiros, F.J.; de Oliveira, C.P.; Avila-Diaz, A. (2022) Evaluation of extreme precipitation climate indices and their projected changes for Brazil: From CMIP3 to CMIP6. Weather. Clim. Extrem. 38, 100511.

da Rocha, R.P., Llopart, M., Reboita, M.S. et al. (2024) Precipitation Diurnal Cycle Assessment in Convection-Permitting Simulations in Southeastern South America. Earth Syst Environ 8, 1–19. https://doi.org/10.1007/s41748-023-00361-1

Devaraju, N., Bala, G., & Modak, A. (2015) Effects of large-scale deforestation on precipitation in the monsoon regions: Remote versus local effects. *Environmental Research Letters*, 10(10), 104006.

Dominguez, F., Eiras-Barca, J., Yang,Z., Bock, D., Nieto, R., & Gimeno, L. (2022) Amazonian moisture recycling revisited using WRF with water vapor tracers. Journal of Geophysical Research: Atmospheres,127, e2021JD035259. https://doi.org/10.1029/2021JD035259

Dominguez, F., Rasmussen, R., Liu, C.-H., Ikeda, K., Prein, A., co-authors (2024) Advancing South American water climate science through multidecadal convection permitting modeling. Bull. Am. Meteorol. Soc. 105, E32–E34. https://doi.org/ 10.1175/ BAMS-D-22-0226.1

Done JM, Holland GJ, Bruyère CL et al (2015) Modeling high-impact weather and climate: lessons from a tropical cyclone perspective. Clim Change 129(3):381–395. doi:10.1007/s10584-013-0954-6

Drumond, A., et al. (2014) The role of the Amazon Basin moisture in the atmospheric branch of the hydrological cycle: A Lagrangian analysis. *Hydrology and Earth System Sciences*, 18(7), 2577–2598.

Duffy, P. B., et al. (2003) Strengths and limitations of GCMs in simulating South American climate. *Climatic Change*, 58(1-2), 89–111.

Durkee, J. D. and T. L. Moteb (2009) A climatology of warm-season mesoscale convective complexes in subtropical South America. Int. J. Climatol. i30, 418-431. DOI: 10.1002/joc.1893

Ehret, U., et al. (2012) Hydroclimate data analysis and modeling: A look at recent advancements. *Hydrology and Earth System Sciences*, 16(9), 3263–3270.

Eiras-Barca, J., Dominguez, F., Yang, Z., Chug, D., Nieto, R., Gimeno, L. and Miguez-Macho, G. (2020) Changes in South American hydroclimate under projected Amazonian deforestation. Ann. N.Y. Acad. Sci., 1472: 104-122. https://doi-org.cuucar.idm.oclc.org/10.1111/nyas.14364

Elkouk, A., Pokhrel, Y., Livneh, B., Payton, E., Luo, L., Cheng, Y., ... & Thiery, W. (2024) Toward understanding parametric controls on runoff sensitivity to climate in the community land model: A case study over the Colorado River headwaters. Water Resources Research, 60(12), e2024WR037718.

Espinoza JC, Garreaud R, Poveda G, Arias PA., Molina-Carpio J, Masiokas M, Viale M and Scaff L (2020) Hydroclimate of the Andes Part I: Main Climatic Features. Front. Earth Sci. 8:64. doi: 10.3389/feart.2020.00064

Falco, M., Carril, A.F., Menéndez, C.G. et al. (2019) Assessment of CORDEX simulations over South America: added value on seasonal climatology and resolution considerations. Climate Dynamics, 52: 4771–4786. https://doi.org/10.1007/s00382-018-4412-z.

Falco M, Carril AF, Menéndez CG, Zaninelli PG, Li LZ (2018) Assessment of CORDEX simulations over South America: added value on seasonal climatology and resolution considerations. Clim Dyn 52, 4771–4786

Feddema, J. J., et al. (2005) The importance of land-cover change in simulating future climates. *Science*, 310(5754), 1674–1678.

Feijoó, M., Solman, S. (2022) Convection-permitting modeling strategies for simulating extreme rainfall events over Southeastern South America. Clim. Dyn. 59 (9), 2549–2569. https://doi.org/10.1007/s00382-022-06226-z.

Feng, Z., Leung, L. R., Hardin, J.,Terai, C. R., Song, F., & Caldwell, P. (2023) Mesoscale convective systems in DYAMOND global convection-permittingsimulations. Geophysical ResearchLetters, 50, e2022GL102603. https://doi.org/10.1029/2022GL102603

Feng, Z., Prein, A. F., Kukulies, J., Fiolleau, T., Jones, W. K., Maybee, B., et al. (2025) Mesoscale convective systems tracking method intercomparison (MCSMIP): Application to DYAMOND global km-scale simulations. Journal of Geophysical Research: Atmospheres, 130, e2024JD042204. https://doi.org/10.1029/2024JD042204

Feser, F., et al. (2011) Regional climate models add value to global model data: A review and selected examples. *Bulletin of the American Meteorological Society*, 92(9), 1181–1192.

Fischer, E. M., and Knutti, R. (2016) Observed heavy precipitation increase confirms theory and early models. *Nature Climate Change*, **6**, 986–991. https://doi.org/10.1038/nclimate3110

Fosser, G., Khodayar, S. & Berg, P. (2015) Benefit of convection permitting climate model simulations in the representation of convective precipitation. Clim Dyn 44, 45–60. https://doi.org/10.1007/s00382-014-2242-1

Fu, R., and W. Li (2004) Influence of land surface on transition from dry to wet season in Amazonia, *Theor. Appl. Climatol.*, **78**, 97–110, doi:10.1007/s00704-004-0046-7

Fu, R., Zhu, B., & Dickinson, R. E. (1999) How do atmosphere and land surface influence seasonal changes of convection in the tropical Amazon? Journal of Climate, 12(5), 1306-1321.

Funk, C., Peterson, P., Landsfeld, M. et al. (2015) The climate hazards infrared precipitation with stations—a new environmental record for monitoring extremes. Sci Data 2, 150066. https://doi.org/10.1038/sdata.2015.66

Gao, X., et al. (2006) Dynamical downscaling of the 21st-century climate projection for China using the MIT IGSM–RegCM system. *Journal of Climate*, 19(18), 3885–3907.

Gateño, F., Mendoza, P. A., Vásquez, N., Lagos-Zúñiga, M., Jiménez, H., Jerez, C., ... & Montserrat, S. (2024) Screening CMIP6 models for Chile based on past performance and code genealogy. Climatic Change, 177(6), 87.

Garreaud, R. D., et al. (2009) The South American monsoon. *Climate Dynamics*, 28(1), 3–33.

Garreaud, R. D., Vuille, M., & Clement, A. C. (2003) The climate of the Altiplano: Observed current conditions and mechanisms of past changes. *Palaeogeography, Palaeoclimatology, Palaeoecology*, 194(1-3), 5–22.

Garreaud, R. D., Vuille, M., Compagnucci, R., & Marengo, J. (2009) Present-day South American climate. Palaeogeography, Palaeoclimatology, Palaeoecology, 281(3-4), 180-195. doi: 10.1016/j.palaeo.2007.10.032

Giorgi, F. (2006) Regional climate modeling: Status and perspectives. *Journal de Physique IV*, 139, 101–118.

Giorgi, F., 2019 Thirty years of regional climate modeling: where are we and where are we going next? J. Geophys. Res. Atmos. 124, 5696–5723. https://doi.org/10.1029/ 2018JD030094.

Giorgi, F., Coppola, E., Giuliani, G., Ciarlo, J. M., Pichelli, E., Nogherotto, R., ... & Drofa, O. (2023) The fifth generation regional climate modeling system, RegCM5: Description and illustrative examples at parameterized convection and convection-permitting resolutions. Journal of Geophysical Research: Atmospheres, 128(6), e2022JD038199.

Giorgi, F., Coppola, E., Jacob, D., Teichmann, C., Abba Omar, S., Ashfaq, M., et al. (2022) The CORDEX-CORE EXP-I initiative: Description and highlight results from the initial analysis. Bulletin of the American Meteorological Society, 103(2), E293–E310. https://doi.org/10.1175/BAMS-D-21-0119.1

Giorgi, F., & Gutowski, W. J. (2015) Regional dynamical downscaling and the CORDEX initiative. *Annual Review of Environment and Resources*, 40, 467–490.

Giorgi, F., Jones, C., & Asrar, G. R. (2016) Addressing climate information needs at the regional level: the CORDEX framework. *Wiley Interdisciplinary Reviews: Climate Change*, 7(2), 211–229. https://doi.org/10.1002/wcc.380

Giorgi, F., & Mearns, L. O. (1991) Approaches to the simulation of regional climate change: A review. *Reviews of Geophysics*, 29(2), 191–216.

Giorgi, F., & Mearns, L. O. (1999) Introduction to special section: Regional climate modeling revisited. *Journal of Geophysical Research: Atmospheres*, 104(D6), 6335–6352.

Grimm, A. M., et al. (2000) ENSO and seasonal rainfall variability in South America. *Journal of Climate*, 13(1), 35–58.

Guilloteau, C., Foufoula-Georgiou, E. (2020) Multiscale Evaluation of Satellite Precipitation Products: Effective Resolution of IMERG. In: Levizzani, V., Kidd, C., Kirschbaum, D., Kummerow, C., Nakamura, K., Turk, F. (eds) Satellite Precipitation Measurement. Advances in Global Change Research, vol 69. Springer, Cham. https://doi.org/10.1007/978-3-030-35798-6_5

Gutiérrez, J. M., et al. (2019) An intercomparison of a large ensemble of statistical downscaling methods over Europe: Results from the VALUE initiative. *International Journal of Climatology*, 39(9), 3750–3785.

Gutowski, W. J., et al. (2010) Regional climate modeling: The regional climate modeling system (RCMS). *Annual Review of Environment and Resources*, 35, 253–279.

Haarsma, R. J., et al. (2016) High Resolution Model Intercomparison Project (HighResMIP) for CMIP6. *Geoscientific Model Development*, 9(11), 4185–4208.

Hall, A., Rahimi, S., Norris, J., Ban, N., Siler, N., Leung, L. R., et al. (2024) An evaluation of dynamical downscaling methods used to project regional climate change. Journal of Geophysical Research: Atmospheres, 129, e2023JD040591. https://doi.org/10.1029/2023JD040591

Halladay, K., Kahana, R., Johnson, B., et al. (2023) Convection-permitting climate simulations for South America with the Met Office Unified Model. Clim. Dyn. 61, 5247–5269. https://doi.org/10.1007/s00382-023-06853-0.

Haywood, J. M., & Boucher, O. (2000) Estimates of the direct and indirect radiative forcing due to tropospheric aerosols: A review. *Reviews of Geophysics*, 38(4), 513–543.

Han, B., Fan, J., Varble, A., Morrison, H., Williams, C. R., Chen, B., et al. (2019) Cloud-resolving model intercomparison of an MC3E squall line case: Part II. Stratiform precipitation properties. Journal of Geophysical Research: Atmospheres, 124(2), 1090–1117. https://doi.org/10.1029/2018JD029596

He, C., Kumar, R., Tang, W., Pfister, G., Xu, Y., Qian, Y., & Brasseur, G. (2024) Air pollution interactions with weather and climate extremes: current knowledge, gaps, and future directions. Current Pollution Reports, 10(3), 430-442.

He, C., Valayamkunnath, P., Barlage, M., Chen, F., Gochis, D., Cabell, R., ... & Ek, M. (2023) The community Noah-MP land surface modeling system technical description version 5.0. NCAR Technical Note NCAR/TN-575+ STR, 5.

Heim, C., Leutwyler, D., & Schär, C. (2023) Application of the pseudo-global warming approach in a kilometer-resolution climate simulation of the tropics. Journal of Geophysical Research: Atmospheres, 128(5), 1–24. https://doi.org/10.1029/2022JD037958

Herdies, D. L., A. da Silva, M. A. F. Silva Dias, and R. Nieto Ferreira (2002) Moisture budget of the bimodal pattern of the summer circulation over South America. J. Geophys. Res., 107, 8075, doi:10.1029/2001JD000997

Hernández, K. S., Henao, J. J., Gómez-Ríos, S., Robledo, V., Rendón, A. M., & Mejía, J. F. (2025) Spatio-temporal representation of mesoscale convective systems in convection-permitting simulations over Northwestern South America: Insights into rainfall overestimation. Journal of Geophysical Research: Atmospheres, 130(7), e2024JD042289. https://doi.org/10.1029/2024JD042289

Hernandez D, Mendoza PA, Boisier JP, Ricchetti F. (2022) Hydrologic Sensitivities and ENSO Variability Across Hydrological Regimes in Central Chile (28°–41°S). Water Resources Research 58 (9) DOI: 10.1029/2021WR031860

Hewitson, B. C., & Crane, R. G. (2006) Consensus between GCM climate change projections with empirical downscaling: Precipitation downscaling over South Africa. *International Journal of Climatology*, 26(10), 1315–1337.

Hernández, K. S., Henao, J. J., Gómez-Ríos, S., Robledo, V., Rendón, A. M., & Mejía, J. F. (2025) Spatio-temporal representation of mesoscale convective systems in convection-permitting simulations over Northwestern South America: Insights into rainfall overestimation. Journal of Geophysical Research: Atmospheres, 130(7), e2024JD042289. https://doi.org/10.1029/2024JD042289

Hersbach, H., Co-authors (2020) The ERA5 global reanalysis. Q. J. R. Meteorol. Soc. 146, 1999–2049. https://doi.org/10.1002/qj.3803.

Hewitson, B. C., et al. (2014) Regional climate projections. In: *Climate Change 2014: Impacts, Adaptation, and Vulnerability*. IPCC WGII AR5.

Hong, S.-Y., Noh, Y., Dudhia, J. (2006) A new vertical diffusion package with an explicit treatment of entrainment processes. Mon. Weather Rev. 134 (9), 2318–2341. https://doi.org/10.1175/MWR3199.1.

Huang, Y., Xue, M., Hu, X., Matin, E., Novoa, H., McPherson, R., Liu, C., Chen, M., Hong, Y., Perez, A.V., Morales, I., Ticona, J.L., Flores, A.J. (2024a) Increasing frequency and precipitation intensity of convective storms in the Peruvian Central Andes: Projections from convection-permitting regional climate simulations. Quarterly Journal of the Royal Meteorological Society 1–20. https://doi.org/ 10.1002/qj.4820.

Huang, Y., Xue, M., Hu, X., Matin, E., Novoa, H., McPherson, R., Liu, C., Ikeda, K., Rasmussen, R., Prein, A.F., Perez, A.V., Morales, I., Ticona, J.L., Flores, A.J. (2024b) Characteristics of Precipitation and Mesoscale Convective Systems over the Peruvian Central Andes in Multi 5-Year Convection-Permitting Simulations. Journal of Geophysical Research: Atmospheres 129. https://doi.org/10.1029/2023JD040394 e2023JD040394.

Huang, Y., Xue, M., Hu, X., Matin, E., Novoa, H., McPherson, R., Perez, A., Morales, I. (2023) Convection-Permitting Simulations of Precipitation over the Peruvian Central Andes: Strong Sensitivity to Planetary Boundary Layer Parameterization. Journal of Hydrometeorology 24, 1969–1990. https://doi.org/10.1175/JHM-D-22-0173.1.

Huffman, G.J., Bolvin, D.T., Braithwaite, D., Hsu, K., Joyce, R., Kidd, C., Nelkin, E.J., Sorooshian, S., Tan, J., Xie, P. (2019) Algorithm Theoretical Basis Document (ATBD) Version 5.2 for the NASA Global Precipitation Measurement (GPM)

Integrated MultisatellitE Retrievals for GPM (I-MERG). GPM. Project 38. https://pmm.nasa.gov/sites/default/files/document_files/IMERG_ATBD_V6.pdf.

Humphrey, V., Gudmundsson, L. & Seneviratne, S.I. (2016) Assessing Global Water Storage Variability from GRACE: Trends, Seasonal Cycle, Subseasonal Anomalies and Extremes. Surv Geophys 37, 357–395. https://doi.org/10.1007/s10712-016-9367-1

Iacono, M.J., Delamere, J.S., Mlawer, E.J., Shephard, M.W., Clough, S.A., Collins, W.D. (2008) Radiative forcing by long-lived greenhouse gases: calculations with the AER radiative transfer models. J. Geophys. Res. 113, D13103. https://doi.org/10.1029/ 2008JD009944.

IPCC (2021) *Intergovernmental Panel on Climate Change, Sixth Assessment Report (AR6), Working Group I: The Physical Science Basis.* https://www.ipcc.ch/report/ar6/wg1/

Jimenez, Pedro A., Jimy Dudhia, J. Fidel Gonzalez–Rouco, Jorge Navarro, Juan P. Montavez, and Elena Garcia–Bustamante (2012) A revised scheme for the WRF surface layer formulation. Mon. Wea. Rev., 140, 898–918. doi:10.1175/MWR-D-11-00056.1

Kawase, H., et al. (2009) Diurnal cycle of precipitation over the maritime continent in a high-resolution atmospheric general circulation model. *Journal of Climate*, 22(22), 5670–5676.

Kendon, E.J., Roberts, N.M., Fowler, H.J., Roberts, M.J., Chan, S.C., Senior, C.A. (2014) Heavier summer downpours with climate change revealed by weather forecast resolution model. Nat. Clim. Chang. 4, 570–576. https://doi.org/10.1038/ nclimate2258.

Kendon, E. J., Roberts, N. M., Fowler, H. J., Roberts, M. J., Chan, S. C., & Senior, C. A. (2017) Do convection-permitting regional climate models improve projections of future precipitation change? *Bulletin of the American Meteorological Society*, 98(1), 79–93. https://doi.org/10.1175/BAMS-D-15-0004.1

Kendon, E.J., Roberts, N.M., Senior, C.A., Roberts, M.J. (2012) Realism of rainfall in a very high-resolution regional climate model. J. Clim. 25, 5791–5806. https://doi. org/10.1175/JCLI-D-11-00562.1

Kim, J.-H., J. Dudhia, C.-H. Liu, K. Ikeda, R. Rasmussen, T. Schneider (2025) Finding missing clouds in the CONUS404 using satellite derived cloud radiative properties. Atmospheric Research, in review.

Kodama, Y. M. (1992) Large-scale common features of subtropical precipitation zones (the Baiu frontal zone, the SPCZ, and the SACZ). Part-I: Characteristics of subtropical frontal zones. J. Meteor. Soc. Japan, 70, 813–835.

Kodama, Y.-M. (1993) Large-scale common features of subtropical precipitation zone (the Baiu frontal zone, the SPCZ and the SACZ) Part 2: Conditions of the circulations for generating the STCZs. J. Meteor. Soc. Japan, 71, 581-610.

Koren, I., Kaufman, Y. J., Rosenfeld, D., Remer, L. A., & Rudich, Y. (2004) Aerosol invigoration and restructuring of Atlantic convective clouds. *Geophysical Research Letters*, 31(5).

Kumjian, M. R., and Coauthors (2020) Gargantuan hail in Argentina. Bull. Amer. Meteor. Soc., 101, E1241–E1258, https://doi.org/10.1175/BAMS-D-19-0012.1.

Jones, R. G., et al. (1995) A high resolution atmospheric GCM with enhanced hydrology: Evaluation and application to climate change. *Climate Dynamics*, 11(2), 61–79.

Lagos Zúñiga, M. Á. (2024) Convective precipitation in the subtropical Andes of Central Chile: physical mechanisms and climate change projections. PhD Thesis. Universidad de Chile. https://repositorio.uchile.cl/handle/2250/203019

Lagos-Zuniga, M., Balmaceda-Huarte, R., Regoto, P., Torrez, L., Olmo, M., Lyra, A., ... & Bettolli, M. L. (2024) Extreme indices of temperature and precipitation in South America: Trends and intercomparison of regional climate models. Climate Dynamics, 62(6), 4541-4562.

Laprise, R. (2008) Regional climate modelling. *Journal of Computational Physics*, 227(7), 3641–3666.

Lavers, D.A., Simmons, A., Vamborg, F. & Rodwell, M.J. (2022) An evaluation of ERA5 precipitation for climate monitoring. Quarterly Journal of the Royal Meteorological Society, 148(748) 3124–3137. Available from: https://doi.org/10.1002/qj.4351

Lawrence, D., & Vandecar, K. (2015) Effects of tropical deforestation on climate and agriculture. *Nature Climate Change*, 5(1), 27–36.

Leung, L. R., Boos, W. R., Catto, J. L., A. DeMott, C., Martin, G. M., Neelin, J. D., O'Brien, T. A., Xie, S., Feng, Z., Klingaman, N. P., Kuo, Y., Lee, R. W., Martinez-Villalobos, C., Vishnu, S., Priestley, M. D. K., Tao, C., and Zhou, Y. (2022) Exploratory Precipitation Metrics: Spatiotemporal Characteristics, Process-Oriented, and Phenomena-Based, J. Climate, 35, 3659–3686, https://doi.org/10.1175/JCLI-D-21-0590.1

Li, W., and R. Fu (2004) Transition of the large-scale atmospheric and land surface conditions from dry to wet season over Amazonia as diagnosed by the ECMWF Re-analysis, *J. Clim.*, **17**, 2637–2651.

Li, W., Fu, R., & Dickinson, R. E. (2006) Rainfall and its seasonality over the Amazon in the 21st century as assessed by the coupled models for the IPCC AR4. *Journal of Geophysical Research: Atmospheres*, 111(D2).

Lima, A. L., Veiga, J. A. P., Brito, A. L., & Correia, F. W. S. (2023) Effects of deforestation at different spatial scales on the climate of the Amazon basin. Climate Research, 91, 21-46. https://doi.org/10.3354/cr01717

Tzu-Shun Lin, Cenlin He, Changhai Liu, Ronnie Abolafia-Rosenzweig, Zhe Zhang, Jimy Dudhia, Michael Barlage, and Andrew Newman (2025) Effect of Soil Organic Matter on WRF/Noah-MP Simulated Surface Air Temperature. Joint MPAS/WRF Users Workshop 2025, CO, USA. https://drive.google.com/file/d/1g7LVEvDcxL-RUOyCrVdsVlEtRZZ86VOe/view

Liu, C.-H., Dudhia, J., Wang, W., Moncrieff, M.W. (2021) Tropical Convection Simulation in the Grey Zone: Impact of Horizontal Resolution and Convective Parameterization. AGU, New Orleans, 13–17 December 2021.

Liu, C.; Ikeda, K.; Rasmussen, R. (2024) Severe Convective Weather in the Central and Eastern United States: Present and Future. *Atmosphere*, 15,1444. https:// doi.org/10.3390/atmos15121444

Liu, C., K. Ikeda, A. Prein, L. Scaff, F. Dominguez, R. Rasmussen et al. (2025) Convection-permitting climate simulations over South America: Experimentation during different phases of ENSO. *Atmos. Res.*, 316, https://doi.org/10.1016/j.atmosres.2025.107936

Liu, C.H., Ikeda, K., Rasmussen, R., Barlage, M., Newman, A.J., Prein, A.F., et al. (2017) Continental-scale convection-permitting modeling of the current and future climate of North America. Clim. Dyn. 49 (1–2), 71–95. https://doi.org/10.1007/s00382- 016

Llopart, M., Domingues, L.M., Torma, C. et al. (2021) Assessing changes in the atmospheric water budget as drivers for precipitation change over two CORDEX-CORE domains. Clim Dyn 57, 1615–1628. https://doi.org/10.1007/s00382-020-05539-1

Lucas-Picher, P., Argüeso, D., Brisson, E., Tramblay, Y., Berg, P., Lemonsu, A., Kotlarski, S., & Caillaud, C. (2021) Convection-permitting modeling with regional climate models: Latest developments and next steps. Wiley Interdisciplinary Reviews: Climate Change, 12(6), e731. https://doi.org/10.1002/wcc.731

Maraun, D., et al. (2010) Precipitation downscaling under climate change: Recent developments to bridge the gap between dynamical models and the end user. *Reviews of Geophysics*, 48(3).

Marengo, J.A. and Camargo, C.C. (2008) Surface air temperature trends in Southern Brazil for 1960–2002. Int. J. Climatol., 28: 893-904. https://doi.org/10.1002/joc.1584.

Marengo, J.A., Jones, R., Alves, L.M. and Valverde, M.C. (2009) Future change of temperature and precipitation extremes in South America as derived from the PRECIS regional climate modeling system. Int. J. Climatol., 29: 2241-2255. https://doi.org/10.1002/joc.1863.

Marengo, J. A., et al. (2012) Recent developments on the South American monsoon system. *International Journal of Climatology*, 32(1), 1–21.

Marengo, J. A., et al. (2018) Changes in climate and land use over South America. *WIREs Climate Change*, 9(6), e511.

Marengo, J. A., W. R. Soares, C. Saulo, and M. Nicolini (2004) Climatology of the low-level jet east of the Andes as derived from the NCEP–NCAR reanalyses: Characteristics and temporal variability. J. Climate, 17, 2261–2280, https://doi.org/10.1175/1520-0442(2004)017<2261:COTLJE>2.0.CO;2.

Martinez J.A., Junquas C., Bozkurt D., Viale M., Fita L., Trachte K., Campozano L., Arias P.A., Boisier J.P., Condom T., Goubanova K., Pabón-Caicedo J.D., Poveda G., Solman S.A., Sörensson A.A. and Espinoza J.C. (2024) Recent progress in atmospheric modeling over the Andes – part I: review of atmospheric processes. Front. Earth Sci. 12:1427783. doi: 10.3389/feart.2024.1427783

Martinez-Villalobos, C., Neelin, J.D. (2023) Regionally high risk increase for precipitation extreme events under global warming. Sci Rep 13, 5579. https://doi.org/10.1038/s41598-023-32372-3

Martins, J. V., et al. (2009) Remote sensing of smoke aerosol and its radiative effects in the Amazon. *Journal of Geophysical Research*, 114(D14).

Masiokas, M. H., Villalba, R., Luckman, B. H., Le Quesne, C., & Aravena, J. C. (2006) Snowpack variations in the central Andes of Argentina and Chile, 1951–2005: Large-scale atmospheric influences and implications for water resources in the region. Journal of climate, 19(24), 6334-6352. DOI: 10.1175/JCLI3969.1

Mendoza, P. A., Clark, M. P., Mizukami, N., Newman, A. J., Barlage, M., Gutmann, E. D., ... & Arnold, J. R. (2015a) Effects of hydrologic model choice and calibration on the portrayal of climate change impacts. Journal of Hydrometeorology, 16(2), 762-780.

Mendoza, P. A., Clark, M. P., Barlage, M., Rajagopalan, B., Samaniego, L., Abramowitz, G., & Gupta, H. (2015b) Are we unnecessarily constraining the agility of complex process-based models? Water Resources Research, 51(1), 716-728.

Mendoza, P. A., Mizukami, N., Ikeda, K., Clark, M. P., Gutmann, E. D., Arnold, J. R., ... & Rajagopalan, B. (2016) Effects of different regional climate model resolution and forcing scales on projected hydrologic changes. Journal of Hydrology, 541, 1003-1019.

Mendoza PA, Rajagopalan B, Clark MP, Cortés G, McPhee J. (2014) A robust multimodel framework for ensemble seasonal hydroclimatic forecasts. Water Resources Research 50 (7): 6030–6052 DOI: 10.1002/2014WR015426

Miguez-Macho, G., Fan, Y., Weaver, C.P., Walko, R., Robock, A. (2007) Incorporating water table dynamics in climate modeling: 2. Formulation, validation, and soil moisture simulation. J. Geophys. Res. 112, D13108. https://doi.org/10.1029/ 2006JD008112.

Moraes-Arraut, J., Nobre, C., Barbosa, H. M. J., Obregon, G., & Marengo, J. (2012) Aerial rivers and lakes: Looking at large-scale moisture transport and its relation to amazonia and to subtropical rainfall in south america. Journal of Climate, 25 (2), 543 - 556.

Morrison, H., van Lier-Walqui, M., Fridlind, A. M., Grabowski, W. W., Harrington, J. Y., Hoose, C., et al. (2020) Confronting the challenge of modeling cloud and precipitation microphysics. Journal of Advances in Modeling Earth Systems, 12, e2019MS001689. https://doi.org/10.1029/2019MS001689

Mu, Y., Jones, C., Carvalho, L. M. V., Kukulies, J., Prein, A. F., Xue, L., & Liu,C. (2025) Impacts of northerly low-leveljets on mesoscale convective systems eastof the Andes. Journal of Geophysical Research: Atmospheres, 130, e2025JD043842. https://doi.org/10.1029/2025JD043842

Müller, O. V., E. H. Berbery, D. Alcaraz-Segura, and M. B. Ek (2014) Regional model simulations of the 2008 drought in southern South America using a consistent set of land surface properties. J. Climate, 27, 6754–6778, doi:10.1175/JCLI-D-13-00463.1.

Müller, O. V., McGuire, P. C., Vidale, P. L., and Hawkins, E. (2024) River flow in the near future: a global perspective in the context of a high-emission climate change scenario, Hydrol. Earth Syst. Sci., 28, 2179–2201, https://doi.org/10.5194/hess-28-2179-2024

Müller, O. V., Vidale, P. L., Vannière, B., Schiemann, R., and McGuire, P. C. (2021) Does the HadGEM3-GC3.1 GCM overestimate land precipitation at high resolution? A constraint based on observed river discharge. *Journal of Hydrometeorology*, 22, 2131–2151, https://doi.org/10.1175/JHM-D-20-0290.1

Niu, G.Y., et al. (2011) The community Noah land surface model with multiparameterization options (Noah-MP): 1. Model description and evaluation with local-scale measurements. J. Geophys. Res. 116, D12109. https://doi.org/10.1029/ 2010JD015139.

Nobre, C. A., et al. (2009) Amazon deforestation and climate change. *Geophysical Research Letters*, 36(7).

O'Gorman, P. A., and Schneider, T. (2009) The physical basis for increases in precipitation extremes in simulations of 21st-century climate change. *Proceedings of the National Academy of Sciences*, **106**(35), 14773–14777.

Palomino-Angel S.Anaya-Acevedo J. A.Botero B. A. (2019) Evaluation of 3B42V7 and IMERG daily-precipitation products for a very high-precipitation region in northwestern South America.Atmos. Res.21737–48. 10.1016/j.atmosres.2018.10.012

Pielke, R. A., et al. (2007) An overview of regional land-use and land-cover impacts on rainfall. *Tellus B: Chemical and Physical Meteorology*, 59(3), 587–601.

Pitman, A. J., et al. (2009) The impact of land cover change on climate. *Nature Geoscience*, 2(11), 681–685.

Portele, T.C., Laux, P., Lorenz, C., Janner, A., Horna, N., Fersch, B., Iza, M., Kunstmann, H. (2021) Ensemble-tailored pattern analysis of high-resolution dynamically downscaled precipitation fields: example for climate sensitive regions of South America. Front. Earth Sci. 9, 669427. https://doi.org/10.3389/ feart.2021.669427

Potter, E., (2023) An Evaluation of High-Resolution Model Simulations of Orographic Precipitation, Snowpack, Atmospheric Rivers, and Their Climate Sensitivities in the Southern Andes. *Legacy Theses & Dissertations (2009-2024)*. 3222. https://doi.org/10.54014/74VY-VP3Y

Poveda, G., and O. J. Mesa (1999) The westerly low-level Choco Jet and two other atmospheric jets over Colombia: Climatology and variability during ENSO phases. (in Spanish). Rev. Acad. Colomb. Cienc., 23, 517–528.

Poveda, G., and Oscar J. Mesa (2000) On the existence of Lloró (the rainiest locality on Earth): Enhanced ocean–land–atmosphere interaction by a low-level jet. Geophys. Res. Lett., 27, 1675–1678, https://doi.org/10.1029/1999GL006091.

Poveda, G., and Coauthors (2005) The Diurnal Cycle of Precipitation in the Tropical Andes of Colombia. Mon. Wea. Rev., 133, 228–240, https://doi.org/10.1175/MWR-2853.1.

Poveda, G., P.R. Waylen, & R. Pulwarty (2006) Modern climate variability in northern South America and southern Mesoamerica. Palaeogeography, Palaeoclimatology, & Palaeoecology, 234, 3-27.

Poveda, G., Jaramillo, L., and Vallejo, L. F. (2014) Seasonal precipitation patterns along pathways of South American low-level jets and aerial rivers. Water Resources Research, 50 (1), 98-118. doi: https://doi.org/10.1002/2013WR0140871095.

Poveda, G., J.C. Espinoza, M.D. Zuluaga, S.A. Solman, R. Garreaud, and P.J. van Oevelen (2020) High impact weather events in the Andes. Frontiers in Earth Science, Section Hydrosphere, 8:162. doi: 10.3389/feart.2020.00162.

Poveda, G. (2023) Mechanisms controlling the 4D distribution of rainfall and latent heating over the rainiest region on Earth. Journal of Geophysical Research: Atmospheres, 128, e2023JD039328. https://doi.org/10.1029/2023JD039328

Prein, et al. (2024) Km-scale simulations of mesoscale convective systems over South America – a feature tracker intercomparison. *J. Geophys. Res*. 129. https://doi.org/ 10.1029/2023JD040254

Prein, A. F., et al. (2015) A review on regional convection-permitting climate modeling: Demonstrations, prospects, and challenges. *Reviews of Geophysics*, 53(2), 323–361.

Prein, A. F., G. J. Holland, R. M. Rasmussen, J. Done, K. Ikeda, M. P. Clark, and C.-H. Liu (2013) Importance of regional climate model grid spacing for the simulation of heavy precipitation in the Colorado Headwaters. *J. Climate*, 26, 4848-4857.

Prein, A.F., Liu, C., Ikeda, K. et al. (2020) Simulating North American mesoscale convective systems with a convection-permitting climate model. Clim Dyn 55, 95–110. https://doi.org/10.1007/s00382-017-3993-2

Prein, A. F., R. M. Rasmussen, K. Ikeda, C.-H. Liu, M. P. Clark, and G. J. Holland (2017) The future intensification of hourly precipitation extremes. *Nat. Clim. Change*, DOI: 10.1038/NCLIMATE3168.

Qin, Y., Wang, D., Ziegler, A. D., Fu, B., & Zeng, Z. (2025) Impact of Amazonian deforestation on precipitation reverses between seasons. Nature, 639, 102-108. https://doi.org/10.1038/s41586-024-08570-y

Rasmussen, R.M., Chen, F., Liu, C.H., Ikeda, K., Prein, A., Kim, J., Schneider, T., Dai, A., Gochis, D., Dugger, A., Zhang, Y., Jaye, A., Dudhia, J., He, C., Harrold, M., Xue, L., Chen, S., Newman, A., Dougherty, E., Abolafia-Rosenzweig, R., Lybarger, N.D., Viger, R., Lesmes, D., Skalak, K., Brakebill, J., Cline, D., Dunne, K., Rasmussen, K., Miguez-Macho, G.

(2023) CONUS404: The NCAR–USGS 4-km Long-Term Regional Hydroclimate Reanalysis over the CONUS. Bulletin of the American Meteorological Society 104 (8), E1382–E1408. https://doi.org/10.1175/BAMS-D-21-0326.1.

Rasmussen, R., Ikeda, K., Liu, C.H., Gochis, D., Clark, M., Dai, A.G., et al. (2014) Climate change impacts on the water balance of the Colorado headwaters: high-resolution regional climate model simulations. J. Hydrometeorol. 15 (3), 1091–1116. https:// doi.org/10.1175/Jhm-D-13-0118.1.

Rasmussen, R., Liu, C.H., Ikeda, K., Gochis, D., Yates, D., Chen, F., et al. (2011) High resolution coupled climate runoff simulations of seasonal snowfall over Colorado: a process study of current and warmer climate. J. Clim. 24 (12), 3015–3048. https:// doi.org/10.1175/2010

Rau, P., Bourrel, L., Labat, D., Melo, P., Dewitte, B., Frappart, F., Lavado, W. & Felipe, O. (2017) Regionalization of rainfall over the Peruvian Pacific slope and coast. International Journal of Climatology, 37(1), 143-158. https://doi.org/10.1002/joc.4693

Reboita MS, Ambrizzi T, Crespo NM, Dutra LMM, Ferreira GWS, Rehbein A, Drumond A, da Rocha RP, Souza CA. (2021) Impacts of teleconnection patterns on South America climate. Ann N Y Acad Sci. 2021 Nov;1504(1):116-153. doi: 10.1111/nyas.14592. Epub 2021 Apr 29. PMID: 33914367.

Reboita, M. S., Drumond, A., Ferreira, G., Zilli, M., Crespo, N., Rodrigues, R., da Rocha, R., Ambrizzi, T. (2025) Meteorology and Climate of South America and Surrounding Oceans. In: Taschetto, A. S., Ndarana, T., Ambrizzi, T. eds. Meteorology and Climate of the Southern Hemisphere. Cambridge.

Reboita, M. S., Kuki, C. A. C., Marrafon, V. H., de Souza, C. A., Ferreira, G. W. S., Teodoro, T., & Lima, J. W. M. (2022) South America climate change revealed through climate indices projected by GCMs and Eta-RCM ensembles. Climate Dynamics, 58(1), 459-485.

Rehbein, A., Prein, A.F., Ambrizzi, T. *et al.* (2025) 20 Years of MCSs simulations over South America using a convection-permitting model. *Clim Dyn* **63**, 38. https://doi.org/10.1007/s00382-024-07529-z

Reichler, T., & Kim, J. (2008) How well do coupled models simulate today's climate? *Bulletin of the American Meteorological Society*, 89(3), 303–311.

Rojas, Y., & Minder, J. R. (2024) Variability of the Southern Andes rain shadow. Atmospheric Research, 308, 107509.

Ropelewski, C. F., & Halpert, M. S. (1987) Global and regional scale precipitation patterns associated with the El Niño/Southern Oscillation. *Monthly Weather Review*, 115(8), 1606–1626.

Rosenfeld, D., Lohmann, U., Raga, G. B., et al. (2008) Flood or drought: How do aerosols affect precipitation? *Science*, 321(5894), 1309–1313.

Rosero, E., Yang, Z. L., Wagener, T., Gulden, L. E., Yatheendradas, S., & Niu, G. Y. (2010) Quantifying parameter sensitivity, interaction, and transferability in hydrologically enhanced versions of the Noah land surface model over transition zones during the warm season. Journal of Geophysical Research: Atmospheres, 115(D3).

Ruiz-Vásquez, M., Arias, P.A. & Martínez, J.A. (2024) Enso influence on water vapor transport and thermodynamics over Northwestern South America. Theor Appl Climatol 155, 3771–3789. https://doi.org/10.1007/s00704-024-04848-3

Rummukainen, M. (2010) State-of-the-art with regional climate models. *Climate Change*, 1(1), 82–96.

Salati, E., & Vose, P. B. (1984) Amazon Basin: A system in equilibrium. *Science*, 225(4658), 129–138.

Saavedra, F. A., Kampf, S. K., Fassnacht, S. R., & Sibold, J. S. (2018) Changes in Andes snow cover from MODIS data, 2000–2016. The Cryosphere, 12(3), 1027-1046.

Sakaguchi, K., Leung, L. R., Burleyson, C. D., Xiao, H., & Wan, H. (2018) Role of troposphere-convection-land coupling in the southwestern Amazon precipitation bias of the community earth system model version 1 (CESM1). Journal of Geophysical Research: Atmospheres, 123, 8374–8399. https://doi.org/10.1029/2018JD028999

Salio, P., M. Nicolini, and A. C. Saulo, (2002) Chaco low-level jet events characterization during the austral summer season, J. Geophys. Res., 107(D24), 4816, doi:10.1029/2001JD001315.

Salio, P., Nicolini, M. and Zipser, E.J. (2007) Mesoscale convective systems over southeastern South America and their relationship with the South American low-level jet. Monthly Weather Review, 135, 1290–1309. https://doi.org/10.1175/MWR3305.1.

Schär, C., et al. (1996) The use of a regional climate model for simulations over complex terrain. *Climate Dynamics*, 12(7), 417–432.

Schär, C., Co-authors (2020) Kilometer-scale climate models: prospects and challenges. Bull. Am. Meteorol. Soc. 101, 567–587. https://doi.org/10.1175/BAMS-D-18-01

Segovia, S., Mendoza, P. A., Lagos-Zúñiga, M., Scaff, L., & Prein, A. (2025) Benchmarking convection-permitting climate simulations for hydrological applications: A comparative study of WRF-SAAG and observation-based products. EGUsphere, 2025, 1-33.

Senior CA, Marsham JH, Berthou S, Burgin LE, Folwell SS, Kendon EJ, Klein CM, Jones RG, Mittal N, Rowell DP, Tomassini L, Vischel T, Becker B, Birch CE, Crook J, Dougill AJ, Finney DL, Graham RJ, Hart NCG et al (2021) Convection permitting regional climate change simulations for understanding future climate and informing decision making in Africa. Bull Am Meteorol Soc. https://doi.org/10.1175/BAMS-D-20-0020.1

Sepúlveda, U. M., Mendoza, P. A., Mizukami, N., & Newman, A. J. (2022) Revisiting parameter sensitivities in the variable infiltration capacity model across a hydroclimatic gradient. Hydrology and Earth System Sciences, 26(13), 3419-3445.

Sierra, J.P., J.-C. Espinoza, C. Junquas, S. Wongchuig, J. Polcher, V. Moron, L. Fita, P.A. Arias, A. Schrapffer, R. Pennel (2023) Impacts of land-surface heterogeneities and Amazonian deforestation on the wet season onset in southern Amazon. Clim. Dynam., 61, 4867-4898, 10.1007/s00382-023-06835-2

Skamarock, W., Klemp, J., Dudhia, J., Gill, D.O., Liu, Z., Berner, J., Wang, W., Powers, J. G., Duda, M.G., Barker, D., Huang, X.-Y. (2019) A Description of the Advanced Research WRF Model Version 4.1. NCAR Tech. Note NCAR/TN-556+STR, 145. https://doi.org/10.5065/1dfh-6p97.

Solman, S. A., et al. (2008) Evaluation of regional climate model simulations over South America. *Climate Dynamics*, 30(7), 733–752.

Solman, S. A., et al. (2013) Evaluation of an ensemble of regional climate model simulations over South America driven by ERA-Interim. *Climate Dynamics*, 41(5–6), 1139–1157.

Solman, S. A., Camilloni, I., & Cardoso, M. F. (2013) Regional climate change scenarios for South America from the CLARIS-LPB project: model performance and future projections. *Climate Dynamics*, 40(9-10), 2557–2579. https://doi.org/10.1007/s00382-012-1421-1

Spracklen, D. V., Arnold, S. R., & Taylor, C. M. (2012) Observations of increased tropical rainfall preceded by air passage over forests. *Nature*, 489(7415), 282–285.

Stratton, R.A., Senior, C.A., Vosper, S.B., Folwell, S.S., Boutle, I.A., Earnshaw, P.D., et al. (2018) A Pan-African convection-permitting regional climate simulation with the met office unified model: CP4-Africa. J. Clim. 31 (9), 3485–3508. https://doi.org/ 10.1175/jcli-d-17-0503.1

Thompson, G., Field, P.R., Rasmussen, R.M., Hall, W.D. (2008) Explicit forecasts of winter precipitation using an improved bulk microphysics scheme. Part II: implementation of a new snow parameterization. Mon. Weather Rev. 136, 5095–5115. https://doi.org/10.1175/2008MWR2387.1.

Tovar, C., A.F. Carril, A.G. Gutiérrez, A. Ahrends, L. Fita, P. Zaninelli, P. Flombaum, A.M. Abarzúa, D. Alarcón, V. Aschero, S. Báez, A. Barros, J. Carilla, M.E. Ferrero, S.G. Flantua, P. Gonzáles, C.G. Menéndez, O.A. Pérez-Escobar, A. Pauchard, R.C. Ruscica, T. Särkinen, A.A. Sörensson, A. Srur, R. Villalba, P.M. Hollingsworth (2022) Understanding climate change impacts on biome and plant distributions in the Andes: challenges and opportunities. J. Biogeogr., 49, pp. 1420-1442, 10.1111/jbi.14389

Trenberth, K. E. (2011) Changes in precipitation with climate change. *Climate Research*, **47**, 123–138. https://doi.org/10.3354/cr00953

Trenberth, K. E., Dai, A., Rasmussen, R. M., and Parsons, D. B. (2003) The changing character of precipitation. *Bulletin of the American Meteorological Society*, **84**(9), 1205–1217.

Twomey, S. (1977) The influence of pollution on the shortwave albedo of clouds. *Journal of the Atmospheric Sciences*, 34(7), 1149–1152.

Vallejo-Bernal, S.M., V. Urrea, J. M. Bedoya-Soto, D. Posada, A. Olarte, Y. Cárdenas-Posso, F. Ruiz-Murcia, M.T. Martínez, W.A. Petersen, G.J. Huffman, and G. Poveda (2020) Ground Validation of TRMM 3B43 Precipitation Data over Colombia. Part I: Monthly and Seasonal Timescales. International Journal of Climatology, 2020, 1-24. https://doi.org/10.1002/joc.6640.

Varble, A. C., Morrison, H., & Zipser, E. (2020) Effects of under-resolved convective dynamics on the evolution of a squall line. Monthly Weather Review, 148(1), 289–311. https://doi.org/10.1175/mwr-d-19-0187.1

Vásquez, N. A., Mendoza, P. A., Knoben, W. J., Arnal, L., Lagos-Zúñiga, M., Clark, M., & Vargas, X. (2024) The Key role of temporal stratification for GCM bias correction in climate impact assessments. Earth's Future, 12(8), e2023EF004242.

Vásquez, N. A., Mendoza, P. A., Lagos-Zuñiga, M., Scaff, L., Muñoz-Castro, E., & Vargas, X. (2024) Robust spatial changes in climate classes: insights from bias-corrected CMIP6 models across Chile. Environmental Research Letters, 20(1), 014061.

Velasco, I., & Fritsch, J. M. (1987) Mesoscale convective com-plexes in the Americas. Journal of Geophysical Research, 92(D8), 9591–9613. https://doi.org/10.1029/JD092iD08p09591

Vera, C., et al. (2006) The South American monsoon system: Recent evolution and current understanding. *Journal of Climate*, 19(8), 5031–5049.

Vera, C., Rauber, R. M., & Liebmann, B. (2013) Regional climate modeling and climate change impact assessment in South America: The CREAS project. *Atmosfera*, 26(3), 237–255. https://doi.org/10.20937/ATM.2013.26.03.04

Vergara-Temprado, J., et al. (2021) Convection-permitting simulations of South American climate: Challenges and opportunities. *Climate Dynamics*, 56(11–12), 3507–3527.

Viale, M., Bianchi, E., Cara, L., Ruiz, L. E., Villalba, R., Pitte, P., ... & Zalazar, L. (2019) Contrasting climates at both sides of the Andes in Argentina and Chile. Frontiers in Environmental Science, 7, 69.

Wang, H., & Fu, R. (2004) Influence of cross-Andes flow on the South American low-level jet. Journal of climate, 17(6), 1247-1262.

Wang, Y.-G., Geerts, B., Liu, C.-H. (2018) A 30-year convection-permitting regional climate simulation over the interior western United States. Part I: validation. Int. J. Climatol. 38 (1–2). https://doi.org/10.1002/joc.5527

Wang, Y.-G., Geerts, B., Liu, C.-H., X.-Q. Jing (2025) A Convection-Permitting Regional Climate Simulation of Changes in Precipitation and Snowpack in a Warmer Climate over the Interior Western United States. *Climate*, *13*(3), 46; https://doi.org/10.3390/cli13030046

Wang, D., Giangrande, S. E., Feng, Z., Hardin, J. C., & Prein, A. F. (2020) Updraft and downdraft core size and intensity as revealed by radar wind profilers: MCS observations and idealized model comparisons. Journal of Geophysical Research: Atmospheres, 125(11), e2019JD031774. https://doi.org/10.1029/2019JD031774

Wang, W. C., et al. (2004) Regional climate modeling: Progress, challenges, and prospects. *Journal of the Meteorological Society of Japan*, 82(6), 1599–1628.

Wilby, R. L., et al. (2004) Guidelines for use of climate scenarios developed from statistical downscaling methods. *IPCC Task Group on Data and Scenario Support for Impact and Climate Analysis (TGICA)*.

Wilby, R. L., et al. (2009) Guidelines for use of climate scenarios developed from statistical downscaling methods. *Intergovernmental Panel on Climate Change (IPCC) Task Group on Data and Scenario Support for Impact and Climate Analysis (TGICA)*.

Wongchuig, S., J. Carlo Espinoza, T. Condom, C. Junquas, J.P. Sierra, L. Fita, A. Sörensson, J. Polcher (2023) Changes in the surface and atmospheric water budget due to projected Amazon deforestation: lessons from a fully coupled model simulation. J. Hydrol., 625, Article 130082, 10.1016/j.jhydrol.2023.130082

Wright, J. S., Fu, R., Worden, J. R., Chakraborty, S., Clinton, N. E., Risi, C., ... & Yin, L. (2017) Rainforest-initiated wet season onset over the southern Amazon. Proceedings of the National Academy of Sciences, 114(32), 8481-8486.

Wu, P., Liu, Y., Lin, Y., et al. (2021) Biomass burning aerosols modulate initiation of the South American Monsoon. *Nature Communications*, 12(1), 6530.

Xie, P., R. Joyce, S. Wu, S.-H. Yoo, Y. Yarosh, F. Sun, and R. Lin (2017) Reprocessed, bias-Corrected CMORPH global high-resolution precipitation estimates from 1998. Journal of Hydrometeorology. 18, 1617-1641. DOI: 10.1175/JHM-D-16-0168.1

Xu, Z., Han, Y., & Yang, Z. (2019) Dynamical downscaling of regional climate: A review of methods and limitations. Science China Earth Sciences, 62(2), 365-375. https://doi.org/10.1007/s11430-018-9261-5

Xue, Y., Janjic, Z., Dudhia, J., Vasic, R., de Sales, F. (2014) A review on regional dynamical downscaling in interseasonal to seasonal simulation/prediction and major factors that affect downscaling ability. Atmos. Res. 147-148, 68–85.

Yang, Z., Dominguez, F. (2019) Investigating land surface effect on the moisture transport over South America with a moisture tagging model. J. Clim. 32. https://doi.org/ 10.1175/JCLI-D-18-0700.1

Yazmina Rojas, Justin R. Minder, Leah S. Campbell, Adam Massmann, and Rene Garreaud (2021) Assessment of GPM IMERG satellite precipitation estimation and its dependence on microphysical rain regimes over the mountains of south-central Chile, Atmospheric Research, 253, 105454, ISSN 0169-8095, https://doi.org/10.1016/j.atmosres.2021.105454.

Yepes, J., Poveda, G., Mejía, J. F., Moreno, L. & Rueda, C. (2019) CHOCO-JEX: A Research Experiment Focused on the Chocó Low-Level Jet over the Far Eastern Pacific and Western Colombia. Bulletin of the American Meteorological Society, 100 (5), 779-796. DOI: https://doi.org/10.1175/BAMS-D-18-0045.1)

Yin, L., Fu, R., & Zhang, Y. (2013) Rainfall variability and changes in the Amazon Basin. *Journal of Climate*, 26(19), 738–754.

Yun, Y., Liu, C., Luo, Y., Liang, X., Huang, L., Chen, F., Rasmussen, R. (2020) Convection permitting regional climate simulation of warm-season precipitation over Eastern China. Clim. Dyn. https://doi.org/10.1007/s00382-019-05070-y.

Yun, Y., Liu, C., Luo, Y., Gao, W. (2021) Warm-season mesoscale convective systems over eastern China: convection-permitting climate model simulation and observation. Clim. Dyn. 57 (7), 1–19. https://doi.org/10.1007/s00382-021-05994-4

Zemp, D. C., et al. (2014) Self-amplified Amazon forest loss due to vegetation–atmosphere feedbacks. *Nature Communications*, 5, 2597.

Zemp, D. C., Schleussner, C.-F., Barbosa, H. M. J., van der Ent, R. J., Donges, J. F., Heinke, J., . . . Rammig, A. (2014) On the importance of cascading moisture recycling in South America. Atmospheric Chemistry and Physics, 14 ,13337–13359. doi: 10.5194/acp-14-13337-2014.

Zemp, D. C., Schleussner, C.-F., Barbosa, H. M. J., & Rammig, A. (2017) Deforestation effects on Amazon forest resilience. Geophysical Research Letters, 44 .doi: 10.1002/2017GL072955.

Zhang, Xiaoxiao, Hailong Liu, and Minghua Zhang (2015) “Double ITCZ in Coupled Ocean-Atmosphere Models: From CMIP3 to CMIP5”. In: Geophysical Research Letters 42.20, pp. 8651–8659. issn: 19448007. doi: https://doi.org/10.1002/2015GL065973.

Zhang, Z.; Varble, A.; Feng, Z.; Hardin, J.; Zipser, E. (2021) Growth of mesoscale convective systems in observations and a seasonal convection-permitting simulation over Argentina. Mon. Weather Rev., 149, 3469–3490. https://doi.org/10.1175/MWR-D-20-0411.1

Zhang, Z., Varble, A. C., Feng, Z., Marquis, J. N., Hardin, J. C., & Zipser, E. J. (2024) Dependencies of simulated convective cell and system growth biases on atmospheric instability and model resolution. Journal of Geophysical Research: Atmospheres, 129, e2024JD041090. https://doi.org/10.1029/2024JD041090

Zhang, C., Wang, Y., & Hamilton, K. (2009) Improved representation of boundary layer clouds over the southeast Pacific in a climate model. *Journal of Climate*, 22(10), 2552–2565.

Zhou, J., & Lau, K.-M. (2001) Principal modes of interannual and decadal variability of summer rainfall over South America. *International Journal of Climatology*, 21(13), 1623–1644.

Zilli, M.T., Lemes, M.R., Hart, N.C.G. *et al.* (2024) The added value of using convective-permitting regional climate model simulations to represent cloud band events over South America. *Clim. Dyn*. **62**, 10543–10564. https://doi.org/10.1007/s00382-024-07460-3

Zipser, E. J., D. J. Cecil, C. Liu, S. W. Nesbitt, and D. P. Yorty (2006) Where are the most intense thunderstorms on Earth? Bull. Amer. Meteor. Soc., 87, 1057–1072, https://doi.org/10.1175/BAMS-87-8-1057.

Statements & Declarations

Funding

Authors ACV and ZF received research support from the U.S. Department of Energy Biological and Environmental Research Atmospheric System Research program under project KP1701010/57131. Kwok Chun received support from the NERC–FAPESP–NSTC Land Use Change Investigation and Regional Climate (LIRIC) project (Grant number: NE/Z504026/1) for providing the supercomputing infrastructure of ARCHER2 and JASMIN, and the Climate Collaboratorium: Co-creation of Applied Theatre Decision Labs for Exploring Climate Adaptation and Mitigation (Grant number: ES/Z000238/1). C.M.-V. received support from Proyecto ANID Fondecyt Iniciación 11250471 and Data Observatory Foundation ANID Technology Center number DO210001. Pablo Mendoza received support from CONICYT/PIA Project AFB230001 (AMTC). All other authors declare that no funds, grants, or other support were received during the preparation of this manuscript.

Competing Interests

The authors have no relevant financial or non-financial interests to disclose.

Author Contributions

Roy M. Rasmussen and Andreas F. Prein led the project. Francina Dominguez led the applications for HPC resources. All authors contributed to the conceptualization, methodology, simulation design, and discussion of the data analysis and results. Changhai Liu conducted the simulations and formal analysis. Kyoko Ikeda led the data curation, and Kyoko Ikeda and Zhe Zhang led the post-processing and data archiving. Changhai Liu wrote the first draft of the manuscript, and all authors commented on and edited earlier versions. All authors read and approved the final manuscript.

Data Availability

The SAAG dataset is openly available via the NCAR GDEX system (https://gdex.ucar.edu/datasets/d616000/) and the Chilean National Laboratory HPC system (NLHPC; https://www.nlhpc.cl/). With approximately 2 PB of raw WRF output (historical and PGW), the dataset is too large for local copies to be practical. Analysis requires substantial storage, in-situ computation, and high-speed data transfers, resources not widely available in South America. Establishing a centralized infrastructure (e.g., UK Met Office JASMIN or MPI Levante) is therefore urgent; without it, datasets of this scale cannot fully support climate science, impact studies, or policymaking in the region.

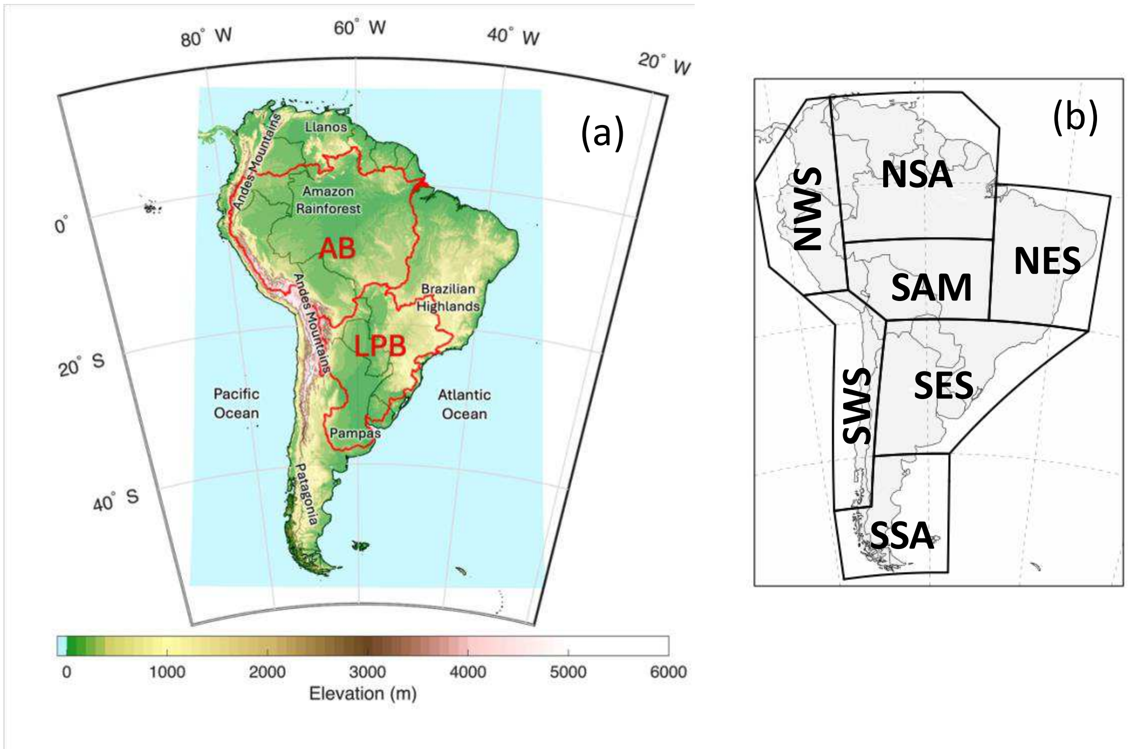

Fig. 1. (a) Model domain (cyan rectangular area) with color shading representing surface elevation (m). The domain is centered at 58°W, 22°S, with the Lambert Conformal projection, covering an area of ≈5884 km x 8108 km. The red-contoured areas denote the Amazon Basin (AB) and the La Plata Basin (LPB), respectively. (b) IPCC climate reference regions over South America, including Northwest South America (NWS), Northern South America (NSA), South American Monsoon (SAM), Northeast South America (NES), Southwest South America (SWS), Southeast South America (SES), and Southern South America (SSA).

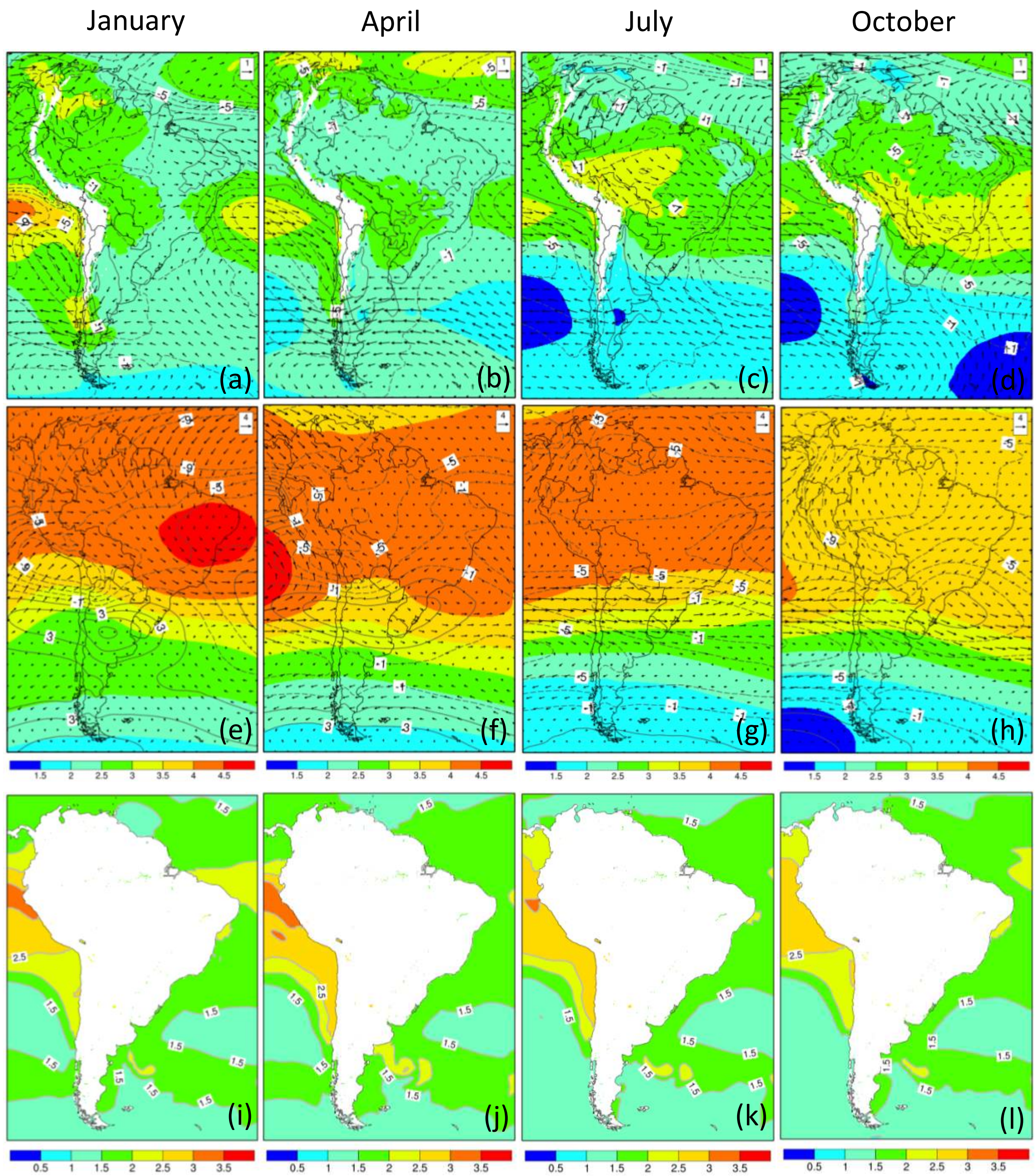

Fig. 2. Climate perturbations representing the differences between the future period 2060-2080 and the historical period 2000-2020 in LENS2. (a)-(d) are temperature (°C; color shading), relative RH (contour), and wind vectors at 850 hPa. (e)-(h) are temperature (°C; color shading), RH (contour), and wind vectors at 250 hPa. (i)-(l) are SST perturbations (°C). From left to right are January, April, July, and October, representative of the austral summer, fall, winter, and spring seasons, respectively.

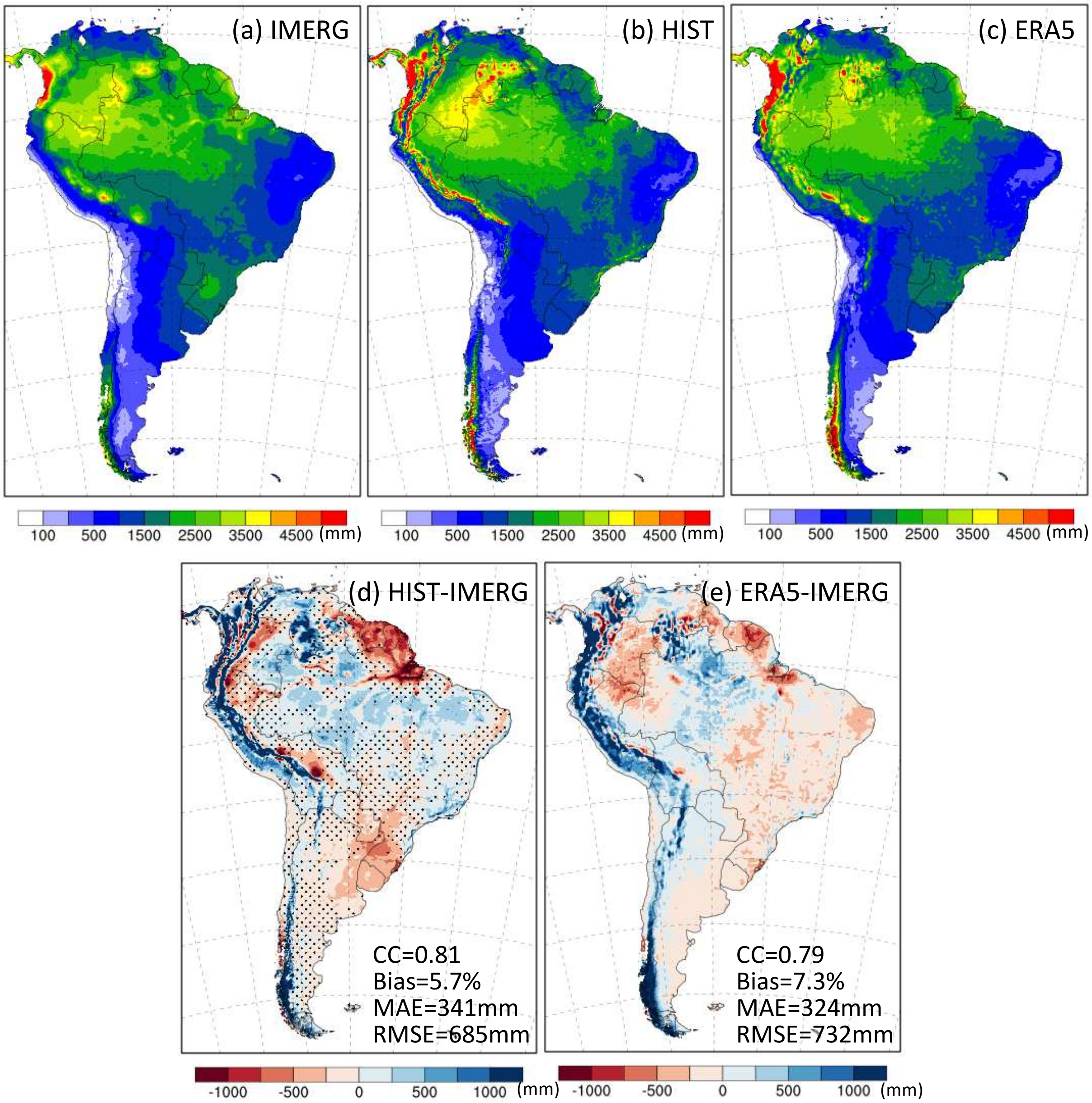

Fig. 3. Annual precipitation (mm) for IMERG (a), HIST (b), and ERA5 (c) averaged over the 21 water years from June 2000 to May 2021. Annual precipitation differences (mm) with respect to IMERG for HIST (d) and ERA5 (e). The numbers in (d)-(e) are pattern correlation coefficient (CC), percentage bias, mean absolute error (MAE), and root mean square error (RMSE). Stippled areas in (d) indicate that model biases are within the observational uncertainties estimated from observational datasets: IMERG, CHIRPS, CMORPH, CPC, GPCP, and MSWEP.

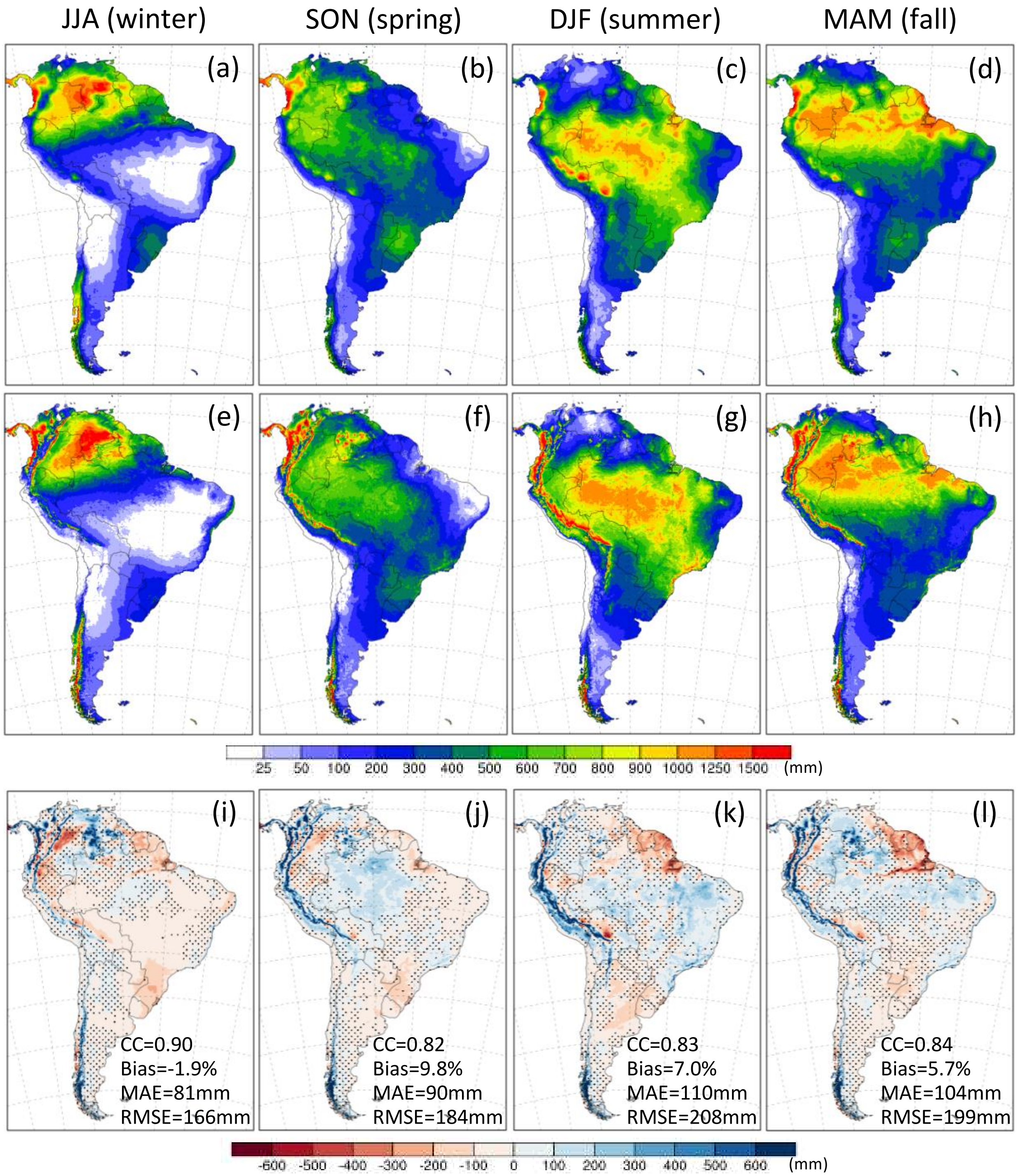

Fig. 4. Seasonal precipitation (mm), averaged over the 21 water years from June 2000 to May 2021, for IMERG (top) and HIST (middle), and difference (HIST-IMERG; bottom). From left to right are austral winter (a, e, i), spring (b, f, j), summer (c, g, k), and fall (d, h, l). The numbers in (i)-(l) are pattern correlation coefficient (CC), areal mean percent bias, mean absolute error (MAE), and root mean square error (RMSE). Stippled areas in (i)-(l) indicate that model biases are within the observational uncertainties estimated from observational datasets: IMERG, CHIRPS, CMORPH, CPC, GPCP, and MSWEP.

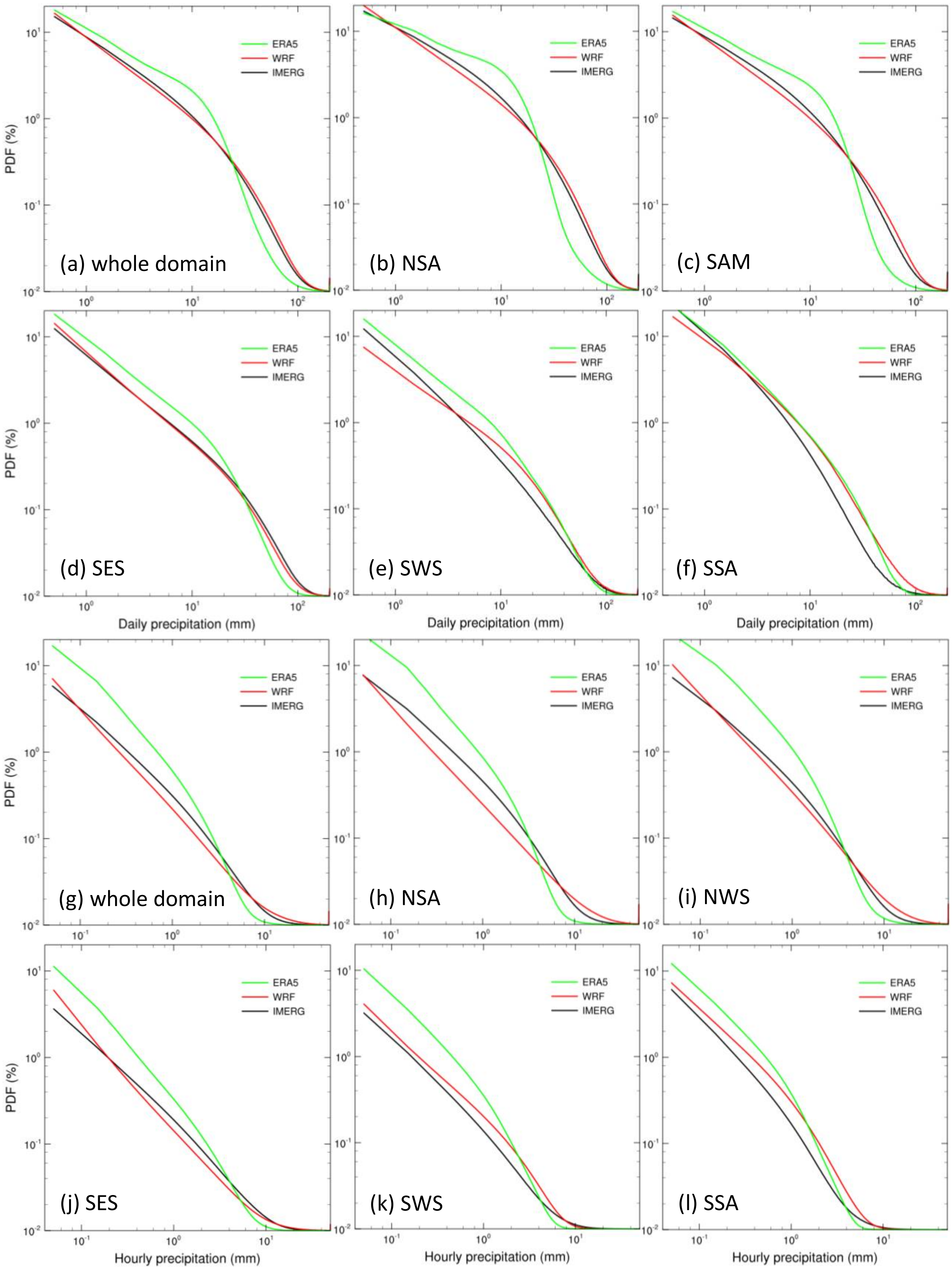

(a) whole domain
(b) NSA
(c) SAM
(d) SES
(e) SWS
(f) SSA
(g) whole domain
(h) NSA
(i) NWS
(j) SES
(k) SWS
(l) SSA
ERA5
WRF
IMERG
PDF (%)
Daily precipitation (mm)
Hourly precipitation (mm)

1864

Fig. 5. Probability density function (PDF) distributions of (a-f) daily precipitation and (g-l) hourly precipitation over land points, with the black, red, and green lines representing IMERG, HIST and ERA5, respectively. The bin widths of daily and hourly precipitation are 1 mm day^{-1} and 0.1 mm h^{-1}, respectively. (a, g) whole domain, (b, h) Northern South America (NSA), (c) South American Monsoon (SAM), (i) Northwest South America (NWS), (d, j) Southeast South America (SES), (e, k) Southwest South America (SWS), and (f, l) Southern South America (SSA).

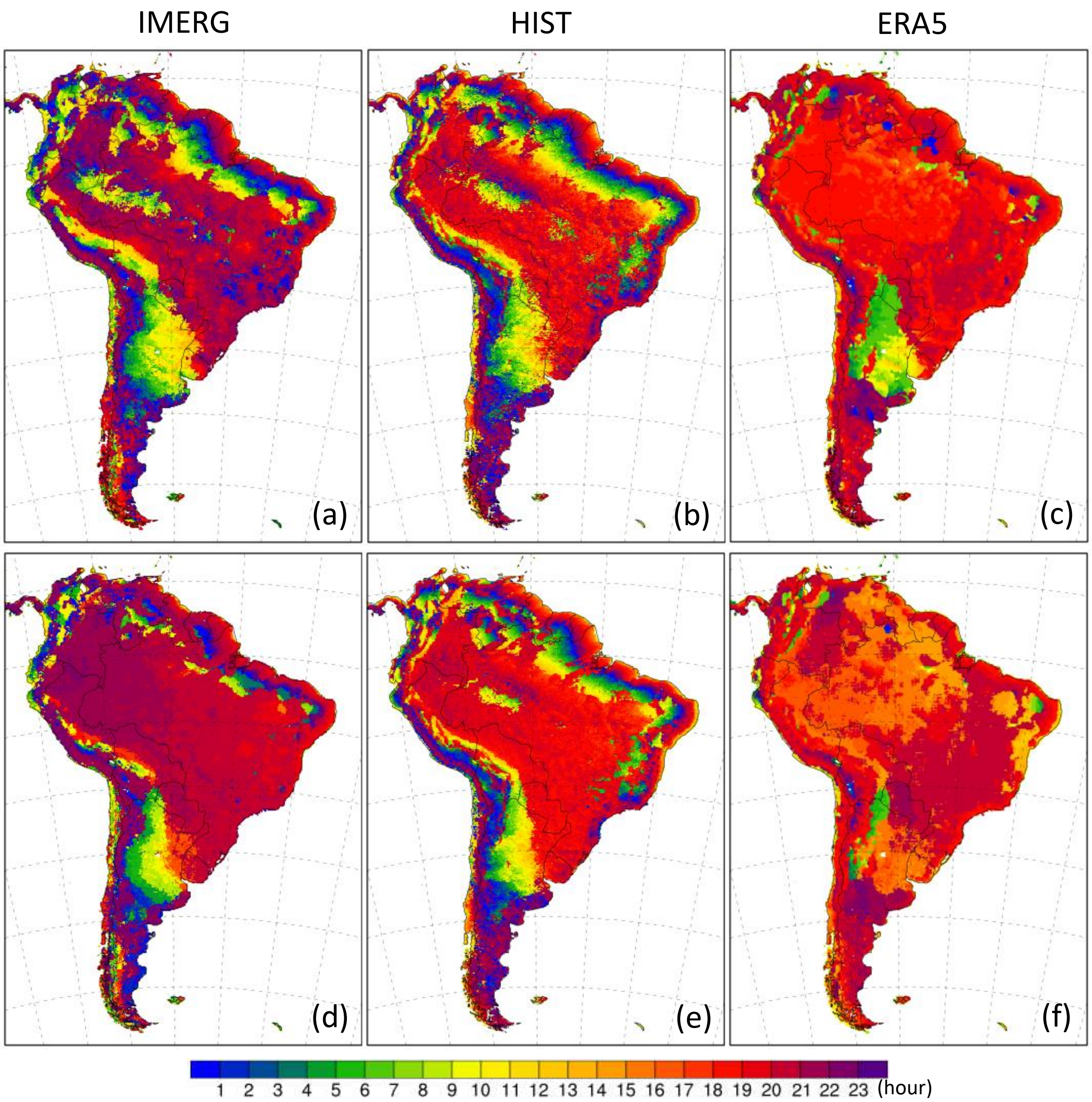

Fig. 6. UTC hour of austral summer (DJF) maximum hourly precipitation amount (top: a-c) and maximum hourly precipitation frequency (bottom: d-f) for IMERG (left), HIST (middle), and ERA5 (right). The difference between UTC and Local Solar Time (LST) mostly ranges from 3 to 5 hours, with an average of ≈4 hours; that is, LST = UTC - 4 hours for most of the continent.

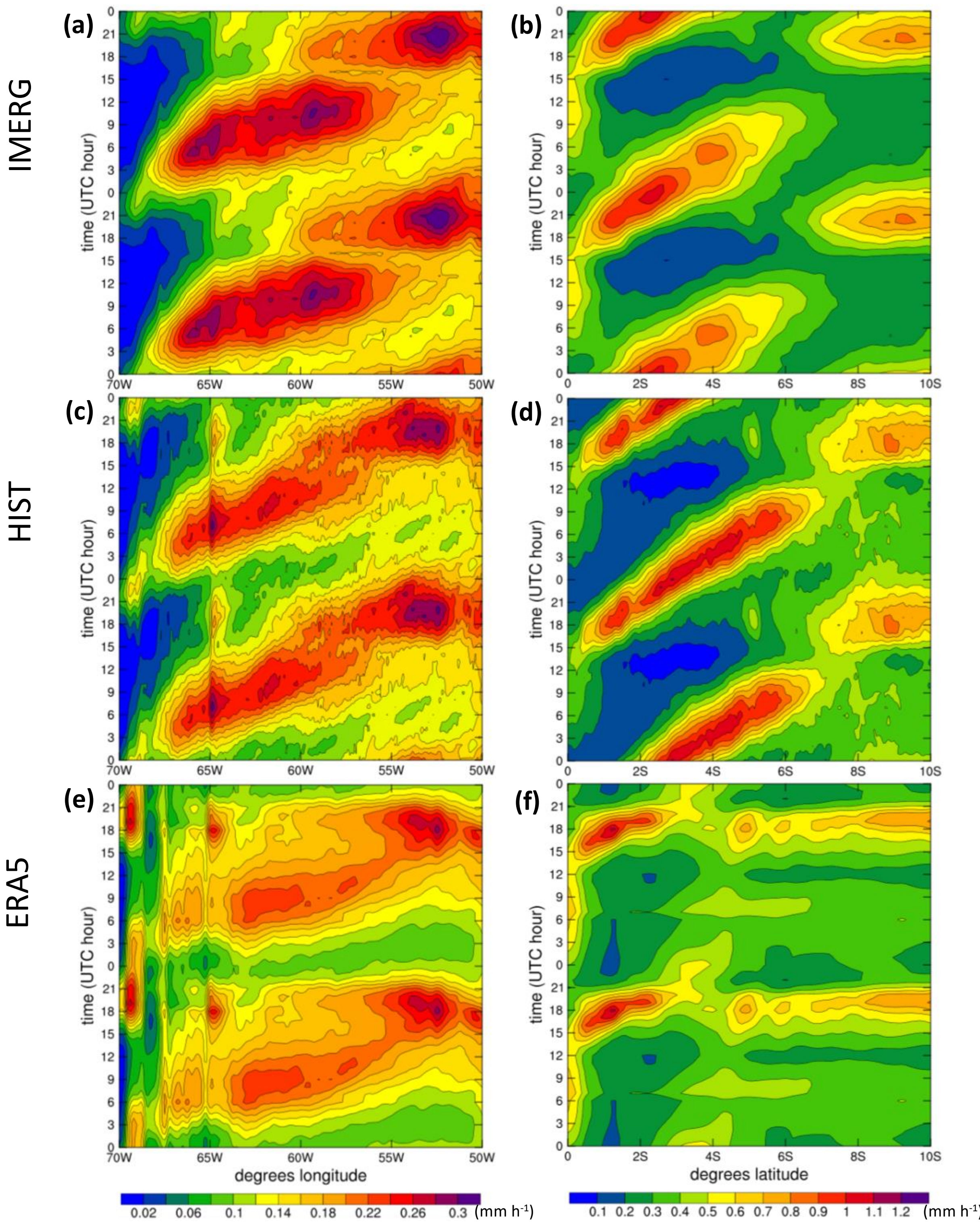

Fig. 7. Diurnal Hovmöller diagrams of summer (DJF) hourly precipitation for two sub-regions in IMERG (a, b), HIST (c, d), and ERA5 (e, f). The left panels (a, c, e) are the time-longitude distribution averaged between 29-34°S, and the right panels (b, d, f) are the time-latitude distribution averaged between 48-50°W. The diurnal cycle is repeated twice for clarity.

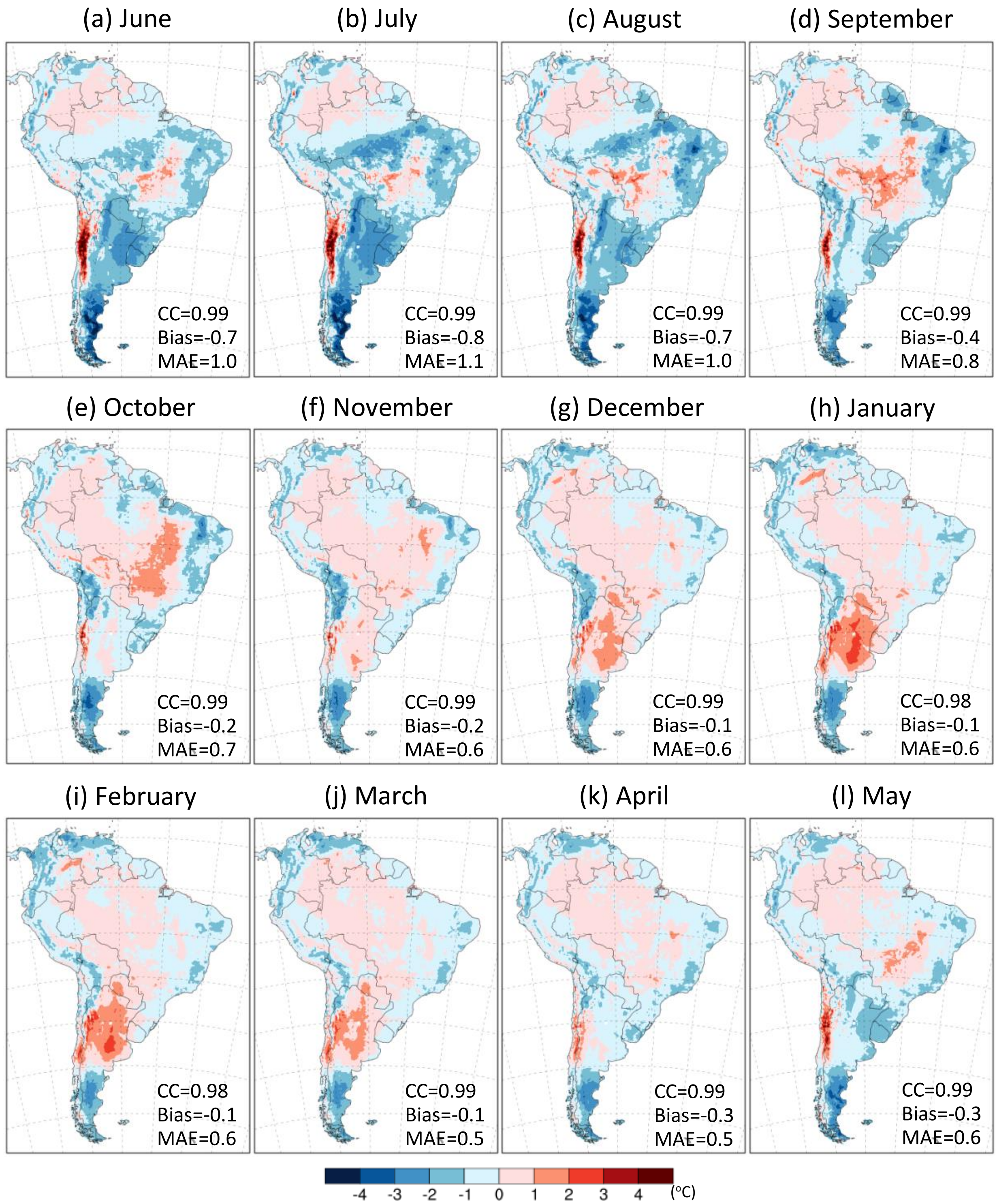

Fig. 8. Monthly mean 2-m temperature difference (°C) between HIST and ERA5 (HIST-ERA5), averaged over the 22 years from 2000 to 2021, for (a) June, (b) July, (c) August, (d) September, (e) October, (f) November, (g) December, (h) January, (i) February, (j) March, (k) April, and (l) May. The numbers are pattern correlation coefficient (CC), mean bias, and mean absolute error (MAE).

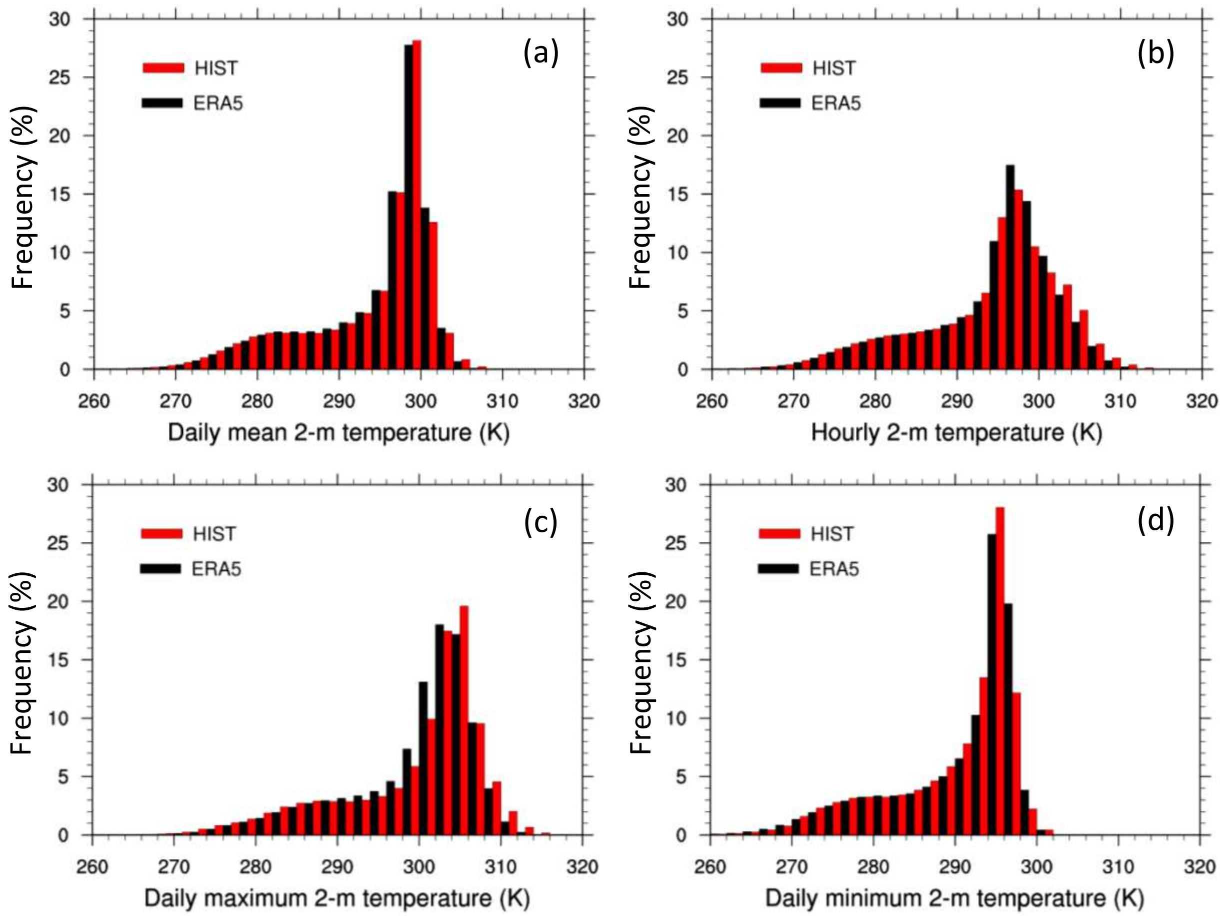

Fig. 9. Probability distribution of (a) daily mean 2-m temperature, (b) instantaneous hourly 2-m temperature, (c) daily maximum 2-m temperature, and (d) daily minimum 2-m temperature for HIST (red) and ERA5 (black). All results are computed over land points only. The bin spacing is 2 K.

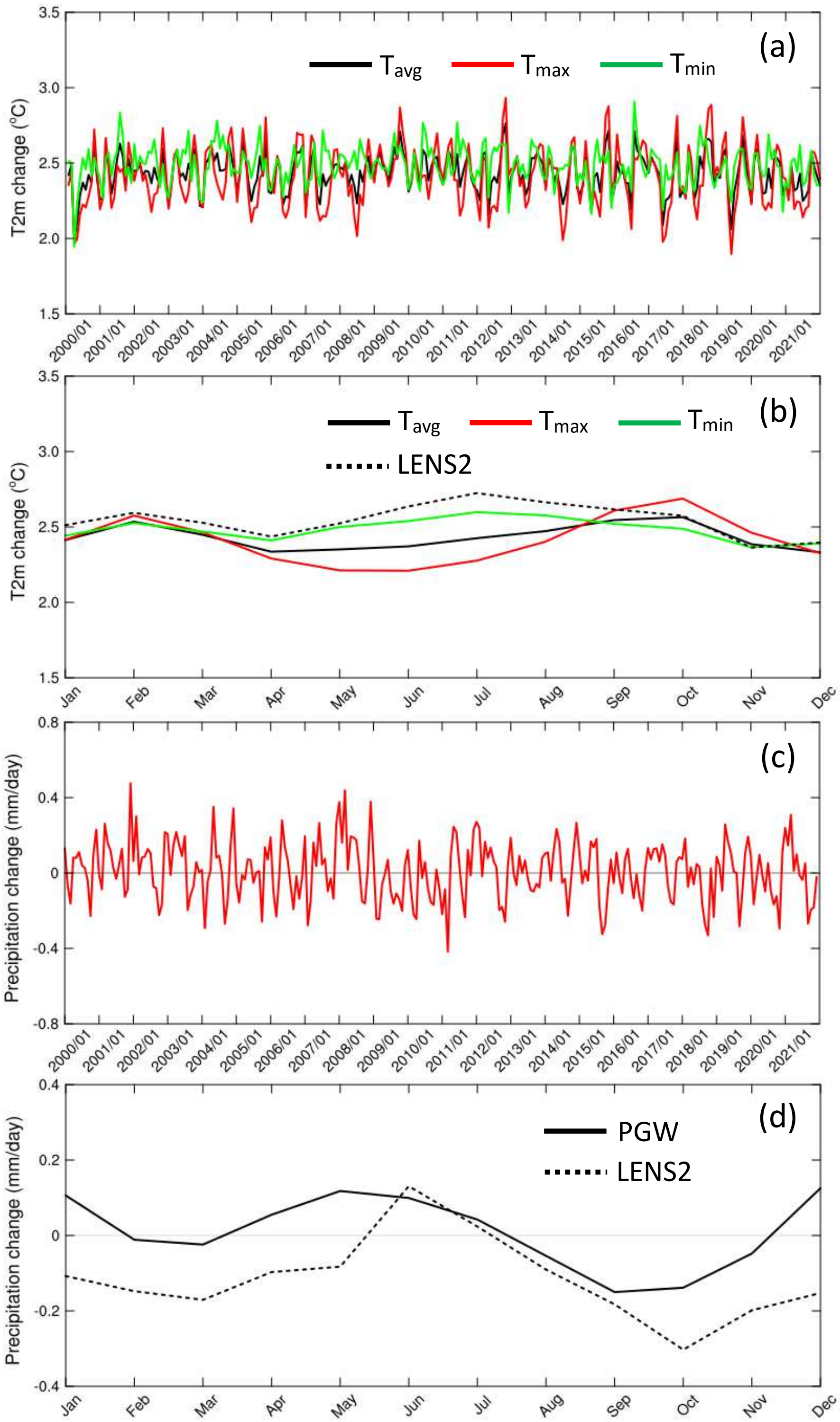

Fig. 10. Time series of (a) monthly surface air temperature and (c) precipitation changes (PGW minus HIST). The 22-year averaged annual cycle of (b) surface air temperature and (d) precipitation changes (PGW minus HIST), and LENS2 projected changes between the period 2060-2080 and the period 2000-2020.

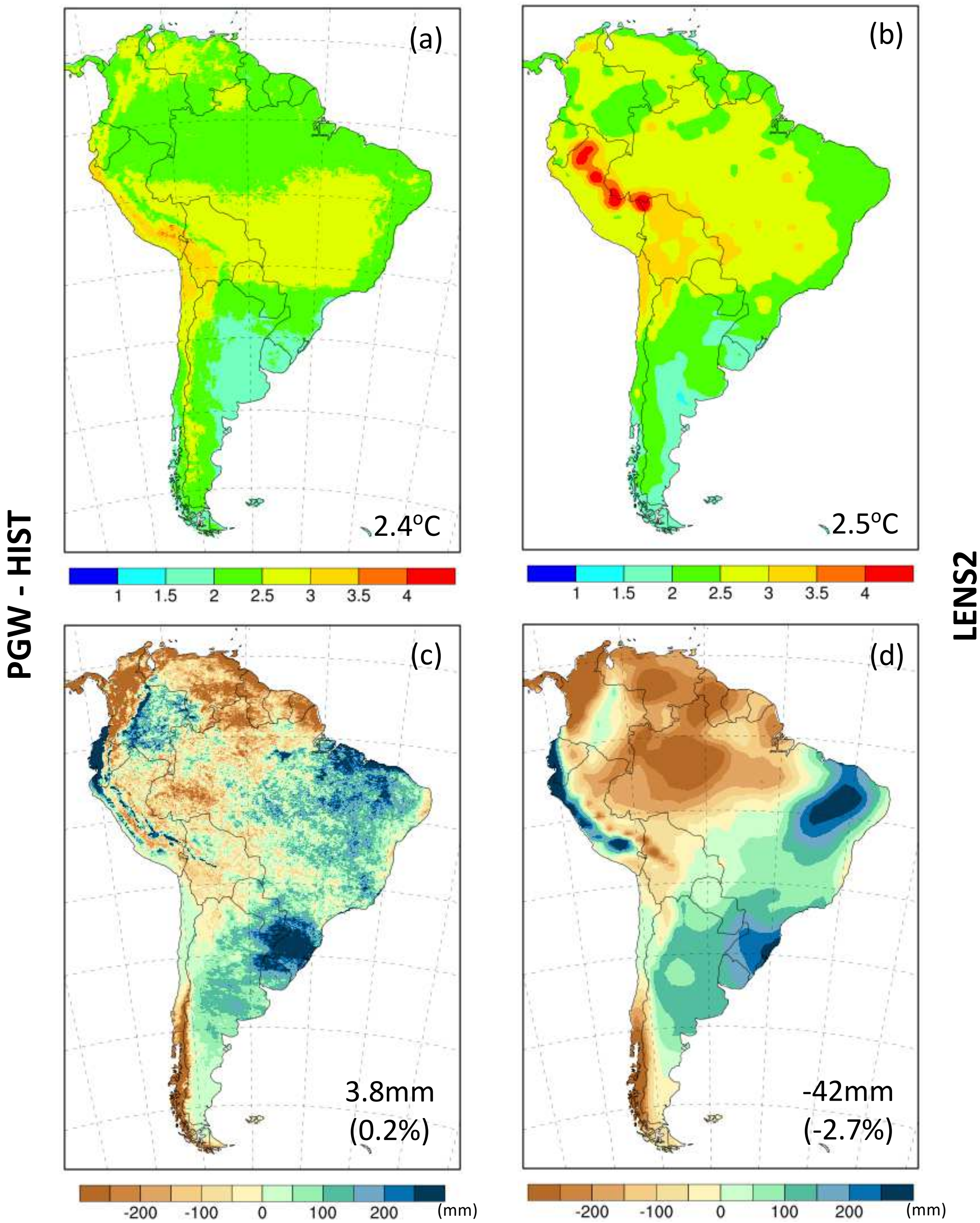

Fig. 11. (a)-(b) annual mean surface air temperature changes (°C), and (c)-(d) annual total precipitation changes (mm), corresponding to the differences between PGW and HIST (left) and the differences between the period 2060-2080 and the period 2000-2020 in LENS2 (right). The numbers are the averages over all land points.

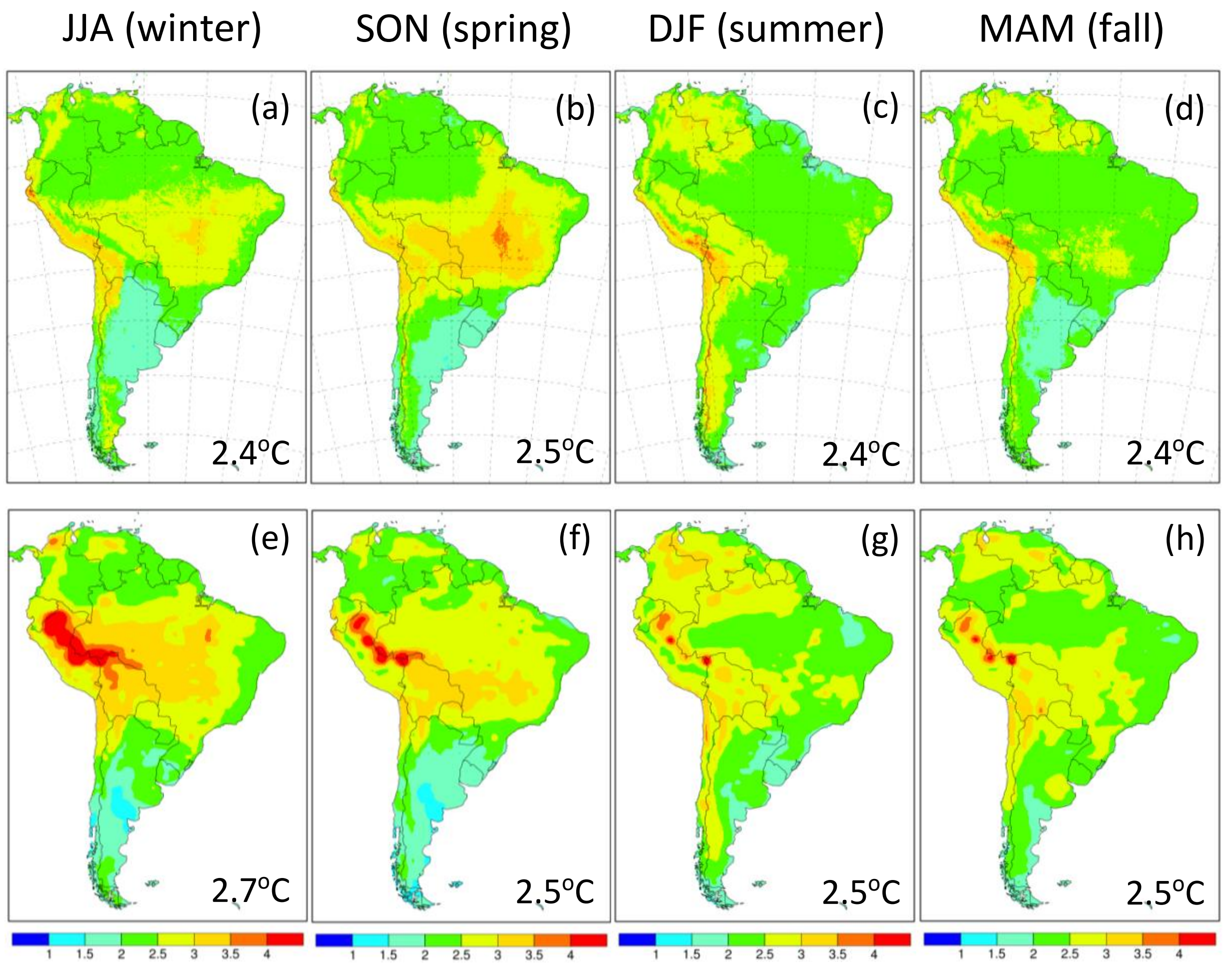

Fig. 12. Seasonal surface air temperature changes (°C) for austral winter (a, e), spring (b, f), summer (c, g), and fall (d, h). (a)-(d) stand for the differences between PGW and HIST, and (e)-(h) correspond to the differences between the two periods 2060-2080 and 2000-2020 in LENS2. The numbers are the average temperature changes over all land points.

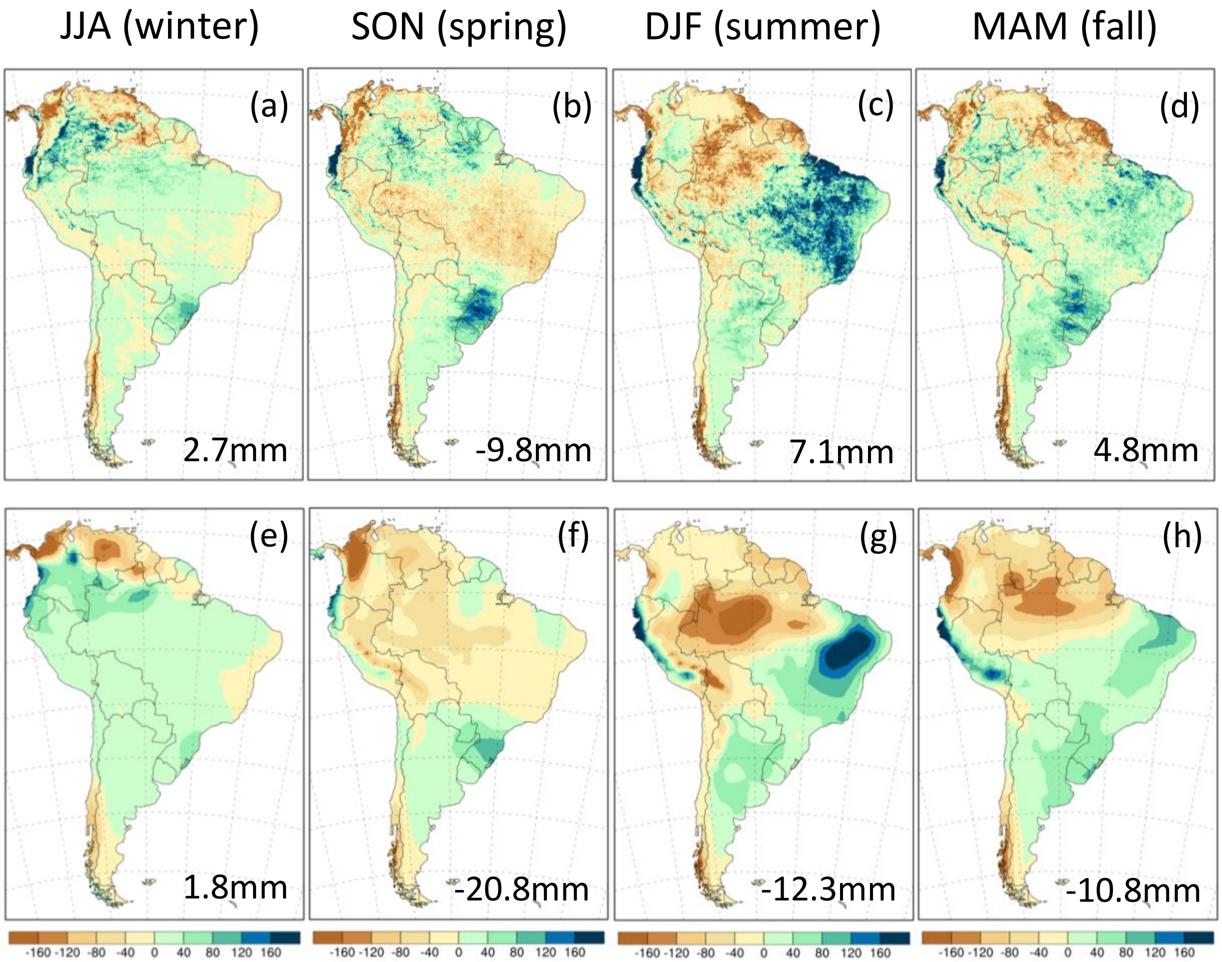

Fig. 13. Seasonal precipitation changes (mm) for austral winter (a, e), spring (b, f), summer (c, g), and fall (d, h). (a)-(d) are the differences between PGW and HIST, and (e)-(h) correspond to the differences between the two periods 2060-2080 and 2000-2020 in LENS2. The numbers are the average precipitation changes over all land points.

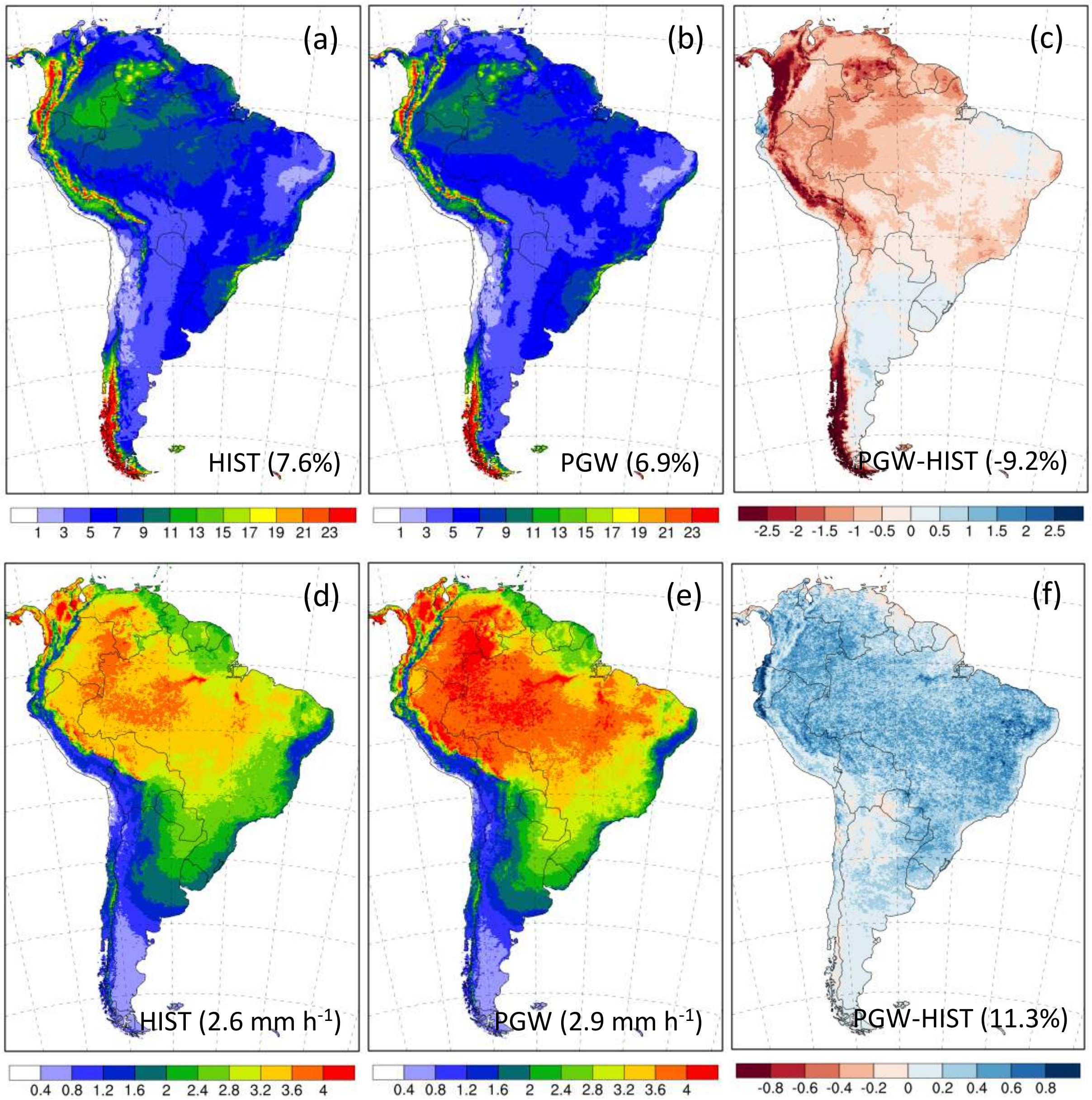

Fig. 14. Precipitation frequency (%; a-c) and intensity (mm h^{-1}; d-h) for wet hours (hourly precipitation $\geq$ 0.1 mm). From left to right are HIST, PGW, and their absolute differences (PGW-HIST). Frequency and intensity represent the percentage of wet hours relative to total hours and the mean precipitation amount over wet hours at each grid point. Values printed on the left and middle columns are land area averages, and values printed on the right column are percent differences [(PGW-HIST)/HISTx100%].

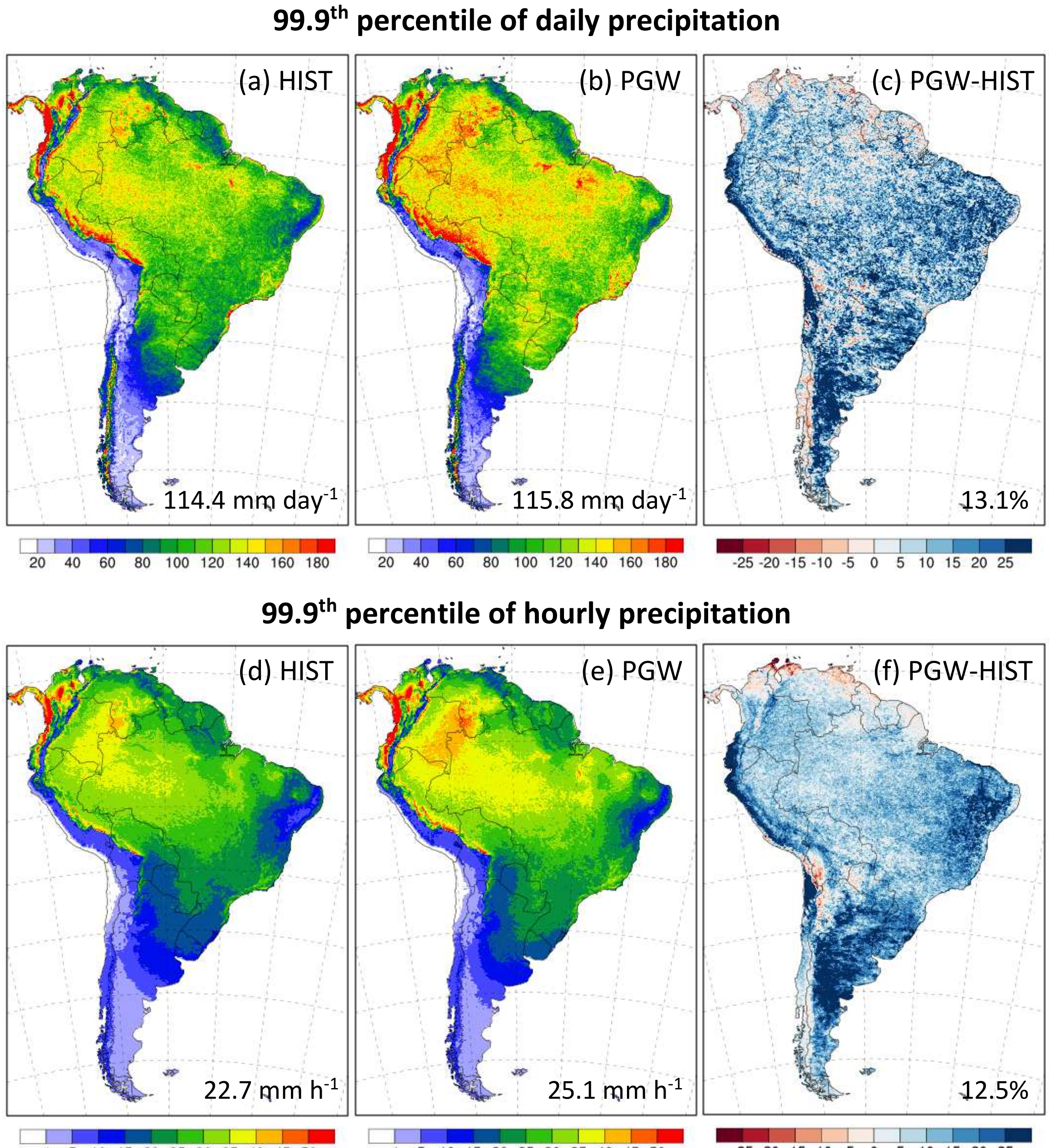

Fig. 15. The 99.9th percentile of daily precipitation (top: a-c) and hourly precipitation (bottom: d-e). From left to right are HIST, PGW, and their percent difference [(PGW-HIST)/ HISTx100%]. The numbers are the averages over all land points.

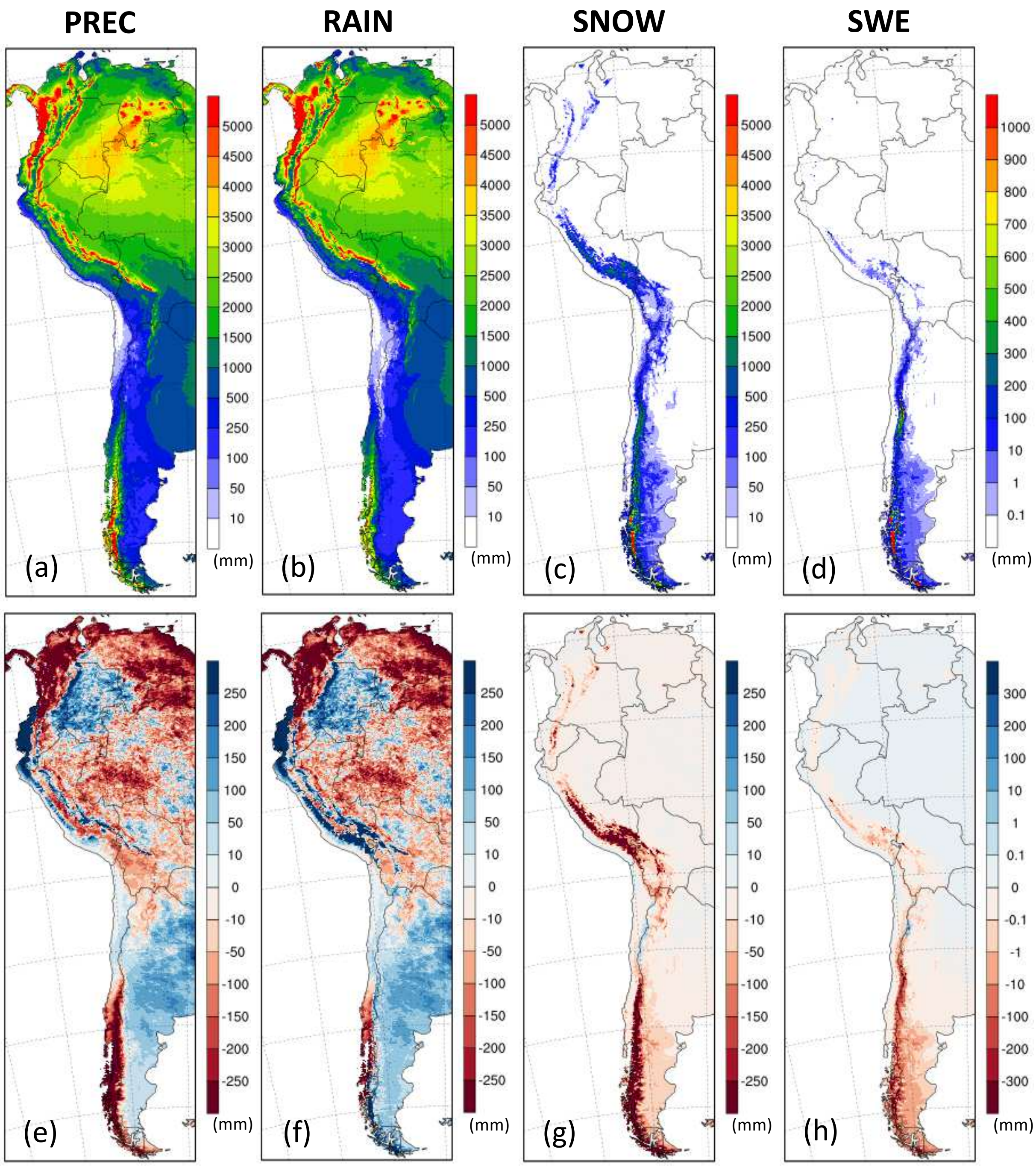

Fig. 16. Top panels are (a) annual total precipitation, (b) annual total rainfall, (c) annual total liquid equivalent snowfall, and (d) annual mean snow water equivalent (SWE), averaged over the 22 years of HIST simulation. Bottom panels are the 22-yrear average changes of (e) annual total precipitation, (f) annual total rainfall, (g) annual total liquid equivalent snowfall, and (h) annual mean SWE, corresponding to the differences between PGW and HIST (PGW-HIST). The unit for all fields is mm.

Supplement materials for: Multi-Decadal Convection Permitting Dynamical Downscaling of Current and Future Climates over South America

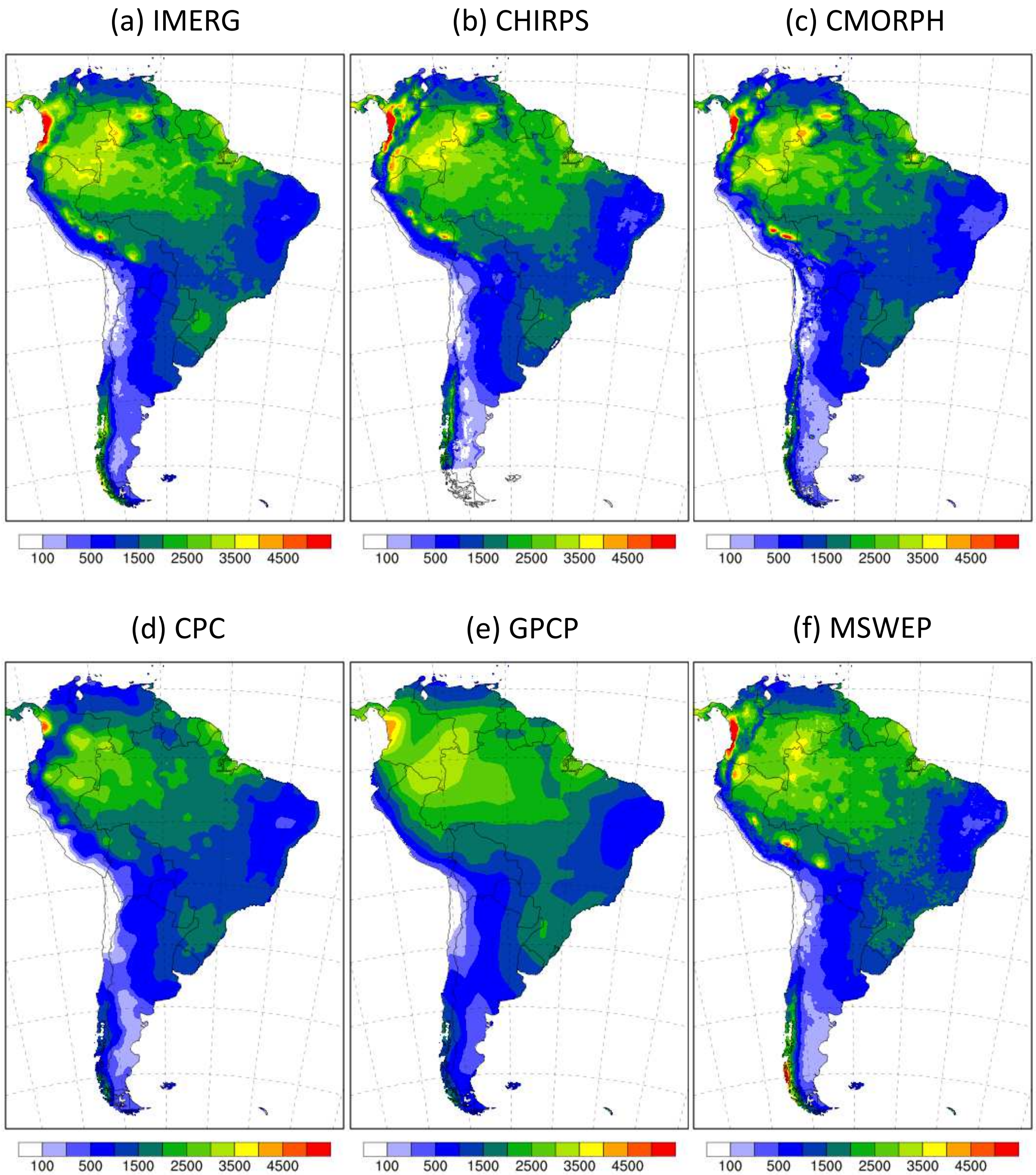

Fig. S1. Annual precipitation (mm), averaged over the 21 water years from June 2000 to May 2021, for (a) IMERG, (b) CHIRPS, (c) CMORPH, (d) CPC, (e) GPCP, and (f) MSWEP.

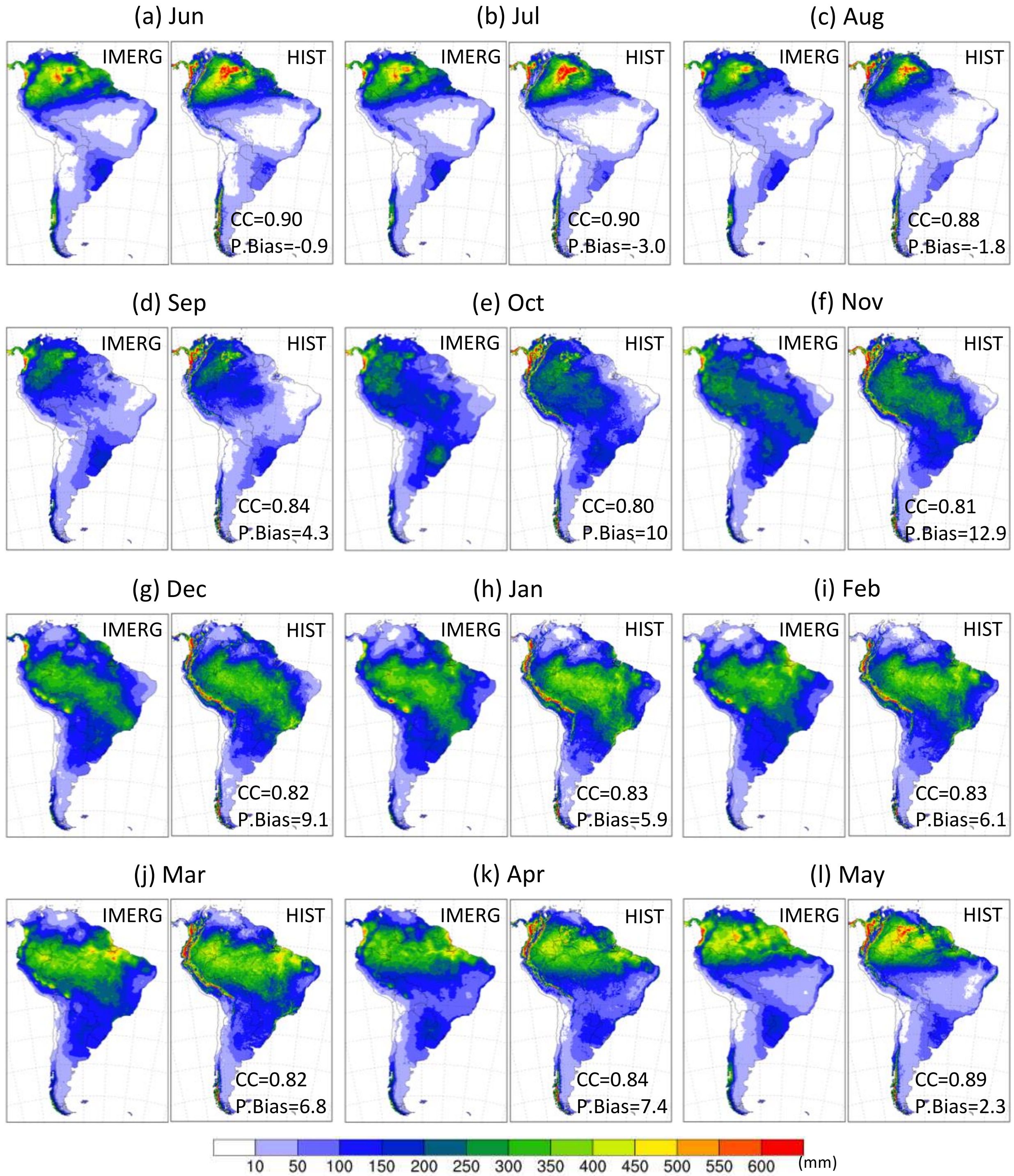

Fig. S2. Comparison of monthly precipitation (mm), averaged over the 21 water years from June 2000 to May 2021, between IMERG (left) and HIST simulation (right) for (a) June, (b) July, (c) August, (d) September, (e) October, (f) November, (g) December, (h) January, (i) February, (j) March, (k) April, and (l) May. The numbers are pattern correlation coefficient (CC) and percentage bias (%) over land points.

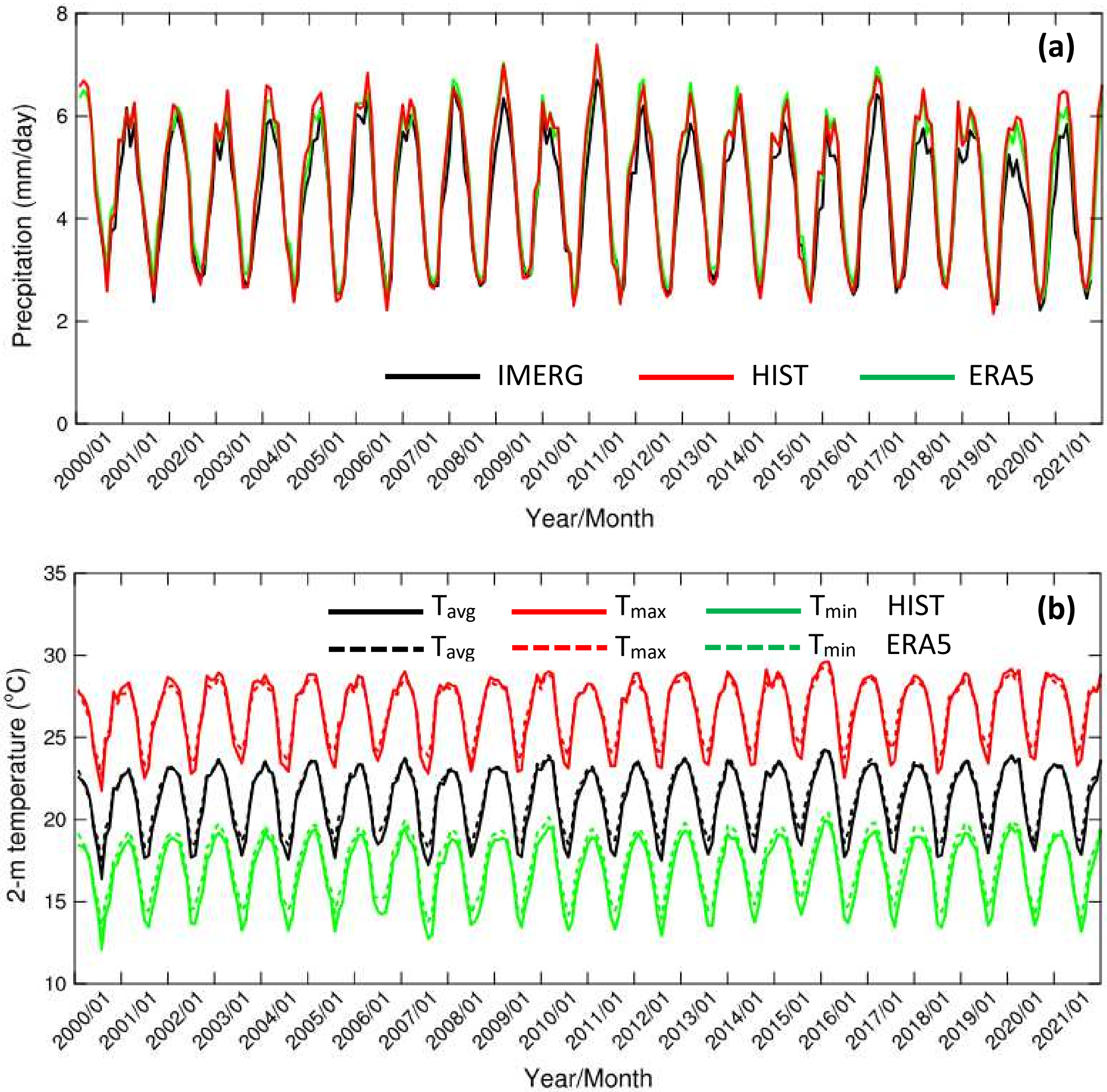

Fig. S3. Times series of (a) monthly mean daily precipitation for HIST (red), IMERG (black), and ERA5 (green), and (b) monthly mean daily average temperature (black), daily maximum temperature (red), and daily minimum temperature (green) for HIST (solid) and ERA5 (dashed). Variables are spatially averaged over all land points.

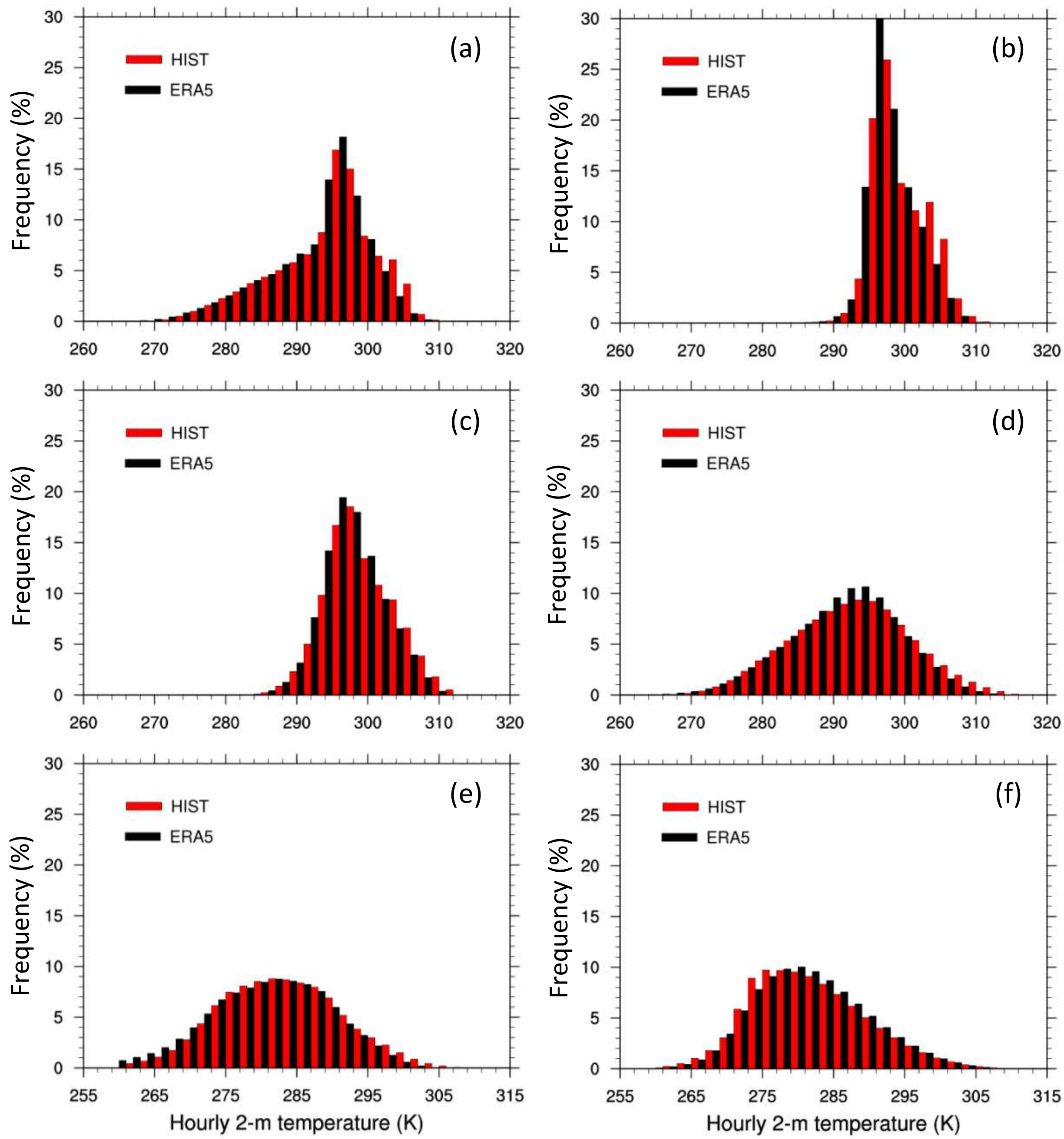

Fig. S4. Probability distribution of instantaneous hourly 2-m temperature over different climate regions for HIST (red) and ERA5 (black). (a) NWS, (b) NSA, (c) NES, (d) SES, (e) SWS, and (f) SSA. All results are computed over land points of each climate region only. The bin width is 2 K.